Aus dem Institut für Schlaganfall- und Demenzforschung (ISD)

Klinikum der Ludwig-Maximilians-Universität München

Direktor: Prof. Dr. Martin Dichgans

HTRA1 loss-of-function signatures in the brain vessel proteomes of CADASIL and cerebral amyloid angiopathy patients

Dissertation

zum Erwerb des Doktorgrades der Naturwissenschaften

an der Medizinischen Fakultät der

Ludwig-Maximilians-Universität zu München

vorgelegt von

Andreas Zellner

aus

Starnberg

2020

Mit Genehmigung der Medizinischen Fakultät

der Universität München

Betreuer:	PD Dr. Christof Haffner
Zweitgutachter:	Prof. Dr. Michael Ehrmann
Dekan:	Prof. Dr. med. dent. Reinhard Hickel
Tag der mündlichen Prüfung:	13.05.2020

EIDESSTATTLICHE VERSICHERUNG

Ich erkläre hiermit an Eides statt, dass ich die vorliegende Dissertation mit dem Thema „HTRA1 loss-of-function signatures in the brain vessel proteomes of CADASIL and cerebral amyloid angiopathy patients" selbstständig verfasst, mich außer der angegebenen keiner weiteren Hilfsmittel bedient und alle Erkenntnisse, die aus dem Schrifttum ganz oder annähernd übernommen sind, als solche kenntlich gemacht und nach Herkunft unter Bezeichnung der Fundstelle einzeln nachgewiesen habe. Ich erkläre des Weiteren, dass die hier vorgelegte Dissertation nicht in gleicher oder in ähnlicher Form bei einer anderen Stelle zur Erlangung eines akademischen Grades eingereicht wurde.

München, den 15.07.2020

_____

Andreas Zellner

PUBLICATIONS RELATED TO THIS THESIS

Zellner, A., E. Scharrer, T. Arzberger, C. Oka, V. Domenga-Denier, A. Joutel, S. F. Lichtenthaler, S. A. Müller, M. Dichgans, and C. Haffner. 2018. 'CADASIL brain vessels show a HTRA1 loss-of-function profile', *Acta Neuropathol*, 136: 111-25.

Ziaei, A., X. Xu, L. Dehghani, C. Bonnard, A. Zellner, A. Y. Jin Ng, S. Tohari, B. Venkatesh, C. Haffner, B. Reversade, V. Shaygannejad, and M. A. Pouladi. 2019. 'Novel mutation in HTRA1 in a family with diffuse white matter lesions and inflammatory features', *Neurol Genet*, 5: e345.

ABSTRACT

Cerebral autosomal dominant arteriopathy with subcortical infarcts and leukoencephalopathy (CADASIL) is the most frequent monogenetic small vessel disease (SVD) and caused by the mutation-induced accumulation and aggregation of the Notch3 extracellular domain (Notch3^{ECD}) in brain vessel walls. The molecular processes linking Notch3^{ECD} deposition to vessel degeneration are so far only incompletely understood and therefore, the brain vessel proteome from CADASIL patient autopsy samples was determined by quantitative mass spectrometry. This revealed a strong enrichment of secreted and extracellular space proteins including the high temperature requirement protein A1 (HTRA1), a serine protease genetically inactivated in a SVD with phenotypic similarity to CADASIL. The colocalization of HTRA1 with Notch3^{ECD} deposits and the accumulation of several HTRA1 substrates in the CADASIL proteome indicated a sequestration process accompanied by functional inactivation. Indeed, a comparison with the brain vessel proteome of HTRA1 knockout mice revealed a highly significant overlap suggesting the presence of a loss-of-function signature. A number of shared proteins were identified as novel HTRA1 substrates using *in vitro* proteolysis assays. To investigate whether HTRA1 is also involved in cerebral amyloid angiopathy (CAA), a SVD characterized by the vascular deposition of amyloid β, the proteomic profile of isolated brain vessel from CAA patient autopsy material was determined. As in the CADASIL study, a significant enrichment of HTRA1, its colocalization with pathological deposits and the presence of a HTRA1 loss-of-function signature was observed. Thus, this study provides evidence for a loss of HTRA1 function as a critical step in the pathological cascades underlying CADASIL and CAA, and suggests a more general role of HTRA1 in SVD pathogenesis.

ZUSAMMENFASSUNG

Zerebrale autosomal dominante Arteriopathie mit subkortikalen Infarkten und Leukenzephalopathie (CADASIL) ist die häufigste monogenetische Mikroangiopathie und wird durch die mutationsinduzierte Akkumulation und Aggregation der extrazellulären Domäne von Notch3 (Notch3^{ECD}) in den Gefäßwänden des Gehirns ausgelöst. Die molekularen Prozesse, durch welche Notch3^{ECD}-Ablagerungen zu Gefäßdegeneration beitragen, sind bisher nur unvollständig verstanden, weshalb das zerebrale Gefäßproteom aus CADASIL-Autopsiematerial mit Hilfe quantitativer Massenspektrometrie bestimmt wurde. Dies zeigte eine starke Anreicherung von sekretierten Proteinen und Proteinen des Extrazellulärraumes, einschließlich der Serinprotease HTRA1 (high temperature requirement protein A1), bei der eine genetische Inaktivierung zu einer Mikroangiopathie führt, die phänotypische Ähnlichkeit zu CADASIL aufweist. Die Kolokalisation von HTRA1 mit Notch3^{ECD}-Ablagerungen und die Akkumulation mehrerer HTRA1-Substrate im CADASIL-Proteom deuteten auf einen Sequestrierungs-Prozess hin sowie eine funktionelle Inaktivierung. Tatsächlich zeigte ein Vergleich mit dem zerebralen Gefäßproteom von HTRA1-Knockout-Mäusen eine hochsignifikante Überlappung, was das Vorhandensein einer Funktionsverlust-Signatur signalisierte. Eine Reihe der gemeinsamen Proteine wurde unter Verwendung von *in vitro* Proteolyse-Experimenten als neue HTRA1-Substrate identifiziert. Um zu untersuchen, ob HTRA1 auch bei zerebraler Amyloidangiopathie (CAA) beteiligt ist, einer Mikroangiopathie gekennzeichnet durch vaskuläre Ablagerung von Amyloid-β, wurde das proteomische Profil isolierter Gehirngefäße aus CAA-Autopsiematerial bestimmt. Wie auch in der CADASIL-Studie wurde eine signifikante Anreicherung von HTRA1, eine Kolokalisation mit pathologischen Ablagerungen und die Anwesenheit einer HTRA1-Funktionsverlust-Signatur beobachtet. Diese Studie liefert somit Hinweise auf einen Funktionsverlust von HTRA1 als kritischen Schritt in den Krankheitskaskaden von CADASIL und CAA, und deutet auf eine allgemeinere Rolle von HTRA1 bei der Entstehung von Mikroangiopathien hin.

TABLE OF CONTENTS

TABLE OF CONTENTS

1 INTRODUCTION

Dementia is defined as a loss of cognitive functions including memory, thinking and behavior and characterized by the inability to perform daily tasks. The greatest known risk factor for dementia is age and, as life expectancy increases, it is developing into one of the major public health problems in our aging society. In the last quarter of a century, the global number of individuals who lived with dementia more than doubled from 20.2 million in 1990 to 48.3 million in 2016 (Nichols et al. 2019) and is expected to reach more than 115 million by 2050 (Prince et al. 2013).

Vascular dementia (VD) is the second most common cause of dementia after Alzheimer's disease (AD) and thought to arise from defects in cerebral blood flow (Kalaria 2018). When blood supply is interrupted, either by the blockage (ischemic stroke) or the rupture of a blood vessel (hemorrhagic stroke), brain tissue is immediately deprived of oxygen and nutrients. In principle every stroke subtype can cause VD (Dichgans et al. 2017), but cerebral small vessel disease (SVD), which accounts for about 20% of all ischemic strokes, is considered as the most common cause and includes arteriolosclerosis, cerebral amyloid angiopathy (CAA), but also genetic disorder such as cerebral autosomal dominant arteriopathy with subcortical infarcts and leukoencephalopathy (CADASIL) (Pantoni 2010).

1.1 The cerebral vasculature

SVD primarily affects the intracerebral vasculature, which shows a unique architecture (Iadecola 2017). Blood supply of the brain is ensured by two pairs of large arteries (internal carotid and vertebral arteries; left and right) merging into a unique circular arrangement of blood vessels, the so-called Circle of Willis (Figure 1.1). Branching from this, the three main cerebral arteries (anterior, middle and posterior artery) progressively divide into smaller resistance arteries and arterioles that run along the surface until penetrating arterioles submerge into the corresponding regions of the cerebral cortex as a further branched network of capillaries. Penetrating arterioles are longer and less extensively branched, so that the occlusion of an individual arteriole results in reduced blood supply and subsequent tissue damage.
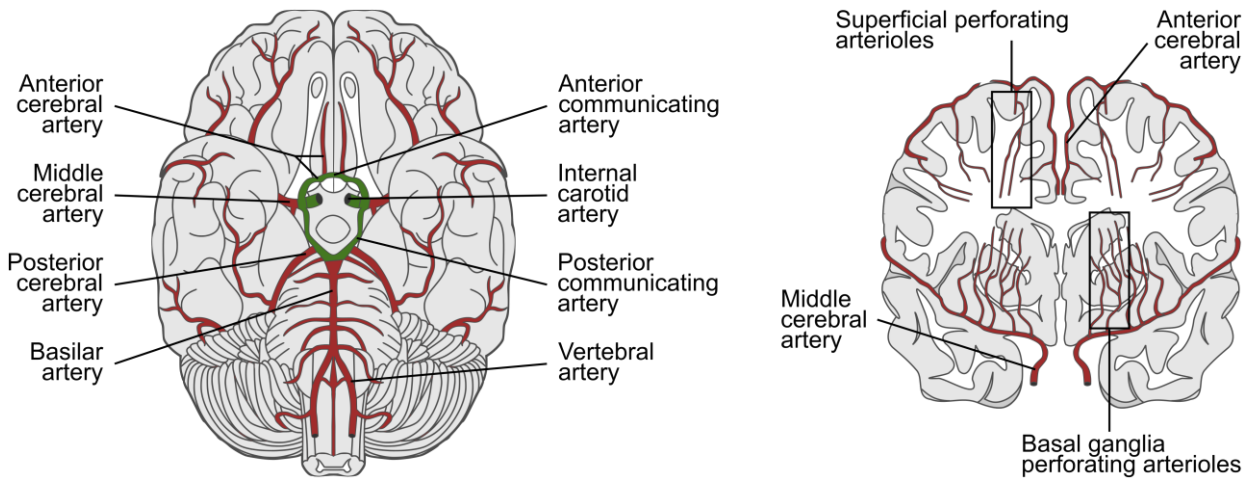
Figure 1.1: The brain vascular network. (**left**): Main cerebral arteries including the Circle of Willis (highlighted in green). (**right**): Coronal section illustrating perforating arterioles supplying the white and deep gray matter. (adapted from Wardlaw et al. 2019)

The structure of cerebral vessels depends on their type and size but in principle always consists of three distinct layers. The tunica intima, the innermost lining of a vessel, is composed of a single layer of endothelial cells and the basement membrane. Its main function is the sealing of the vessel lumen and thereby the maintenance of the blood-brain barrier. The basement membrane, a thin layer of connective tissue, is composed of collagen type IV, heparin sulfate proteoglycans, laminin, fibronectin, and other extracellular matrix (ECM) proteins and links the endothelial cell layer to the underlying tissue. The tunica media, the middle layer of the vessel wall, is mainly composed of mural cells (vascular smooth muscle cells, pericytes) supported by a framework of collagenous and elastic fibers. Through contraction or relaxation, vascular smooth muscle cells are able to control the vessel lumen diameter and thereby blood pressure and blood flow. The tunica adventitia, the outermost layer of a blood vessel, is mainly composed of connective tissue produced by fibroblasts and is important for the integration of the blood vessel in the surrounding tissue.

Capillaries are the smallest blood vessels (5-10 µm) and serve as the primary site of oxygen and nutrient exchange with a total length of about 650 km in a human brain (Begley et al. 2003). They are composed of a single layer of endothelial cells, wrapped by pericytes and encased by the basement membrane (Figure 1.2). In the brain, they are continuously covered by astrocytic endfeet which have an important influence on capillary function by regulating cerebral blood flow and representing an interface to neurons known as the neurovascular unit. This crosstalk between all different cell types is important for the maintenance of vessel function and may provide a primary site for neurovascular diseases (Iadecola 2017).
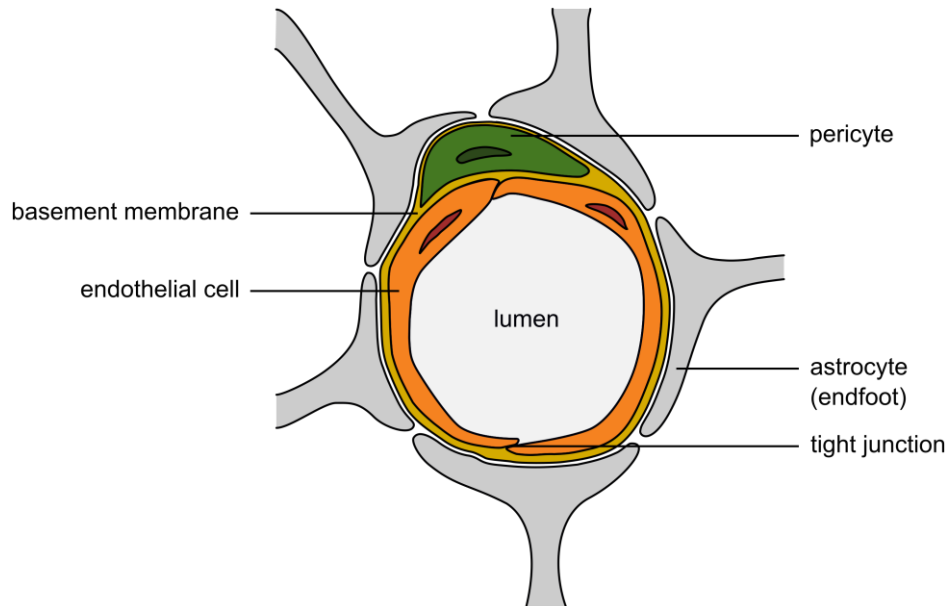
Figure 1.2: Structure of a brain capillary. A single layer of endothelial cells (sealed by tight junctions) and pericytes are encased by the basement membrane and continuously covered by astrocytic endfeet.

1.2 Cerebral small vessel disease (SVD)

SVD describes a group of neuroimaging and neuropathological abnormalities, originating from pathological changes in the structure and function of perforating cerebral arterioles, capillaries and venules (Wardlaw et al. 2019; Pantoni 2010). Although the patients' symptoms are diverse and show a high variability, clinical or radiologic manifestations of SVD can be detected in about 80% of 65-years old adults and in almost 100% of 90-years old individuals, classifying SVD as the most common age-related condition of the brain (Haffner et al. 2016).

Since small vessels are difficult to investigate *in vivo*, SVD can remain clinically unnoticed for years (Wardlaw et al. 2013). First evidence for the disease is usually provided by brain imaging techniques, showing white matter hyperintensities (WMH), cerebral microbleeds, lacunes, enlarged perivascular spaces, superficial siderosis or small subcortical infarcts in the white or subcortical gray matter (Wardlaw et al. 2019). On histopathological examination of small perforating arteries, thickening of the vessel walls due to the deposition of fibro-hyaline material, narrowing of the vessel lumen and a loss of smooth muscle cells in the tunica media are observed. In addition, several manifestations of endothelial dysfunction have been identified including impaired vasodilation, vessel stiffening as well as blood-brain barrier leakage and increased interstitial fluid content (Wardlaw et al. 2019). Mechanistically, SVD pathogenesis is still relatively poorly understood. One reason might be that the majority of pathological data is

provided by studies on post-mortem tissue, which represents the end stage of the disease, making it difficult to identify causative mechanisms (Pantoni 2010).

While SVD risk is mainly attributed to common vascular risk factors such as age, hypertension, hypercholesterolemia, diabetes mellitus, myocardial infarction and smoking (Wardlaw et al. 2019), the contribution of genetic factors is significant. However, genome-wide association studies in sporadic patient cohorts have so far revealed only a few risk loci (Rutten-Jacobs et al. 2019; Dichgans et al. 2019). In contrast, the investigation of rare Mendelian SVD forms with defined genetic origin have provided significant advancements with regard to the molecular mechanisms underlying vascular pathological changes and contributors to stroke and dementia (Haffner et al. 2016).

Advancements in linkage analysis and DNA sequencing technologies have allowed more efficient analyses of genes underlying hereditary SVD and led to the identification of a variety of causative genes (Table 1.1). Albeit genetically heterogeneous, the hereditary forms share multiple features with sporadic SVD, including a progressive arteriopathy, subcortical infarcts and white matter hyperintensities as well as stroke and dementia (Haffner et al. 2016).

Table 1.1: Monogenetic small vessel diseases

Name	Gene	Mode of inheritance	Clinical features (neurological)	Clinical features (extra-neurological)
CADASIL	NOTCH3	dominant	stroke, dementia, migraine with aura, psychiatric disorders	-
CARASIL	HTRA1	recessive	stroke, dementia	spondylosis, alopecia
late-onset HTRA1-related SVD	HTRA1	dominant	stroke, dementia	-
COL4A1/A2-related SVD	COL4A1/ COL4A2	dominant	stroke, dementia, intracerebral hemorrhages, congenital porencephalopathy	infantile hemiparesis, kidney defects, ophthal-mologic malformations
PADMAL	COL4A1	dominant	stroke, dementia, lacunar infarcts of the pons	-
RVCL	TREX1	dominant	stroke, dementia, psychiatric disturbance, migraine	retinopathy, pseudotumors, Raynaud syndrome
CARASAL	CTSA	dominant	stroke, cognitive deterioration	-
FOXC1-related SVD	FOXC1	dominant	stroke, white matter-hyperintensities	Axenfeld-Rieger syndrome

CADASIL: Cerebral autosomal dominant arteriopathy with subcortical infarcts and leukoencephalopathy; CARASIL: Cerebral autosomal recessive arteriopathy with subcortical infarcts and leukoencephalopathy; PADMAL: Pontine autosomal dominant microangiopathy with leukoencephalopathy; RVCL: Retinal vasculopathy with cerebral leukodystrophy; CARASAL: Cathepsin A-related arteriopathy with strokes and leukoencephalopathy

Cathepsin A-related arteriopathy with strokes and leukoencephalopathy (CARASAL) (Bugiani et al. 2016), retinal vasculopathy with cerebral leukodystrophy (RVCL) (Richards et al. 2007) and FOXC1-related SVD (French et al. 2014) are extremely rare monogenetic SVD forms identified in isolated cases only. So far their disease mechanisms are mostly elusive. Several SVD forms are caused by mutations in *COL4A1* and *COL4A2* encoding subunits of collagen type IV, an important component of the vascular basement membrane (Kuo et al. 2012). While coding region mutations are associated with systemic SVD involving not only the brain, but also the eyes, muscles and kidneys and lead to a disruption of basement membrane integrity, mutations in the *COL4A1* 3'-untranslated region interrupt a miRNA binding site and result in pontine autosomal dominant microangiopathy with leukoencephalopathy (PADMAL), a stroke disorder primarily characterized by a pathology in the pons (Verdura et al. 2016).

Cerebral autosomal dominant arteriopathy with subcortical infarcts and leukoencephalopathy (CADASIL), and the phenotypically related syndrome cerebral autosomal recessive arteriopathy with subcortical infarcts and leukoencephalopathy (CARASIL) are the currently most intensely investigated hereditary SVD forms. CADASIL is the main topic of this thesis and its features are discussed in detail in chapter 1.4.

1.3 HTRA1-related SVD

CARASIL, initially called Maeda syndrome, is characterized by typical SVD symptoms, including white matter hyperintensities, lacunar infarcts and a vasculopathy of penetrating arteries and arterioles (Maeda et al. 1976; Fukutake 2011; Oide et al. 2008). Striking for CARASIL is the early age of onset (10 to 30 years) and the presence of spondylosis and alopecia as extra-neurological symptoms (Dichgans et al. 2019). By linkage analysis and sequencing of candidate genes CARASIL was found to be caused by homozygous mutations in the *HTRA1* gene encoding for high temperature requirement protein A1. Most mutations are causing missense variants leading to a loss of HTRA1 function, in agreement with the recessive inheritance pattern. But recently, heterozygous HTRA1 mutations were identified as cause for a dominant SVD form, which is clinically related to CARASIL, but lacks the extra-neurological symptoms and shows a delayed age of onset (Nozaki et al. 2016; Verdura et al. 2015). The molecular mechanism underlying the dominant inheritance pattern has not been clearly elucidated yet (see below).

HTRA1 belongs to the highly conserved family of HTRA serine proteases, distinguishable from other serine proteases by the presence of a C-terminal PDZ (postsynaptic density of 95 kDa discs large and zonula occludens 1) domain, responsible for the allosteric activation upon substrate interaction (Clausen et al. 2011). In a variety of species including bacteria and plants, HTRA proteases have been implicated in protein quality control, such as the degradation of misfolded and mislocalized proteins and the maintenance of extracellular protein homeostasis (Clausen et al. 2011). However, the role of the four mammalian family members (HTRA1-4) is less well understood. Important for their catalytic activity is the formation of pyramidal trimers (Hansen et al. 2013). In addition to HTRA2, a mitochondrial protein involved in Parkinson's disease, HTRA1 is the best characterized family member in humans. It is predominantly secreted (Clausen et al. 2011) and, although it is globally expressed, recent studies provided evidence that in the brain, it is mainly produced by astrocytes (Chen et al. 2018; He et al. 2018; Vanlandewijck et al. 2018). HTRA1 mutations resulting in CARASIL are mainly located in the protease domain, directly affecting catalytic activity (Beaufort et al. 2014; Hara et al. 2009; Nozaki et al. 2016; Verdura et al. 2015). Mutations located outside the protease domain were reported to affect HTRA1 secretion, mRNA expression, and/or protein stability (Hara et al. 2009; Shiga et al. 2011; Ziaei et al. 2019). The pathomechanism underlying heterozygous mutations is not fully understood. While haploinsufficiency cannot be completely ruled out, a dominant-negative effect was proposed on the basis of *in vitro* experiments showing an interference of some heterozygous mutations with wild-type HTRA1 activity by affecting the oligomeric state of the protease (Nozaki et al. 2016; Verdura et al. 2015).

A variety of studies have suggested an involvement of HTRA1 in transforming growth factor beta (TGF-β) signaling by mechanisms including the extracellular cleavage of mature TGF-β (Oka et al. 2004; Launay et al. 2008), cleavage of TGF-β receptors (Graham et al. 2013) or intracellular cleavage of the TGF-β prodomain (Shiga et al. 2011). In contrast, another study revealed a facilitating role of HTRA1 on the TGF-β signaling pathway by the processing of latent TGFβ-binding protein 1 (LTBP-1) and thereby mediating the release of TGF-β from the ECM (Beaufort et al. 2014). Thus, it is still controversial whether pathway activity is promoted or attenuated.

Over the last years increasing numbers of HTRA1 substrates have been identified, the majority of them secreted or located in the ECM such as fibronectin, type II collagen, biglycan, clusterin, vitronectin, aggrecan, decorin, fibromodulin and LTBP-1 (Beaufort et al. 2014; Grau et al. 2006; An et al. 2010; Tsuchiya et al. 2005). This suggested that impaired processing of ECM proteins

and a dysregulation of ECM protein homeostasis is a key pathomechanism underlying HTRA1-related SVD. In addition to SVD, HTRA1 has been associated with various other diseases, including osteoarthritis and cancer (Skorko-Glonek et al. 2013), age-related macular degeneration (Coleman et al. 2008), lattice corneal dystrophy (Venkatraman et al. 2017) as well as Alzheimer's disease (Grau et al. 2005; Grau et al. 2006; Poepsel et al. 2015; Tennstaedt et al. 2012).

1.4   CADASIL

Among all monogenetic SVD forms, CADASIL is by far the most prevalent one and was possibly already described in 1955 by Van Bogaert as a familial and rapidly progressive form of Binswanger's disease (Bousser et al. 1994) (a form of small vessel vascular dementia known since 1894) (Caplan 1995). This report stayed unnoticed for many years until the 1980s and early 1990s, when a number of cases of an autosomal-dominant cerebral SVD were described (Stevens et al. 1977; Sonninen et al. 1987; Davous et al. 1991; Tournier-Lasserve et al. 1991; Mas et al. 1992; Salvi et al. 1992; Baudrimont et al. 1993). The acronym CADASIL was coined based on the main features of the disease (Joutel et al. 1996). Its prevalence was reported to be up to 5 cases in 100,000 individuals (Razvi et al. 2005; Narayan et al. 2012), however this number is widely considered as underestimated particularly in countries were magnetic resonance imaging (MRI) and genetic testing are not available (Chabriat 2017). Originally documented in European families, it is now recognized worldwide and in all ethnic groups.

1.4.1   Clinical features

Clinically, CADASIL is characterized by recurrent subcortical infarcts, migraine with aura, mood disturbances and cognitive impairment (Chabriat et al. 2009). Migraine with aura is typically one of the first symptoms of the disease, starting at around 30 years of age, but can vary from early childhood to mid adult age (Chabriat et al. 1995; Vahedi et al. 2004). During the course of the disease cognitive decline as well as motor disabilities progress continuously leading to deficits in episodic memory and executive dysfunction (Dichgans 2002). Many patients develop mood disturbances, severe depressive or manic episodes, bipolar disorders or apathy (Tikka et al. 2014). The phenotypical variations are large, even within affected members of the same family (Di Donato et al. 2017), but the end-stage of the disease is reported around the age of 65 years, where about 80% of the patients are fully demented (Kalimo et al. 2002). Brain MRI abnormalities can be detected in CADASIL patients around the age of 20 years (Chabriat et al. 1998).

Symptomatic but also asymptomatic patients display characteristic MRI features, however their frequency and severity are correlating with the clinical status and dramatically increasing with age (Mizuta et al. 2017). White matter hyperintensities in T2-weighted images as well as lacunar infarctions on T1-weighted or FLAIR MRI located in the deep white matter, basal ganglia and brain stem are the most frequent findings (Chabriat et al. 1998). To date, there is no cure for the disease and treatment options are restricted to symptomatic and secondary preventive treatment (Sondergaard et al. 2017). Therefore, the control of vascular risk factors, particularly smoking and hypertension, is an important part of CADASIL management (Di Donato et al. 2017).

1.4.2 Genetics

The identification of two large French families allowed the localization of the genetic defect of CADASIL to the short arm of chromosome 19 and subsequently the identification of *NOTCH3* as causative gene (Joutel et al. 1996). It consists of 33 exons, encodes a single-pass type I transmembrane receptor of the evolutionary highly conserved Notch family and is primarily expressed by vascular smooth muscle cells and pericytes. In mammals the Notch family consists of four highly homologous members which are indispensable during development of most organs (Louvi et al. 2012). All Notch receptors are initially synthetized as precursor proteins and after cleavage by a furin-like convertase in the Golgi apparatus (S1-cleavage), the non-covalently linked heterodimers are transported to the cell surface (Kopan et al. 2009). The mature Notch3 receptor consists of a large extracellular domain containing 34 epidermal growth factor (EGF)-like repeats (EGFr), a negative regulatory region (NRR), comprising three Lin12/Notch repeats (LNR), a transmembrane domain and an intracellular domain (ICD) containing seven ankyrin repeats and a PEST motif (Figure 1.3).
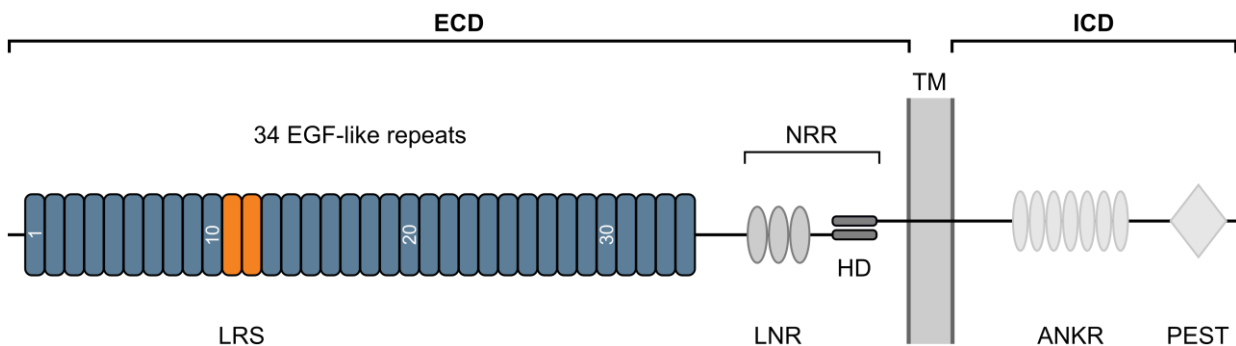
Figure 1.3: Scheme of Notch3. The structure of Notch3 is composed of an extracellular domain (ECD) with 34 epidermal growth factor (EGF)-like repeats and a negative regulatory region (NRR) composed of three Lin12/Notch repeats (LNR) and two heterodimerization domains (HD). The transmembrane domain (TM) is followed by the intracellular domain (ICD) comprising several ankyrin repeats (ANKR) and a PEST motif. LRS: ligand recognition site

Ligands of Notch3 in mammals belong either to the Jagged (Jag1 or Jag2) or Delta-like (DLL) family (DLL1, 3 or 4) with an interaction site reported to be located at EGFr 10-11 (Peters et al. 2004; Joutel et al. 2004). Upon ligand binding, a conformational change in the NRR uncovers the S2 cleavage site for the metalloproteases ADAM10 or ADAM17 and results in the release of the ECD. This enables a third cleavage by γ-secretase within the Notch3 transmembrane domain (S3-cleavage) (Xu et al. 2015), leading to nuclear translocation of the ICD and regulation of transcriptional downstream targets (Fouillade et al. 2013).

1.4.3   Pathomechanism

The core structure of each of the individual Notch3 EGFrs is formed by six conserved cysteine residues, forming three distinct disulfide bridges between cysteines 1 and 3, 2 and 4, and 5 and 6 (Figure 1.4). Pathogenic Notch3 mutations are exclusively located within one of the EGFrs (Chabriat et al. 2009) and are typically missense mutations affecting the conserved cysteine pattern, causing either the addition or the loss of a cysteine, and thereby resulting in an unpaired sulfhydryl group (Figure 1.4). Among diagnosed patients more than 230 different Notch3 cysteine mutations have been reported (Tikka et al. 2014) with the highest prevalence within EGFrs 1-6 (Coupland et al. 2018) (Figure 1.4). Recently, Rutten and colleagues have shown that mutations outside this region are associated with a milder phenotype and a significant lower MRI lesion load (Rutten et al. 2019). For some mutations within the EGFrs 7-34 they found an unexpected high frequency in the general population (1:300), suggesting that these mutations are less pathogenic or even non-penetrating.
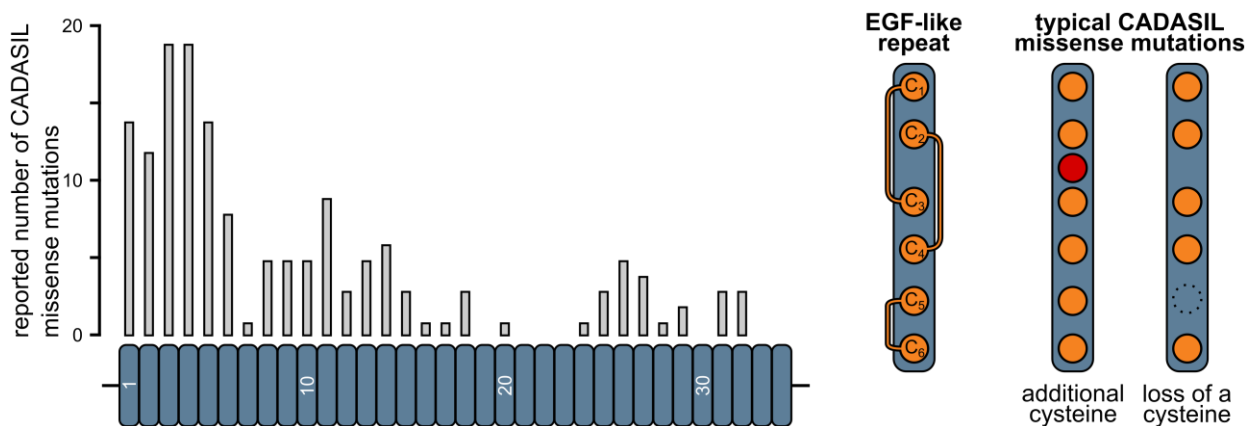
Figure 1.4: Frequency of CADASIL mutations in individual Notch3 EGF-like repeats (EGFrs) and typical mutation pattern. (**left**): Reported number of Notch3 missense mutations in the corresponding EGFr. (adapted from Coupland et al. 2018) (**right**): Within individual EGFrs six cysteine residues form three disulfide bridges between cysteines 1-3, 2-4 and 5-6. This pattern is lost by CADASIL-typical mutations causing either an addition (red circle) or a loss of a cysteine (dotted circle).

So far, the molecular mechanism underlying the pathological processes in CADASIL is only incompletely understood. Some findings argue for an involvement of Notch3 signaling in the disease mechanism. A recent study from Rutten and coworkers showed that mutations located in EGFr domains 10 and 11, comprising the ligand-binding domain and causing reduced Notch3 signaling, are associated with a higher white matter lesion load when compared to mutations in all other EGFr domains (Rutten et al. 2019). However, only 3.4% (14/ 412) of CADASIL patients of this cohort exhibited mutations in the ligand binding domain and the observed effect size was rather small. The majority of mutations are located outside the ligand binding domain, and for those, it is still controversial if and how these mutations affect Notch3 downstream signaling. While the R169C mutation was recently shown to result in increased Notch signaling in cerebral arteries of transgenic mice (Baron-Menguy et al. 2017), the C455R and R1031C mutations reduced signaling activity in isolated mouse fibroblasts (Arboleda-Velasquez et al. 2011). For several other CADASIL-typical Notch3 mutations no change in signaling activity could be observed *in vitro* (Cognat et al. 2014; Peters et al. 2004; Joutel et al. 2004). Interestingly, Notch3-knockout mice show vascular smooth muscle cell abnormalities (Fouillade et al. 2012), however this phenotype differs fundamentally from transgenic mice with a typical CADASIL mutation and can even be rescued by CADASIL-mutant Notch3 (Henshall et al. 2015; Liu et al. 2010; Monet et al. 2007). In patients, null mutations (frame-shift insertions/ deletions or nonsense mutations) have been identified only in very rare cases with leukoencephalopathy, but an otherwise incomplete CADASIL phenotype (Dotti et al. 2004; Pippucci et al. 2015; Schubert et al. 2018; Rutten et al. 2013). Strikingly, a compound heterozygous patient carrying a *NOTCH3* null mutation on one allele and a cysteine-altering Notch3 mutation (Y710C) on the other allele did not show a more severe phenotype (Rutten et al. 2013). In summary, a contribution of altered Notch3 signaling in CADASIL cannot be fully excluded, however, a loss-of-function mechanism as the sole or main cause of the disease disagrees with the majority of observations.

The stereotypic nature of CADASIL cysteine mutations, affecting the structure of Notch3^{ECD} and promoting its multimerization and aberrant accumulation around vascular smooth muscle cells and pericytes, is in line with a neomorphic effect (Chabriat et al. 2009; Monet-Lepretre et al. 2013) (Figure 1.5). As the formation of protein aggregates is a hallmark of several neurodegenerative diseases, including Alzheimer's disease, Parkinson disease, Huntington's disease, cerebral amyloid angiopathy, amyotrophic lateral sclerosis and frontotemporal dementia, it is reasonable to ask whether CADASIL could be a protein aggregation disease as well.
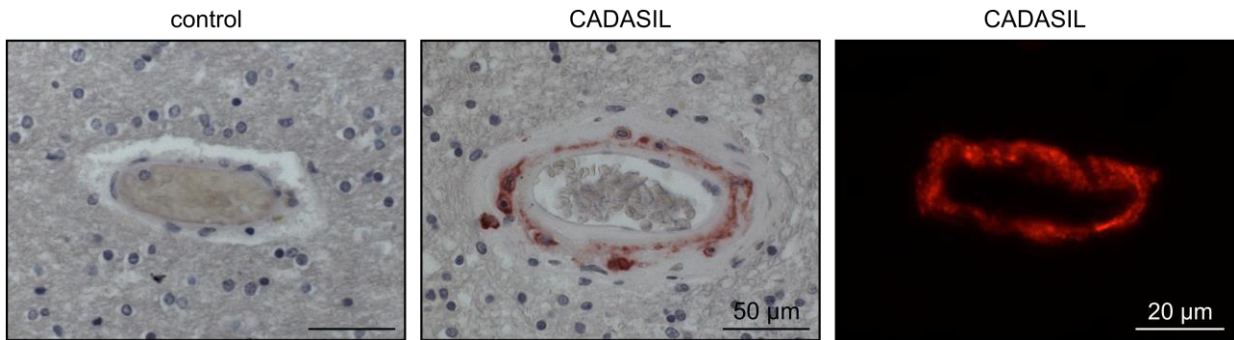
Figure 1.5: Accumulation of Notch3^{ECD} in brain vessels of a CADASIL patient. (**left**): Bright-field microscopy images of immunohistochemical stainings for Notch3^{ECD} of a CADASIL patient and a control subject vessel counterstained with hematoxylin. (**right**): Immunofluorescence staining for Notch3^{ECD} of a CADASIL patient vessel analyzed by confocal microscopy. (adapted from Kast et al., 2014)

Various observations support the involvement of pathological protein deposits in the molecular mechanism of the disease. The presence of so called granular osmiophilic material (GOM) located around vascular smooth muscle cells and pericytes (Baudrimont et al. 1993; Joutel et al. 2000) is a pathognomonic feature of CADASIL (Figure 1.6). GOM deposits can be visualized by electron microscopy as amyloid-negative structures of typically 0.2 to 0.8 µm composed of 10 to 15 nm granules (Kalimo et al. 2002). Although the exact distribution of GOM deposits is still elusive, a combination of immunolabeling and electron microscopy (immunogold EM) revealed that the ECD of Notch3 is a major component (Joutel et al. 2000; Ishiko et al. 2006) (Figure 1.6).
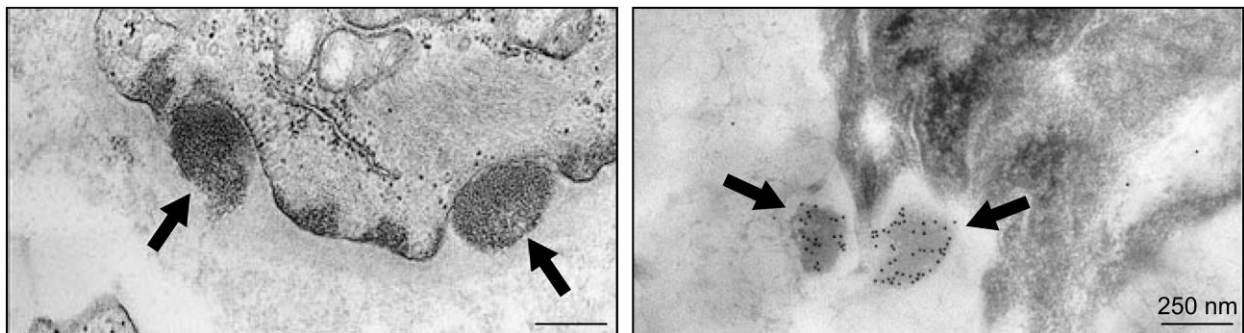
Figure 1.6: GOM deposition in CADASIL. (**left**): Electron microscopy of a dermal artery of a CADASIL patient depicts the deposition of granular osmiophilic material (GOM) at the plasma membrane of smooth muscle cells. (**right**): Immunogold labeling using an antibody against Notch3^{ECD} shows a distribution within GOM deposits. Arrows are pointing towards GOM deposits. (adapted from Ishiko et al., 2006)

In patients, GOM deposits appear more than a decade prior to neurological symptoms, presenting an early manifestation of the disease (Chabriat et al. 2009). This hypothesis is supported by data from a transgenic mouse model expressing rat Notch3^{R169C} which develop Notch3^{ECD} and GOM deposits much earlier than white matter lesions and cerebral blood flow deficits (Joutel et al. 2010). In the same model, Notch3^{ECD} deposition was reported to correlate with a reduction of pericyte

coverage and to be followed by reduced expression of endothelial adherens junction proteins, blood-brain barrier leakage and reduced microvascular CO_2-reactivity (Ghosh et al. 2015).

Recent evidence suggests that the aggregation of Notch3[ECD] facilitates the interaction with additional proteins, promoting its accumulation and sequestration into GOM deposits. It has been reported that various ECM factors, including tissue inhibitor of metalloproteinases 3 (TIMP3), vitronectin, LTBP-1, endostatin, clusterin, decorin, biglycan and serum amyloid P-component (APCS) are enriched in CADASIL patient vessels and colocalize with Notch3[ECD] deposits (Craggs et al. 2016; Kast et al. 2014; Lee et al. 2014; Monet-Lepretre et al. 2013; Nagatoshi et al. 2017; Zhang et al. 2015; Arboleda-Velasquez et al. 2011). Their recruitment suggests a dysregulation of their biological activity and a contribution of impaired ECM homeostasis in CADASIL pathogenesis (Monet-Lepretre et al. 2013; Joutel et al. 2016).

1.5 CAA

Cerebral amyloid angiopathy (CAA) is a common, age-related cerebral SVD characterized by the deposition of amyloid β (Aβ) peptide in the walls of small and medium-sized leptomeningeal and cortical arteries, arterioles, capillaries and less frequently also veins (Charidimou et al. 2017). Its prevalence is 20-40% in non-demented and 50-60% in the demented elderly population (Keage et al. 2009). In addition, CAA can be detected in 85-95% of patients with Alzheimer's disease (Charidimou et al. 2017). The main clinical manifestations are intracerebral hemorrhage, cognitive impairment and dementia (Viswanathan et al. 2011). Typical MRI features include multiple, strictly lobar cerebral microbleeds, white matter hyperintensities and cortical microinfarcts.

Depending on the size of the affected vessels, CAA can be divided in two subtypes: type 1, characterized by Aβ deposits in cortical capillaries (with or without the involvement of leptomeningeal, and cortical arteries, arterioles, veins, and venules) and type 2, showing Aβ pathology exclusively in leptomeningeal and cortical vessels, without the involvement of capillaries (Thal et al. 2002). Apart from Aβ accumulation, fibrinoid necrosis, a loss of vascular smooth muscle cells and vessel wall thickening, degenerative processes also observed in ischemic SVD, can be detected upon neuropathological examination (Attems et al. 2011). CAA occurs mostly sporadic, but similar to AD, it is strongly associated with variants of apoliprotein E (APOE). APOE plays a crucial role in lipid metabolism and occurs in three isoforms (ε2, ε3 and ε4) differing at two amino acid positions due to two common polymorphisms. APOE ε4 and, to a

lesser extent APOE ε2, have been shown to increase both vascular amyloid accumulation as well as the risk of developing CAA-related hemorrhages (Greenberg et al. 1998; Nelson et al. 2013).

Aβ peptides are derived by sequential cleavage of the amyloid precursor protein (APP) by β- and γ-secretase (Figure 1.7) and are highly prone to form oligomers, fibrils and finally amyloid plaques (Selkoe 2001). While in AD, these plaques are predominantly composed of the 42-amino acid fragment (Aβ$_{42}$), the vascular amyloid deposits in CAA mainly consist of Aβ$_{40}$ (Charidimou et al. 2012).
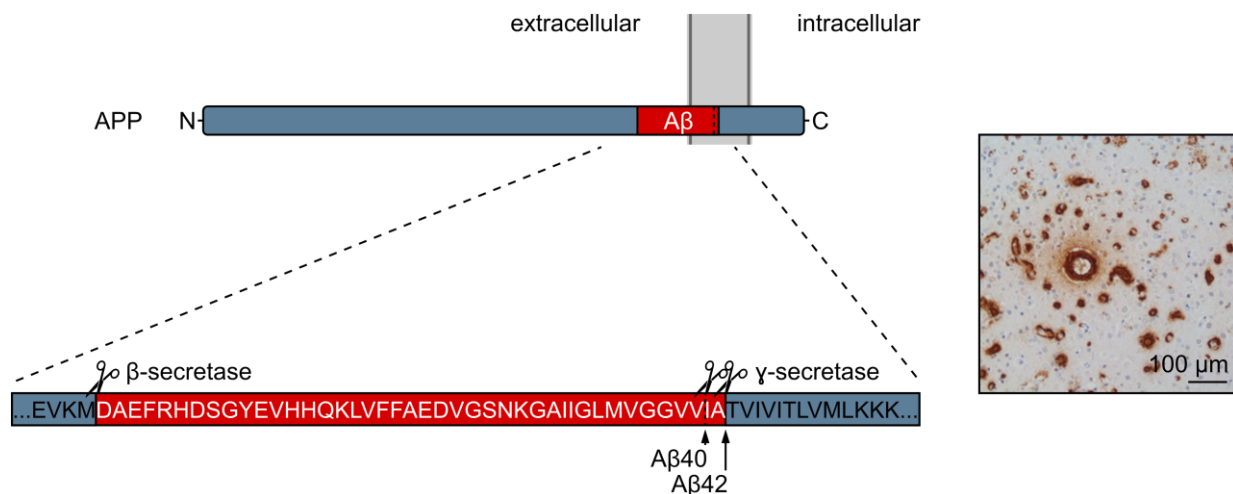
Figure 1.7: Aβ generation and accumulation in CAA. (left): Processing of amyloid precursor protein (APP) first by β-secretase and then γ-secretase releases the amyloid beta (Aβ) peptides Aβ$_{40}$ and Aβ$_{42}$. (**right**): Deposition of Aβ peptides in brain vessel walls of a CAA patient. (adapted from Hondius et al., 2018)

Experimental studies in transgenic mouse models provided evidence that vascular Aβ is primarily of neuronal origin and its accumulation largely the result of an impaired clearance rather than increased production (Charidimou et al. 2017). The so-called *drainage hypothesis* suggests that under normal conditions neuronal produced Aβ drains with the interstitial fluid along the basement membrane and between smooth muscle cells out of the brain. It is proposed, that with aging or under pathological conditions this clearance mechanism can fail, initiating an increase in trapping and finally the deposition of Aβ in brain vessel walls (Carare et al. 2013; Weller et al. 2015; Rasmussen et al. 2018).

Recent proteomic studies have identified several proteins enriched in CAA. Among these, APOE and clusterin (also known as apoliprotein J), which were reported to interact with Aβ and influence its aggregation and clearance (Endo et al. 2019; DeMattos et al. 2004; Wojtas et al. 2017). Sushi repeat-containing protein X-linked (SRPX) has just recently been shown to directly interact with

Aβ *in vitro* and to accumulate in vascular, but not in parenchymal amyloid deposits (Inoue et al. 2017). In addition, SRPX mRNA levels were found to be increased after Aβ stimulation and to promote Aβ-induced apoptosis in cerebrovascular smooth muscle cells. APCS is a plasma glycoprotein which can be found in all forms of amyloid aggregates (Pepys 2018) including Aβ deposits (Hondius et al. 2018), but was also reported to accumulate in CADASIL (Craggs et al. 2016). The prevention of its accumulation is currently under pharmacological investigation (Pepys 2015). Interestingly, HTRA1 was reported to accumulate in parenchymal (Grau et al. 2005) but also in cerebrovascular amyloid deposits (Hondius et al. 2018) and was shown to be involvement in Aβ degradation (Poepsel et al. 2015; Grau et al. 2005; Tennstaedt et al. 2012). These data indicate the presence of common mechanisms in cerebral small vessels diseases, but no consistent picture about pathological pathways has emerged yet.

1.6 Aims of this thesis

In both CADASIL and CAA the formation of insoluble protein deposits in brain vessels is considered as the initiating event of a pathological cascade of events resulting in vessel degeneration and dysfunction. The molecular processes mediating the toxicity of protein aggregates are poorly understood. Previous proteomic studies performed on human samples aiming at identifying disease-relevant processes were hampered by a number of weaknesses including limited numbers of samples, varying sources of vascular material, low mass spectrometry sensitivity and lack of true data quantification.

To overcome these limitations in this study, a vessel isolation technique yielding highly pure fractions of small and medium-sized brain vessels from post-mortem autopsy samples will be combined with state-of-the-art liquid chromatography coupled with tandem mass spectrometry and followed by label-free quantification. Results will be verified by different techniques such as immunoblotting and immunofluorescence staining as well as *in vitro* and cellular approaches. Further, the proteomic signatures obtained from CADASIL and CAA samples will be compared to search for possible commonalities. Thus, this study aims to elucidate novel molecular pathways underlying CADASIL and CAA pathogenesis and the identification of molecular targets relevant for pharmacological intervention.

2 MATERIAL AND METHODS

2.1 Equipment and consumables

Table 2.1: Equipment

Equipment	Manufacturer
Automated cell counter TC20	Bio-Rad Laboratories
Biological safety cabinet class II Herasafe KS	Thermo Fisher Scientific
C18 column (30 cm/ 50 cm $\times$ 75 µm ID)	Dr. Maisch
C18 extraction disks (47 mm) Empore	SUPELCO
Cell culture CO_2 incubator CB150	Binder
Cell storage tank CryoPlus	Thermo Fisher Scientific
Confocal laser scanning microscope LSM 800	Carl Zeiss
Cryostat CM1950	Leica Biosystems
Freeze dryer Coolsafe 110-4	ScanVac
Freezer -20 °C MediLine	Liebherr
Freezer -80 °C HERAfreeze	Thermo Fisher Scientific
Freezing container Mr. Frosty	Thermo Fisher Scientific
Fridge 4 °C MediLine	Liebherr
Fusion FX7 imaging system	Vilber Lourmat Deutschland
Gel electrophoresis System Mini-Protean	Bio-Rad Laboratories
Gel imaging system E-BOX VX2	Vilber Lourmat
Gelsystem PerfectBlue Mini L	PEQLAB
Ion source Nanospray Flex	Thermo Fisher Scientific
Liquid chromatograph EASY-nLC 1000	Thermo Fisher Scientific
Liquid chromatograph EASY-nLC 1200	Thermo Fisher Scientific
Mass spectrometer Q-Exactive	Thermo Fisher Scientific
Mass spectrometer Q-Exactive HF	Thermo Fisher Scientific
MaXtract High Density 2 ml tubes	QIAGEN
Microplate absorbance reader iMark	Bio-Rad Laboratories
Microscope (inverted) Eclipse TS100	Nikon Instruments
Microwave	C. Bomann
Millipore water machine Milli-Q	Merck
Overhead shaker Reax 2	Heidolph Instruments
Power supply Peqpower 250	PEQLAB
Power supply PowerPac HC	Bio-Rad Laboratories
Precellys 24 tissue homogenizer	Bertin Instruments
qPCR system LightCycler 480	Roche Diagnostics
Refrigerated centrifuge 5810	Eppendorf

Table 2.1: Equipment (continued)

Equipment	Manufacturer
Refrigerated centrifuge Avanti J25	Beckmann-Coulter
Refrigerated centrifuge Heraeus Megafuge 40	Thermo Fisher Scientific
Refrigerated microcentrifuge 5424	Eppendorf
Shaking incubator Certomat BS-1	Sartorius
Simple Western WES	ProteinSimple
Sonicator VialTweeter	Hielscher Ultrasonic
Sonicator water bath S 10/H	Elma Schmidbauer
Spectrophotometer NanoDrop ND-1000	PEQLAB
Thermal cycler C1000 Touch	Bio-Rad Laboratories
Thermoshaker basic	CellMedia
Thermoshaker MKR23	DITABIS Digital Biomedical Imaging Systems
Tissue grinder (1 ml) Wheaton	DWK Life Sciences
Tissue potter (10 ml) Wheaton	DWK Life Sciences
Vacuum centrifuge MaxiVac	ScanVac
Western Blotting cell Mini Trans-Blot	Bio-Rad Laboratories

Table 2.2: Consumables

Consumable	Manufacturer
6-Well cell culture plate (sterile)	BD Falcon
96-Well plate clear flat-bottom (nonsterile)	Thermo Fisher Scientific
Cell counting slides for TC20	Bio-Rad Laboratories
Cell strainer, nylon (40 µm)	BD Falcon
Conical tube (15 ml)	BD Falcon
Conical tube (50 ml)	BD Falcon
Cryogenic tube Nunc (1.8 ml)	Thermo Fisher Scientific
Liquid-repellent slide marker pen	Science Services
Microscope cover glass Menzel 24 x 50 mm #1	Thermo Fisher Scientific
Microscope slide SuperFrost Plus	Thermo Fisher Scientific
Microtome Surgipath DB80 LX blades	Leica Biosystems
Nitrocellulose membrane Amersham Protran 0.2 µm	GE Healthcare
Petri dish (10 cm)	Greiner Bio-One
Precellys homogenization tubes (CK14/ 0,5 ml)	Bertin Instruments
Protein LoBind tubes 0.5 ml	Eppendorf
Protein LoBind tubes 1.5 ml	Eppendorf
Scalpel (No. 21)	FEATHER
Serological pipette 10 ml	Greiner Bio-One
Serological pipette 25 ml	Greiner Bio-One

Table 2.2: Consumables (continued)

Consumable	Manufacturer
Spin filter Amicon Ultra 0.5 ml (3.000 MWCO)	Merck
Spin filters Vivacon 500 (30.000 MWCO)	Sartorius
Tissue culture flask T80 Nunc	Thermo Fisher Scientific
Tissue culture flask TripleFlask Nunc	Thermo Fisher Scientific
Tubes Safe-Lock 0.5 ml	Eppendorf
Tubes Safe-Lock 1.5 ml	Eppendorf

2.2 Kits

Table 2.3: Kits

Kit	Manufacturer
High Pure PCR product purification kit	Roche Diagnostics
Ionic detergent compatability reagent	Thermo Fisher Scientific
NucleoBond Xtra Midi	MACHERY-NAGEL
NucleoSpin Plasmid	MACHERY-NAGEL
Omniscript RT kit	QIAGEN
Pierce 660 nm protein assay reagent	Thermo Fisher Scientific
Pierce BCA protein assay kit	Thermo Fisher Scientific
RNeasy Mini kit	QIAGEN

2.3 Chemicals and reagents

Table 2.4: Chemicals and reagents

Chemical/ Reagent	Manufacturer
2-Propanol (Isopropanol)	Sigma-Aldrich
4′,6-diamidin-2-phenylindol	Sigma-Aldrich
Acetone (99.5% for synthesis)	AppliChem
Acetonitrile (ULC/MS – CC/SCF)	Biosolve
Acrylamide/Bis solution, 37.5:1 (30%)	SERVA
Agarose peqGOLD Universal	PEQLAB
Ammonium bicarbonate	Sigma-Aldrich
Ammonium persulfate	Sigma-Aldrich
Ampicillin	Sigma-Aldrich
Antarctic phosphatase	New England Biolabs
Aqueous mounting medium Fluoromount	Sigma-Aldrich
Bovine serum albumin	Sigma-Aldrich
Cryo embedding compound Tissue-Tek OCT	Sakura

Table 2.4: Chemicals and reagents (continued)

Chemical/ Reagent	Manufacturer
Dimethyl sulfoxide	Sigma-Aldrich
Dithiothreitol	Sigma-Aldrich
Dithiothreitol (for SDT buffer)	GE Healthcare
DMEM high glucose, GlutaMAX supplemented	Thermo Fisher Scientific
DNA gel stain SYBR Safe	Thermo Fisher Scientific
DNA ladder peqGOLD 1 kb	PEQLAB
DNA polymerization mix dNTPs (10 mM each)	GE Healthcare
Ethanol (gradient grade for liquid chromatography)	Merck
Fetal bovine serum	Thermo Fisher Scientific
Ficoll PM400	Sigma-Aldrich
Formic acid 0.1% in water (ULC/MS – CC/SCF)	Biosolve
Gel loading dye, purple (6X)	New England Biolabs
HaloLink resin	Promega
HaloTEV protease	Promega
Heparin Natrium 5000 (25,000 units/ ml)	Ratiopharm
HTRA1 inhibitor NVP-LBG976	Novartis
IGEPAL CA-630	Sigma-Aldrich
Iodoacetamide	Sigma-Aldrich
Kanamycin monosulfate	Sigma-Aldrich
Ketamine hydrochloride Ketavet (100 mg/ ml)	Pfizer
Laemmli sample buffer (4x)	Bio-Rad Laboratories
LightCycler 480 probes master mix	Roche Diagnostics
Lipofectamin 2000	Thermo Fisher Scientific
LysC (mass spec grade)	Promega
MEM (no glutamine)	Thermo Fisher Scientific
Opti-MEM reduced serum medium	Thermo Fisher Scientific
Penicillin-streptomycin (10,000 U/ ml)	Thermo Fisher Scientific
Peptone from casein	Carl Roth
Pfu DNA polymerase	Agilent
Phosphate buffered saline	Klinikum der Universität München
Polyethylenimine (linear, MW 25,000 Da)	Sigma-Aldrich
Poly-L-lysine solution (0.01%)	Thermo Fisher Scientific
Ponceau S solution (0.1%)	Sigma-Aldrich
Protein marker Precision Plus Protein (prestained)	Bio-Rad Laboratories
QIAzol lysis reagent	QIAGEN
Random hexamer primer (50 µM)	Thermo Fisher Scientific
ReproSil-Pur 120 C18-AQ, 1.9 µm	Dr. Maisch

Table 2.4: Chemicals and reagents (continued)

Chemical/ Reagent	Manufacturer
Restriction enzyme EcoRI-HF	New England Biolabs
Restriction enzyme KpnI-HF	New England Biolabs
Restriction enzyme NotI-HF	New England Biolabs
Restriction enzyme XbaI	New England Biolabs
Restriction enzyme XhoI	New England Biolabs
RNase-Free DNase	QIAGEN
Sera-Mag SpeedBead hydrophobic	GE Healthcare
Sera-Mag SpeedBead hydrophylic	GE Healthcare
Skim milk powder	Sigma-Aldrich
Sodium chloride	Carl Roth
Sodium dodecyl sulfate	SERVA
Sodium dodecyl sulfate (for SDT buffer)	Sigma-Aldrich
T4 DNA ligase	New England Biolabs
TaqMan probe GAPDH (Hs02786624_g1)	Thermo Fisher Scientific
TaqMan probe HTRA1 (Hs01016151_m1)	Thermo Fisher Scientific
TaqMan probe RPLP0 (Hs99999902_m1)	Thermo Fisher Scientific
TBE buffer (10x)	Carl Roth
Tetramethylethylenediame	Carl Roth
Tris base (Trizma)	Sigma-Aldrich
Tris ultrapure (for SDT buffer)	AppliChem
Trypsin (sequencing grade)	Promega
Trypsin-EDTA (0.05%) (phenol red)	Thermo Fisher Scientific
Tween 20	Carl Roth
UREA (GR for analysis)	Merck
Water (ULC/MS – CC/SCF)	Biosolve
Western HRP substrate Immobilon	Merck
Xylazinhydrochlorid 20 mg/ ml	Akorn
Yeast extract	Carl Roth

2.4   Software

Table 2.5: Software

Software	Manufacturer
Compass for SW (version 3.1.7)	ProteinSimple
ImageJ (version 1.60)	NIH
Ingenuity Pathway Analysis (version 2.1)	QIAGEN N.V.
Maxquant software (version 1.5.2.8/ 1.5.4.1/ 1.6.6.0)	Max-Planck-Institute of Biochemistry
SigmaPlot (version 13.0)	Systat Software

2.5   DNA techniques

2.5.1   Plasmids

Plasmids used and generated in this thesis are listed in Table 2.6. Subcloning was performed by restriction digest and ligation. If necessary, restriction sites were added to the insert via overhang-PCR (see 2.5.2).

Table 2.6: List of plasmids

Name	Gene/ Insert	Source
pcDNA4/TO	mammalian expression vector without insert	Thermo Fisher Scientific
pTT5/N3$^{EGF 1-5}$-Halo	truncated human Notch3 with EGF repeats 1-5 fused to a C-terminal Halo tag	Patrizia Fresser
pcDNA6/HTRA1-V5/His	human HTRA1 fused to a C-terminal V5/His tag	Nathalie Beaufort
pcDNA6/HTRA1^{S328A}-V5/His	human HTRA1 containing the active-site mutation S328A (c.982T>G) fused to a C-terminal V5/His tag	Nathalie Beaufort
pcDNA3.1/HTRA1-Myc/His	human HTRA1 fused to a C-terminal Myc/His tag	Mahmoud A. Pouladi
pcDNA3.1/HTRA1^{S270Lfs*69}	human HTRA1 containing the S270Lfs*69 mutation (c.805_806insG)	Mahmoud A. Pouladi
pcDNA6/HTRA1^{S270Lfs*69}-V5/His	human HTRA1 containing the S270Lfs*69 mutation (c.805_806insG) fused to a C-terminal V5/His tag	Subcloning (HindIII/XhoI)
pTT5/HTRA1-Halo	human HTRA1 fused to a C-terminal Halo tag	Subcloning (XbaI/EcoRI)
pTT5/HTRA1^{S328A}-Halo	human HTRA1 containing the active-site mutation S328A (c.982T>G) fused to a C-terminal Halo tag	Subcloning (XbaI/EcoRI)
pcDNA3.2/CEMIP	human CEMIP	Giancarlo Marra (Tiwari et al. 2013)
pcDNA4/TO/CEMIP-Myc/His	human CEMIP fused to a C-terminal Myc/His tag	Subcloning (KpnI/XhoI)

Table 2.6: List of plasmids (continued)

Name	Gene/ Insert	Source
cDNA/CHRD	human CHRD (cDNA clone MGC: 133038)	Source Bioscience
pcDNA4/TO/CHRD-Myc/His	human CHRD fused to a C-terminal Myc/His tag	Subcloning (EcoRI/XhoI)
pTT3/VTN-Bio/His	human VTN fused to a C-terminal rat CD4 d3+4/His tag	Addgene: #53429
pcDNA4/TO/VTN- Myc/His	human VTN fused to a C-terminal Myc/His tag	Subcloning (NotI/XbaI)
pcDNA4/TO/LTBP-1ΔC-Myc/His	C-terminally truncated human LTBP-1 (aa1-1689) fused to a C-terminal Myc/His tag	Nathalie Beaufort (Beaufort et al. 2014)
cDNA/SEMA3G	human SEMA3G (cDNA clone MGC: 119471)	Source Bioscience
pcDNA4/TO/SEMA3G-Myc/His	human SEMA3G fused to a C-terminal Myc/His tag	Subcloning (EcoRI/XbaI)
pcDNA4/TO/N3$^{EGF 1-15}$-Myc/His	human Notch3 EGF repeats 1-15 fused to a C-terminal Myc/His tag	Marco Düring (Duering et al. 2011)
pRK5M/TIMP3-Myc	human TIMP3 fused to a C-terminal Myc tag	Addgene: #31715
pCMV3/OLFML3-Myc	human OLFML3 fused to a C-terminal Myc tag	SinoBiologicals

2.5.2 Polymerase chain reaction (PCR)

PCR was used to amplify DNA sequences and to add specific restriction sites using primer overhangs (Table 2.10). Standard reaction and cycle conditions are shown in Table 2.7 and Table 2.8. The amplified PCR product was purified using the High Pure PCR product purification kit (Roche Diagnostics) according to the manufacturer's instructions. DNA concentration was determined using the NanoDrop ND-1000 spectrophotometer (PEQLAB).

Table 2.7: PCR reaction mixture

Component	Volume
native Pfu polymerase buffer (10x)	5 µl
template	50 ng
dNTPs (10 mM)	1 µl
forward primer (10 µM)	2.5 µl
reverse primer (10 µM)	2.5 µl
DMSO	2.5 µl
native Pfu polymerase (2.5 U/ µl)	1 µl
Millipore water	ad 50 µl

Table 2.8: PCR cycling parameters

	Temperature	Period		
denaturation	95 °C	3 min		
denaturation	95 °C	30 s		
annealing	55-60 °C	45 s		30 cycles
elongation	72 °C	1 min/ 1 kbp		
elongation	72 °C	10 min		
storage	4 °C	∞		

2.5.3 DNA restriction digestion

Preparative restriction digestion was performed according to the enzymes manufacturer's instructions. All enzymes were purchased from New England Biolabs. Reaction was performed at 37 °C for 1 h. Table 2.9 shows a standard restriction reaction mix.

Table 2.9: Reaction mix for preparative DNA restriction

Component	Amount
DNA	1-5 µg
restriction buffer (10x)	2 µl
restriction enzyme 1	10 U/ µg DNA
restriction enzyme 2	10 U/ µg DNA
Millipore water	ad 20 µl

2.5.4 Oligonucleotides

Oligonucleotides used for PCR (2.5.2) were synthesized by Metabion International AG, Planegg, Germany and are listed in Table 2.10.

Table 2.10: List of oligonucleotides

Name	Sequence 5' to 3'
CHRD Fwd-EcoRI	TG**GAATTC**GCCCTTCACCC
CHRD Rev-XhoI	CC**CTCGAG**AGAGCCTTCGGCTTCTTTCT
HTRA1^{S270Lfs*69} Fwd	GCAGCGACGCCAACACCTAC
HTRA1^{S270Lfs*69} Rev-XhoI	GC**CTCGAG**CCGTCCAGGTTTACTAA
SEMA3G Fwd-EcoRI	CA**GAATTC**GCCCTTCACCAT
SEMA3G Rev-XbaI	CC**TCTAGA**CGTGGCCTCCACCTCCC
VTN Fwd	ATGACATCCACTTTGCCTTT
VTN Rev-XbaI	CC**CTCTAGA**GAGATGGCCAGGGGCAGGAC

Underlined base pairs display primer overhangs, bold letters illustrate restriction sites.

2.5.5   Vector dephosphorylation

To avoid the religation of the restricted vector, its 5' phosphate groups were removed by Antarctic phosphatase (New England Biolabs) incubated for 30 min at 37 °C. Table 2.11 shows the reaction mixture for dephosphorylation. For inactivation of the enzyme, the reaction mixture was subsequently incubated for 5 min at 65 °C.

Table 2.11:   Reaction mixture for dephosphorylation

Component	Amount
DNA	1-5 µg
Antarctic phosphatase buffer (10x)	3 µl
Antarctic phosphatase	1 µl
Millipore water	ad 30 µl

2.5.6   Agarose gel electrophoresis

PCR products and digested vectors were separated by gel electrophoresis to remove template DNA or uncut vector. Depending on the size of the fragment, DNA was separated in 0.7–1.5% agarose gels. An appropriate amount of agarose was dissolved in TBE buffer via boiling in the microwave. Prior gel casting SYBR Safe DNA gel stain (Thermo Fisher Scientific) was added (1:10,000). DNA samples were supplemented with gel loading dye (New England Biolabs) and separated with a constant voltage of 100 V for 1-2 h. As a molecular marker peqGOLD DNA ladder mix (100-10,000 bp) (PEQLAB) was used. DNA bands were visualized by the Gel imaging system E-BOX VX2 (Vilber Lourmat).

To extract DNA from agarose gel, the GeneJET gel extraction kit (Fermentas) was used according to the manufacturer's instructions. Yield and purity were determined by NanoDrop ND-1000 spectrophotometer (PEQLAB).

2.5.7   Ligation

Ligation was performed with 50 ng of vector and a threefold molar excess of insert using T4 DNA ligase (New England Biolabs) in a total reaction volume of 20 µl incubated for 1 h at RT. Ligation mixture was either stored at -20 °C or directly used for bacterial transformation (see 2.5.8.)

2.5.8 Transformation of competent bacteria (Heat Shock Method)

Vector transformation into bacteria was used for the replication of plasmid DNA. Therefore, all mammalian expression constructs used in this study carry a bacterial origin of replication and an antibiotic resistance.

Lysogeny broth (LB) medium: 1% (w/v) peptone, 0.5% (w/v) yeast extract, 0.5% (w/v) NaCl

LB agar plates: LB medium with 1.5% (w/v) agarose

Competent bacteria (50 µl, E. coli DH5α) stored at -80 °C were thawed on ice, mixed with 50 ng of plasmid DNA or up to 5 µl of ligation mixture and incubated for 30 min on ice. Heat shock was performed for 90 s at 42 °C followed by a subsequent 2 min incubation on ice. Bacteria were first outgrown by adding 200 µl of LB medium without antibiotics for 1 h at 37 °C and 900 rpm before plating onto LB agar containing the appropriate antibiotic (Ampicillin 100 µg/ml; Kanamycin 50 µg/ml). After an overnight incubation at 37 °C, colonies were picked and further grown in preparation for plasmid isolation (see 2.5.9). Liquid cultures were grown at 37 °C and 230 rpm agitation in a bacterial shaker.

For long-term storage of transformed bacteria, a glycerol stock was prepared by mixing 1 volume of 50% (v/v) glycerol in Millipore water to 1 volume of a bacteria suspension and subsequently transferring to -80 °C. To recover bacteria from a glycerol stock, a pipet tip was used to scratch some of the frozen bacteria off of the top and to inoculate a culture.

2.5.9 Plasmid DNA isolation of bacteria

Plasmid DNA was isolated from bacteria by using the kits NucleoSpin Plasmid and NucleoBond Xtra Midi (MACHERY-NAGEL) according to manufacturer's instructions. The concentration and purity were determined by NanoDrop ND-1000 spectrophotometer (PEQLAB). Sequencing was performed by GATC Biotech AG, Konstanz, Germany.

2.5.10 Real-time quantitative PCR

Human brain samples (50-100 mg) were pulverized using liquid nitrogen and RNA was extracted with QIAzol Lysis Reagent and the MaXtract high density tubes (QIAGEN) according to the manufacturer's instructions. Genomic DNA was removed by incubation with RNase-Free DNase (QIAGEN) for 30 min at 37 °C followed by column purification with the RNeasy Mini kit

(QIAGEN) following the manufacturer's protocol. Quantity and quality was checked using the NanoDrop ND-1000 spectrophotometer (PEQLAB). For cDNA synthesis, 750 ng of RNA, random hexamers (Thermo Fisher Scientific) and the Omniscript RT kit (QIAGEN) were used according to the manufacturer's instructions. For qPCR, 1% of cDNA was analyzed in a LightCycler 480 (Roche Diagnostics) using the following TaqMan probes: HTRA1 (#4331182), RPLP0 (#4326314E) and GAPDH (#4331182) (all from Thermo Fisher Scientific). Samples were run in triplicates and expression levels were normalized to RPLP0 and GAPDH.

2.6 Brain tissue

2.6.1 Human brain samples

Cryo-conserved human brain autopsy samples from six CADASIL patients, three patients diagnosed with sporadic cerebral small vessel disease (SVD), 15 CAA patients as well as 14 control subjects were provided by the Brain-Net Biobank (Ludwig-Maximilians-University Munich), by A. Joutel (Université Paris-Diderot), by S. Lesnik-Oberstein (Leiden University Medical Center) and by the Netherlands Brain Bank (Netherlands Institute for Neuroscience, Amsterdam; www.brainbank.nl). All material has been collected from donors for or from whom a written informed consent for a brain autopsy and the use of the material and clinical information for research purposes had been obtained.

The *NOTCH3* mutations in the CADASIL patients are genetically confirmed, SVD patients were clinically diagnosed with vascular dementia and CAA patients are histopathologically characterized. For the control subjects no cerebrovascular disorder was documented. The presence of pathogenic *HTRA1* mutations was excluded in four of the six CADASIL patients (CAD 1–3, 6), by sequencing all nine exons of the gene. Sequencing was performed by the Medizinisch Genetisches Zentrum (MGZ), Munich, Germany.

2.6.2 Mouse brain samples

HTRA1 deficient brain samples were obtained from a previously described knockout mouse strain with C57BL/6 J background (Jones et al. 2011). A group of five HTRA1$^{-/-}$ and five HTRA1$^{+/+}$ animals at the age of 20 months was used for proteomic analysis. Matings were performed heterozygously. For tissue collection, animals were first anesthetized by ketamine/ xylazine

injection (90-120 mg/ kg ketamine, 6-8 mg/ kg xylazine) and then transcardially perfused with heparin solution and PBS (5 ml 25 U/ ml followed by 5 ml 12.5 U/ ml and 10 ml PBS). Brains were harvested, immediately frozen on dry ice and stored at -80 °C until use. Animal experiments were performed by Dr. Eva Neubauer (ISD, Munich), in accordance with the german animal welfare law and approved by the government of upper bavaria.

2.6.3 Isolation of brain vessels

The isolation of cerebral vessels from human or murine brains was essentially based on previous protocols (Monet-Lepretre et al. 2013; Yousif et al. 2007). Briefly, human frontal lobe (100 mg) or one hemisphere of murine brain was minced with a scalpel and homogenized in 15 ml cold minimum essential medium (MEM) using a glass tissue potter and 100-150 up and down strokes. An equal volume of 30% (w/v) Ficoll/ MEM solution was added and centrifuged at $6,000 \times g$ for 20 min at 4 °C. The supernatant was discarded, and the resulting pellet was vigorously resuspended in 1% (w/v) bovine serum albumin (BSA) diluted in PBS, transferred onto a 40 µm nylon mesh and washed with 250 ml cold PBS. Vessels were collected by flushing the inverted nylon mesh with PBS and centrifugation at $3,000 \times g$ for 5 min at 4 °C. The pellet was transferred to a protein LoBind tube and the purity was checked by light microscopy. Impure isolations were discarded. To prevent adherence of isolated vessels to surfaces, plastic material was coated with a solution of 1% (w/v) BSA in PBS.

Isolated vessels were further preceded for immunofluorescence staining or for the preparation of protein extracts. For the latter, isolated vessels were centrifuged at $3,000 \times g$ for 5 min at 4 °C, the supernatant was removed, and the pellet was immediately frozen on dry ice and stored at -80 °C until use.

2.6.4 Vessel protein extraction

SDT lysis buffer: 4% (w/v) SDS, 100 mM Tris–HCl pH 7.6, 100 mM DTT

Protein extraction of isolated vessels was performed in SDT lysis buffer. For CADASIL, sporadic SVD and murine samples, homogenization was performed with a dounce tissue grinder. For the CAA study, samples were processed by Precellys tissue homogenizer (5x 30 s, 10,000 rpm, 30 s pause). Homogenates were heated for 3 min at 95 °C and subsequently sonicated (5 times, 30 s, amplitude 100%, duty cycle 50%) with intermediate cooling using the VialTweeter sonicator

(Hielscher). Lysates were cleared by centrifugation at $16,000 \times g$ for 15 min and protein concentration was measured using the colorimetric 660-nm assay supplemented with the ionic detergent compatibility reagent (Thermo Fisher Scientific) according to the manufacturer's instructions.

2.7 Proteomic analysis (LC-MS/MS)

Proteomic measurements were performed in cooperation with Dr. Stephan Müller, Anna Berghofer and Prof. Dr. Stefan Lichtenthaler (DZNE, Munich).

A protein amount of 15 µg from human or mouse vessel lysates was subjected to proteolytic trypsin digestion using the filter-assisted sample preparation (FASP) (Wisniewski et al. 2009) and spin filters with a 30-kDa cut-off (Sartorius) (for CADASIL and mouse samples) or a modified single-pot solid-phase-enhanced sample preparation (SP3) protocol (Cox et al. 2014; Hughes et al. 2019) (for CAA samples). Resulting peptides were desalted, dried by vacuum centrifugation and dissolved in 20 µl 0.1% (v/v) formic acid.

For the analysis of CADASIL or mouse samples, 1.3 µg peptides were separated on a nanoLC system (EASY-nLC 1000, Thermo Fisher Scientific) using an in-house packed C18 column (30 cm column length for human and 50 cm for mouse samples) with a binary gradient of water and acetonitrile (ACN) containing 0.1% (v/v) formic acid: 0 min, 2% (v/v) ACN; 5 min, 5% (v/v) ACN; 185 min, 25% (v/v) ACN; 230 min, 35% (v/v) ACN; 250 min, 60% (v/v) ACN; 255 min, 95% (v/v) ACN; 270 min, 95% (v/v) ACN. For the analysis of CAA samples, 1.0 µg of peptides were separated on an advanced nanoLC system (EASY-nLC 1200, Thermo Fisher Scientific), using the C18 column with 30 cm column length and a shortened binary gradient: 0 min, 2.4% (v/v) ACN; 2 min, 4.8% (v/v) ACN; 92 min, 24% (v/v) ACN; 112 min, 35.2% (v/v) ACN; 121 min, 60% (v/v) ACN. For all, column temperature was set to 50 °C and flow rate to 250 nl/ min. Chromatography was coupled online to a Q-Exactive (or Q-Exative HF for the analysis of CAA samples) mass spectrometer via a nanospray flex ion source equipped with a column oven (Sonation). Using the Q-Exactive, full MS spectra were acquired at a resolution of 70,000. The top 10 peptide ions, exceeding an intensity of 1.5×10^4, were chosen for collision induced dissociation and fragment ion spectra were acquired at a resolution of 17,500. With the Q-Exactive HF, full MS spectra were acquired at a resolution of 120,000 and the top 15 peptide ions were chosen for higher-energy c-trap dissociation with a normalized collision energy of 26%.

Resulting fragment ions spectra were acquired at a resolution of 15,000. For all, a dynamic exclusion of 120 s was used for peptide fragmentation.

For data analysis, the Maxquant software (Cox et al. 2014) (version 1.5.4.1 [CADASIL]/ 1.5.2.8 [mouse]/ 1.6.6.0 [CAA]) was used, searching against a reviewed canonical FASTA database of Homo sapiens (UniProt, download: CADASIL [July 11th, 2016; 20,203 entries], CAA [June 12th 2019; 20962 entries]) or Mus musculus (UniProt, download: December 12th, 2014; 16,685 entries). Two missed trypsin cleavages were allowed for database search. To recalibrate the peptide masses within a window of 20 ppm, the option first search was used. Main search was performed for peptides and peptide fragments within a mass tolerances of 4.5 and 20 ppm respectively. N-terminal acetylation and oxidation of methionine were set as variable modifications, carbamidomethylation of cysteine as static modifications. The false discovery rate (FDR) was adjusted to less than 1% for both peptides and proteins. For label-free quantification (LFQ) of proteins, at least two ratio counts of unique peptides were required. To determine the significance of protein abundance changes, LFQ intensities were $\log_2$-transformed and a two-sided Student's t-test was applied (in the mouse experiment mean LFQ intensities of two technical replicates were calculated beforehand). Relative quantification and statistical analysis were performed for proteins identified in at least three samples of each group using the following significance threshold: p-value < 0.05 and $\log_2$ LFQ ratios > 0.4 and < -0.4 (corresponding to ~1.32-fold and ~0.76-fold changes). Multivariate statistical analysis was performed as indicated using a FDR threshold of 0.05. Over-representation of UniProt subcellular location information was analyzed by a two-tailed Fisher's exact test and significance of the protein overlap using the hypergeometric test.

2.8 Cell culture

2.8.1 Cell maintenance and cryo-conservation

Human embryonic kidney (HEK) 293 cells (ATCC CRL-1573) and HEK293E cells (Duering et al. 2011) were maintained in high glucose dulbecco's modified eagle's medium (DMEM), supplemented with GlutaMAX and sodium pyruvate, 10% (v/v) fetal bovine serum (FBS) and 100 U/ ml penicillin–streptomycin at 37 °C and 5% CO_2. Cells were sub-cultured when 80-90% confluency was reached using the following procedure: Medium was removed, and the cell layer was washed with PBS. Trypsin-EDTA solution was added and incubated for 2 min at 37 °C.

Detached cells were centrifuged at $400 \times g$ for 5 min and resuspended in fresh media. Finally, an appropriate number of cells were seeded in a new culture flask. The typical split ratio for HEK293 cells was 1:10 every 3-4 days. If a distinct number of cells was required for the experiment, cell number was determined using the automated cell counter TC20 (Bio-Rad Laboratories).

For long-term storage, cells were resuspended in culture medium supplemented with 10% (v/v) DMSO and 50% (v/v) FBS (final concentrations), subsequently transferred into cryogenic tubes and gradually frozen in a freezing container (Mr. Frosty, Thermo Fisher Scientific) placed at -80 °C for 24 h. The next day, tubes were transferred into liquid nitrogen tank. For thawing, cryogenic tubes were placed in a water bath at 37 °C and subsequently diluted (1:10) in culture medium as soon as the last ice crystal has melted. After centrifugation at $400 \times g$ for 5 min cells were resuspended in culture medium, plated in a cell culture flask and maintained routinely.

2.8.2 Cell transfection

2.8.2.1 Small-scale transfection

HEK293 cells were seeded on poly-l-lysine-coated 6-well plates. Coating was performed by adding 0.01% (w/v) poly-l-lysine solution for 15 min at RT, followed by two washes with autoclaved Millipore water and subsequent drying. A number of 1.3×10^6 cells were seeded 24 h prior to transfection. The next day, medium was changed to culture medium without penicillin-streptomycin supplementation and 1 µg plasmid DNA was transiently transfected using Lipofectamine 2000 (Thermo Fisher Scientific) according to the manufacturer's instructions. 5 h after transfection, medium was replaced by serum-free medium without FBS or penicillin-streptomycin supplementation and after further 24 to 48 h, conditioned medium was collected and cleared by centrifugation at $1{,}000 \times g$ for 5 min. Supernatant was either directly used for experiments or stored at -20 °C.

2.8.2.2 Large-scale transfection

Polyethylenimine (1 mg/ ml):   100 mg polyethylenimine dissolved in 100 ml Millipore water, adjusted with

1M HCl to pH 7.0, sterile filtered (0.2 μm), aliquoted and stored at -80 °C

For the purification of proteins, HEK293E cells were seeded in TripleFlasks (Thermo Fisher Scientific) with a total growth area of 500 cm^2. 2.7×10^7 cells were plated in a volume of 90 ml one day prior to transfection. The next day, medium was changed to culture medium containing 2.5% (v/v) FBS without penicillin-streptomycin supplementation. Transfection procedure was performed according to the following procedure: 75 μg of plasmid DNA was diluted in 3 ml OptiMEM medium, mixed with 300 μl polyethylenimine solution (1 mg/ ml) and incubated for 25 min at RT before added to the cell medium. The next day, medium was changed to culture medium without FBS or penicillin-streptomycin supplementation. Conditioned medium was collected after further 72 h, cleared by centrifugation at $1,000 \times g$ for 5 min and subsequently used for purification purpose (see 2.9.6).

2.9   Protein analysis

2.9.1   Antibodies

Primary and secondary antibodies used in this thesis are listed in Table 2.12 and Table 2.13. The monoclonal antibodies against Notch3^{ECD} (clones 5E1 and 3G6) were kind gifts of A. Joutel and E. Kremmer respectively.

Table 2.12: List of primary antibodies

Antibody	Species	Type	Dilution	Manufacturer
anti-Aß (6E10)	rouse	mAb	IF 1:300; WB 1:1,000	BioLegend
anti-CEMIP (45750002)	rabbit	pAb	WB 1:500	Novus Biological
anti-Collagen IV (1340-01)	goat	pAb	IF 1:1,000	SouthernBiotech
anti-HTRA1 (HPA036655)	rabbit	pAb	WES 1:50; WB 1:5,000	Sigma-Aldrich
anti-HTRA1 (MAB2916)	mouse	mAb	IF 1:50	R&D Systems
anti-LTBP-1 (MAB388)	mouse	mAb	WB 1:500	Novus Biological
anti-MYC (9E10)	mouse	mAb	WB 1:4,000	Santa Cruz Biotechnology
anti-Notch3 (3G6)	rat	mAb	IF 1:100	E. Kremmer (Duering et al. 2011)
anti-Notch3 (5E1)	mouse	mAb	IF 1:250	A. Joutel (Joutel et al. 2000)
anti-ß-actin (A2066)	rabbit	pAb	WB 1:1,000	Sigma-Aldrich
anti-TIMP3 (D74B10)	rabbit	mAb	WB 1:1,000	Cell Signaling
anti-V5 (R960-25)	mouse	mAb	WB 1:10,000	Thermo Fisher Scientific

mAb: Monoclonal antibody; pAb: Polyclonal antibody; WB: Western Blotting; IF: Immunofluorescence; WES: Simple Western (ProteinSimple)

Table 2.13: List of secondary antibodies

Antibody	Species	Conjugate	Dilution	Manufacturer
anti-goat (ab150135)	donkey	Alexa 488	IF 1:500	Abcam
anti-mouse (ab150110)	donkey	Alexa 555	IF 1:500	Abcam
anti-rat (ab2340696)	donkey	Alexa 647	IF 1:500	Jackson ImmunoResearch
anti-mouse (7076)	goat	HRP	WB 1:10,000	Cell Signaling Technology
anti-rabbit (7074)	horse	HRP	WB 1:10,000	Cell Signaling Technology

WB: Western Blotting; IF: Immunofluorescence; AF: Alexa Fluor

2.9.2 SDS-PAGE

Running buffer: 25 mM Tris, 192 mM glycine, 1% (w/v) SDS

Protein lysates and conditioned supernatants were size-fractioned by sulfate polyacrylamide gel electrophoresis (SDS-PAGE) under denaturing and reducing conditions using the discontinuous Mini-Protrean system (Bio-Rad Laboratories) according to the manufacturer's instructions. The compositions of the stacking and separation gels are shown in Table 2.14. Prior to electrophoresis, samples were mixed with 4x Laemmli sample buffer (Bio-Rad Laboratories) and DTT (100 mM final concentration) and boiled for 5 min at 95 °C. Electrophoresis was performed with 80 to 160 V in running buffer.

Table 2.14: Composition of stacking and separation gels

	Separating gel				Stacking gel
Solution	7.5%	10%	12.5%	15%	5%
Acrylamid/ Bis Solution, 37.5:1 (30%)	2.5 ml	3.3 ml	4.2 ml	5.0 ml	0.8 ml
Tris-HCL 1.5M pH 8.8	2.5 ml	2.5 ml	2.5 ml	2.5 ml	-
Tris-HCL 0.5M pH 6.8	-	-	-	-	1.3 ml
Millipore water	4.8 ml	4.0 ml	3.1 ml	2.3 ml	2.8 ml
SDS (10%)	100 µl	100 µl	100 µl	100 µl	50 µl
APS (10%)	100 µl	100 µl	100 µl	100 µl	50 µl
TEMED	10 µl	10 µl	10 µl	10 µl	5 µl

Volumes are sufficient for two gels. SDS: Sodium dodecyl sulfate; APS: Ammonium persulfat;
TEMED: Tetramethylethylenediame

2.9.3 Western Blotting

Blotting buffer: 25 mM Tris, 192 mM glycine, 20% (v/v) methanol

TBS-T: 10 mM Tris-HCl pH 8.0, 150 mM NaCl, 0.05% (v/v) Tween 20

Blocking buffer: 4% (w/v) skim milk powder in TBS-T

Proteins separated by SDS-PAGE were transferred onto a 0.2 µm nitrocellulose membrane using the Mini Trans-Blot system (Bio-Rad Laboratories) according to the manufacturer's instructions. Transfer was performed at 100 V for 90 min at 4 °C. To verify protein transfer, membranes were

stained using 0.1% (w/v) Ponceau S solution (Sigma-Aldrich) according to the manufacturer's instructions. After washing and destaining with TBS-T, membranes were incubated in blocking buffer for 1 h at RT. Primary antibodies (Table 2.12) were diluted in blocking buffer and incubated overnight at 4 °C under constant shaking. The next day, membranes were washed tree times for 5 min with TBS-T, followed by a 1 h incubation with the appropriate HRP-conjugated secondary antibody (Table 2.13) diluted in blocking buffer. After washing 3 times for 5 min with TBS-T, chemiluminescence signal was detected using the Immobilon western HRP substrat (Merck) and the chemiluminescence imaging system Fusion FX7 (Vilber Lourmat). For quantification, signal intensity was analyzed using ImageJ software.

2.9.4 Immunofluorescence staining of isolated vessels and brain sections

Human brain sections of 16 µm thickness were prepared using the cryostat CM1950 (Leica Biosystems). Cutting temperature was between -17 °C and -21 °C with a temperature difference between the cutting blade and the specimen holder of -1 °C. Sections were stored at -80 °C until further analysis.

For immunofluorescence analysis, isolated vessels were supplemented with BSA up to a final concentration of 0.2% (w/v), transferred onto a microscope slide and dried at room temperature (RT). Cryosections were removed from -80 °C and thawed at RT for 10 min. For fixation and permeabilization, an incubation in 100% ice cold aceton (-20 °C) was performed for 10 min at -20 °C. Subsequently, slides were washed 3 times for 5 min with PBS. Sections or immobilized vessels were encircled with a liquid-repellent slide marker pen, providing a hydrophobic barrier. To reduce unspecific binding, blocking buffer (5% (w/v) BSA in PBS) was added for 1 h at RT. Next, slides were shortly dipped in PBS before applying the primary antibodies diluted in 0.2% (w/v) BSA in PBS. Primary antibody incubation was performed overnight at 4 °C with the antibodies listed in Table 2.12. The next day, slides were washed 3 times with PBS for 5 min and fluorophore-coupled secondary antibodies (Table 2.13) were diluted in 0.2% (w/v) BSA in PBS and added for 1 h at RT. Slides were washed and simultaneously incubated with DAPI solution using the following procedure: PBS for 5 min, DAPI (1:10,000 in PBS) for 5 min, PBS for 5 min, Millipore water for 5 min. Finally, slides were mounted with aqueous mounting media (Fluoromount, Sigma-Aldrich) and images were captured by inverted fluorescence or confocal microscopy.

2.9.5   HTRA1 proteolysis assays

HTRA1 protease as well as the potential substrates was expressed using transiently transfected HEK293 cells (see 2.8.2.1). To ensure roughly equal substrate concentrations, protein levels of conditioned supernatants were first determined by Western Blotting (see 2.9.3) with a Myc tag specific antibody and then adjusted respectively using Amicon Ultra centrifugal filters with a 3-kDa cut-off (Merck). The coincubation of conditioned supernatants was performed in a thermoshaker at 300 rpm and 37 °C for 24 h. Protein levels were determined by Western Blotting (see 2.9.3). Recombinant HTRA1 and HTRA1^{S328A} proteins were purified by HaloTag technology (see 2.9.6) and applied at a final concentration of 100 nM. For some experiments, a HTRA1-specific inhibitor (NVP-LBG976, Novartis) (Grau et al. 2005) was used at a final concentration of 5 µM.

2.9.6   **Protein purification**

Phosphate buffered saline (PBS):	154 mM NaCl, 9.5 mM Na$_2$HPO$_4$, 1.7 mM KHPO$_4$, pH 7.4
Purification buffer:	0.01% (v/v) IGEPAL CA-630 in PBS
Cleavage solution:	30 µl HaloTEV Protease in 1 ml purification buffer

Recombinant HTRA1 and HTRA1^{S328A} were purified using the HaloTag protein purification system (Promega) with a modified protocol. Proteins were expressed in HEK293E cells (see 2.8.2.2) and subsequently purified from the condition media. 750 µl of resuspended HaloLink resin were centrifuged at $1,000 \times g$ for 5 min at RT, supernatant was discarded, and the settled beads (25% bed volume) were washed 3 times with 10 ml purification buffer and subsequent centrifugation at $1,000 \times g$ for 5 min at RT. Beads were than resuspended in the original volume of 750 µl purification buffer and added to the conditioned supernatant for an overnight incubation at 4 °C with overhead rotation. The next day, beads were centrifuged at $1,000 \times g$ for 5 min at 4 °C and supernatant was discarded. Washing was performed as described above. For the elution of the recombinant proteins, settled beads were resuspended in 750 µl of cleavage solution containing HaloTEV protease and incubated for 1 h at RT with overhead rotation. Supernatant (elution fraction 1) was collected by centrifugation at $1,000 \times g$ for 5 min at 4 °C and loaded onto a spin column to remove residual HaloLink resin. Spin columns were centrifuged at $10,000 \times g$ for 5 min at 4 °C. The settled beads were again resuspended in 750 µl purification buffer and rotated overhead for 30 min at RT. Supernatant (elution fraction 2) was cleared by centrifugation and spin column purification was performed as described above. Concentration of purified proteins was

determined using the BCA protein assay kit (Thermo Fisher Scientific) according to the manufacturer's instructions. Proteins were stored at -80 °C for further usage.

2.10 Statistical analysis

For group vise comparative statistical analysis, the two-tailed Student's *t*-test was used. For proteomic analysis, relative quantification as well as statistical analysis was performed for proteins identified in at least three samples of each group. Protein abundance changes with a $\log_2$ LFQ ratio > 0.4 or < -0.4 (corresponding to ~1.32-fold and ~0.76-fold changes) and a *p*-value below 0.05 were considered as statistically significant. Multiple comparison correction was performed as indicated using a FDR threshold of 0.05. To determine the statistical significance of the proteomic profile overlap, hypergeometric test was used and for over-representation analysis according to UniProt subcellular location information, a two-tailed Fisher's exact test was applied. The following UniProt subcellular location information were used (download: May 15th, 2017): cell membrane (SL-0039), extracellular space (SL-0112), mitochondrion (SL-0173), nucleus (SL-0191), secreted (SL-0243). Only reviewed entries were considered.

3 RESULTS

The aggregation of Notch3^{ECD} and formation of Notch3^{ECD}-containing GOM deposits in brain vessel walls are defining features of the hereditary stroke disorder CADASIL. While Notch3^{ECD} is known as major GOM constituent (Joutel et al. 2000; Ishiko et al. 2006), other components of these large protein deposits as well as the downstream processes resulting in vessel degeneration and dysfunction are incompletely defined. A major goal of this thesis was the biochemical characterization of vessels isolated from post-mortem brain samples of CADASIL patients in order to identify novel proteins and pathways contributing to disease pathogenesis. To that end, a proteomic approach was applied to quantitatively determine disease-relevant protein abundance changes.

3.1 CADASIL post-mortem brain samples

Cryopreserved human brain autopsy samples from six CADASIL patients (mean age 64.3 ± 4.6 years) and six age- and sex-matched control subjects (mean age 61.3 ± 6.1 years) were used. Table 3.1 displays their main characteristics.

Table 3.1: Main characteristics of brain autopsy samples from CADASIL patients and control subjects

Sample ID	Sex	Age	Notch3 mutation	affected EGFr	Brain region
CADASIL 1	male	64	R110C	EGFr 2	frontal lobe
CADASIL 2	female	66	D239_D253del	EGFr 6	frontal lobe
CADASIL 3	male	68	C144S	EGFr 3	frontal lobe
CADASIL 4	female	60	R153C	EGFr 3	frontal lobe
CADASIL 5	female	70	C1261R	EGFr 32	frontal lobe
CADASIL 6	female	58	R153C	EGFr 3	frontal lobe
Control 1	male	61	-	-	frontal lobe
Control 2	female	55	-	-	frontal lobe
Control 3	female	60	-	-	frontal lobe
Control 4	female	73	-	-	frontal lobe
Control 5	male	60	-	-	frontal lobe
Control 6	female	59	-	-	frontal lobe

EGFr: Epidermal growth factor (EGF)-like repeat

Pathogenic Notch3 mutations invariably locate in one of the 34 EGFrs of the Notch3^{ECD} and among diagnosed patients, 70% are found in EGFrs 1-6 (Coupland et al. 2018). Autopsy samples used for this study were obtained from patients carrying mutations in EGFr 2 (R110C), EGFr 3 (C144S and R153C), EGFr 6 (D239_D253del) and EGFr 32 (C1261R) and thus display a representative

spectrum of characteristic mutations. All of them result in an uneven number of cysteine residues, either by the addition (R110C and R153C) or the loss of a cysteine (C144S and C1261R), and were previously described to cause typical CADASIL symptoms (Joutel et al. 1997; Dichgans et al. 2001; Dichgans et al. 2000). The mutation D239_D253del is resulting in the deletion of 15 amino acids (D239 to D253) comprising three cysteine residues (C240, C245 and C251).

3.2 Brain vessel isolation and immunofluorescence staining of Notch3[ECD] deposits

To isolate vessels from cryopreserved human autopsy samples, a technique was used, which had been developed previously (Monet-Lepretre et al. 2013; Yousif et al. 2007) and subsequently established in our lab by Kast and coworkers (Kast et al. 2014). The procedure comprises mild tissue homogenization, Ficoll gradient centrifugation and nylon mesh filtration and results in the efficient removal of non-vascular material and the isolation of highly pure vessels (Figure 3.1).
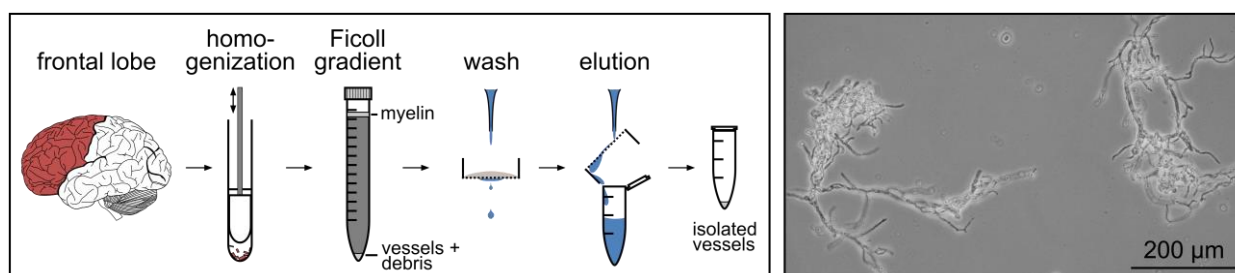
Figure 3.1: Isolation of human brain vessels. (**left**): Cerebral vessels were isolated from cryopreserved human autopsy material by tissue homogenization, Ficoll gradient centrifugation and nylon mesh filtration. (**right**): Light microscopy image of isolated vessels demonstrating high purity.

This procedure resulted in the isolation of intact vessels and provided the opportunity for improved analysis by immunofluorescence staining. Therefore, a labeling protocol was developed which included the immobilization of isolated vessels on a silica surface, antibody staining and imaging by high-resolution confocal microscopy. Figure 3.2 shows an immunofluorescence staining from a control sample for the basement membrane marker collagen type IV applied to isolated brain vessels in comparison to whole-brain cryosections. Staining for vascular proteins using isolated vessels represents a major advancement compared to section-based methods, as it allows three-dimensional visualization of whole vessels and eliminates background signal usually arising from surrounding tissue.
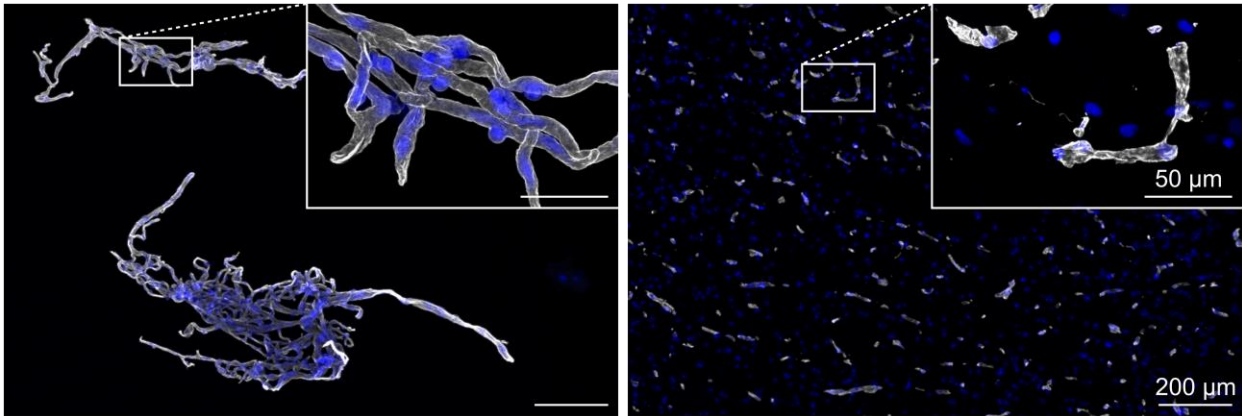
Figure 3.2: Immunofluorescence staining of isolated brain vessels in comparison to cryostat sections. Brain vessels of a control subject were visualized by staining for the basement membrane marker collagen type IV (pseudo-colored in white) and cell nuclei (blue) in isolated brain vessels (**left**) and 16 µm thick cryosections (**right**) using confocal microscopy.

Using an antibody against Notch3^{ECD} revealed widespread granular immunoreactivity in brain vessels from a CADASIL patient, while there was no detectable staining in a control subject (Figure 3.3). Thus, this technique provides a powerful tool to visualize vascular pathological deposits and to study the spatial relationship of proteins expected to emerge from the proteomic study.
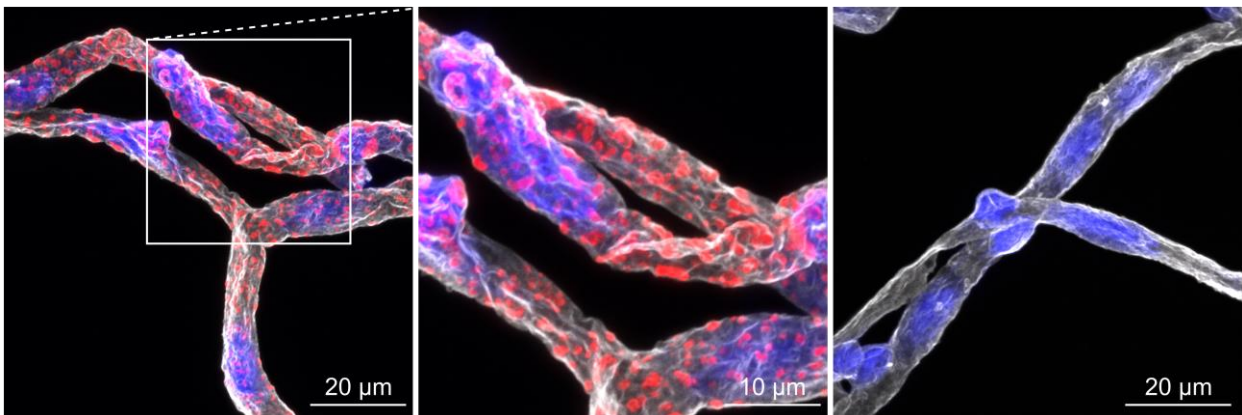
Figure 3.3: Immunofluorescence staining of Notch3^{ECD} deposits in isolated brain capillaries. Confocal microscopy images from (**left, middle**) a CADASIL patient and (**right**) a control subject stained for collagen IV (pseudocolored in white), Notch3^{ECD} (red) and cell nuclei (blue).

3.3 The CADASIL brain vessel proteome

Recent evidence suggests that the misfolding and aggregation of Notch3[ECD] cause the recruitment and sequestration of various additional proteins resulting in their accumulation (Monet-Lepretre et al. 2013). Over the last years, a number of studies have identified several proteins enriched in CADASIL (Craggs et al. 2016; Kast et al. 2014; Lee et al. 2014; Monet-Lepretre et al. 2013; Nagatoshi et al. 2017; Zhang et al. 2015; Arboleda-Velasquez et al. 2011), however a comprehensive understanding of proteome alterations has not been achieved. Liquid chromatography coupled with tandem mass spectrometry (LC-MS/MS) was used to analyze isolated brain vessel extracts from CADASIL patients and control subjects.

3.3.1 LC-MS/MS analysis

Vessels preparations from six CADASIL patients and six age-matched control subjects were solubilized using a stringent lysis buffer including high concentrations of detergent (4% SDS) and reducing agent (100 mM DTT), sonication and heat denaturation. 15 µg of total protein extracts were used for tryptic digestion and peptides were separated by nanoLC and their masses determined using a quadrupole-Orbitrap mass spectrometer (in collaboration with Dr. Stephan Müller and Prof. Dr. Stefan Lichtenthaler, DZNE, Munich). Relative abundance changes were calculated using label-free quantification (LFQ) by the MaxQuant software (Cox et al. 2014). In total, 5092 proteins were identified by two or more unique peptides. 3339 proteins were detected in at least three samples of both the patient and the control group and used for calculation of abundance ratios and for statistical analysis (Figure 3.4). 190 of the quantified proteins (labeled in red) showed a p-value of < 0.05 and a $\log_2$ abundance ratio (CADASIL vs. control) of > 0.4 (~1.32-fold) or < -0.4 (~0.76-fold), with an equal number of enriched and depleted proteins (for a complete list of significantly altered proteins see Appendix, Table 5.1). However, the extent of enrichment (up to 145-fold) was considerably larger than that of depletion (up to 5.9-fold), which is in agreement with the hypothesis of excessive protein accumulation as key feature in CADASIL.
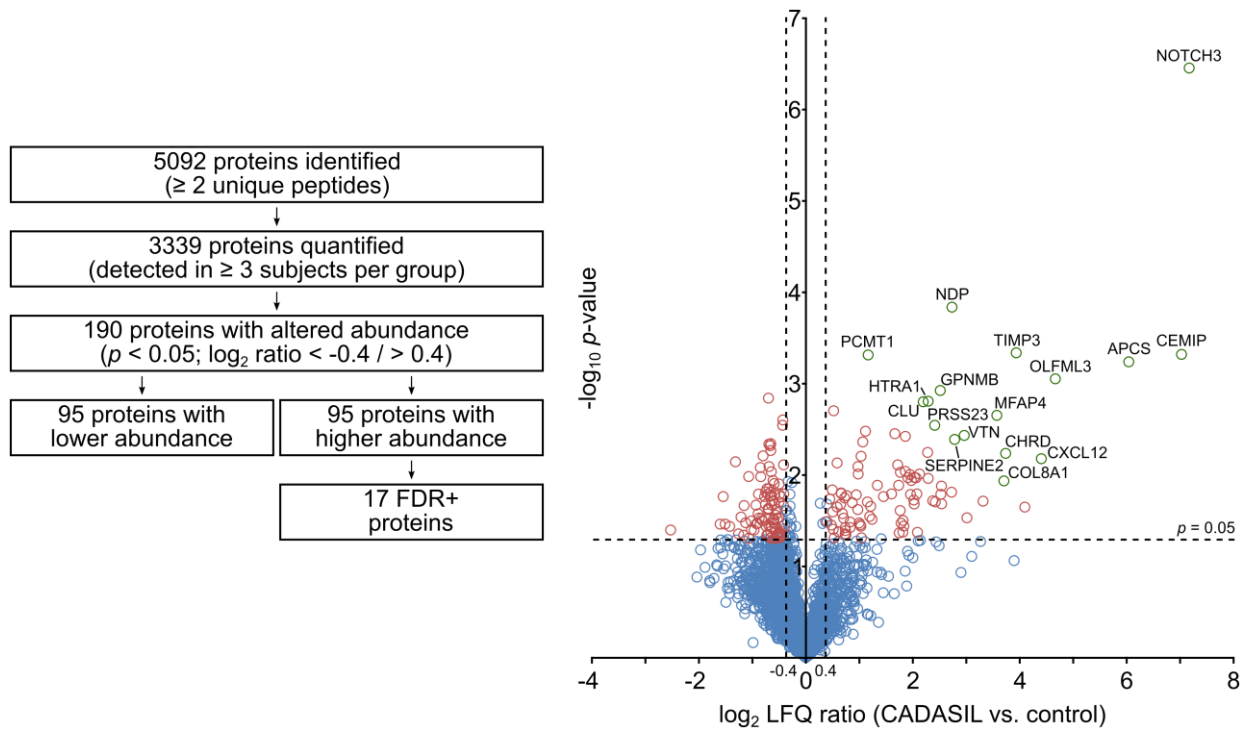
Figure 3.4: Proteomic analysis of isolated brain vessels from CADASIL patients and control subjects. (**left**): Summary of LC-MS/MS and label-free quantification (LFQ) results. (**right**): Volcano plot of $\log_2$ LFQ ratios (CADASIL vs. control) and $-\log_{10}$ p-values of all quantified proteins. Red circles indicate proteins with a significant change in abundance ($p < 0.05$, $\log_2$ ratio $< -0.4 / > 0.4$). Proteins labeled as green circles passed multivariate statistical analysis (FDR = 0.05, S0 = 0.3).

In line with its accumulation in CADASIL brain vessels, the protein with the strongest abundance increase was Notch3, showing an accumulation of 145-fold in comparison to controls. Mapping of the identified peptides within its primary sequence revealed coverage of all domains, but clearly showed that the peptide intensities were much higher in the extracellular domain than in the intracellular region (Figure 3.5). This for the first time provided mass spectrometry confirmation of the widely accepted fact that the accumulation of Notch3 is restricted to its extracellular domain, a finding, which has so far only been shown by antibody-based techniques (Joutel et al. 2000; Ishiko et al. 2006).
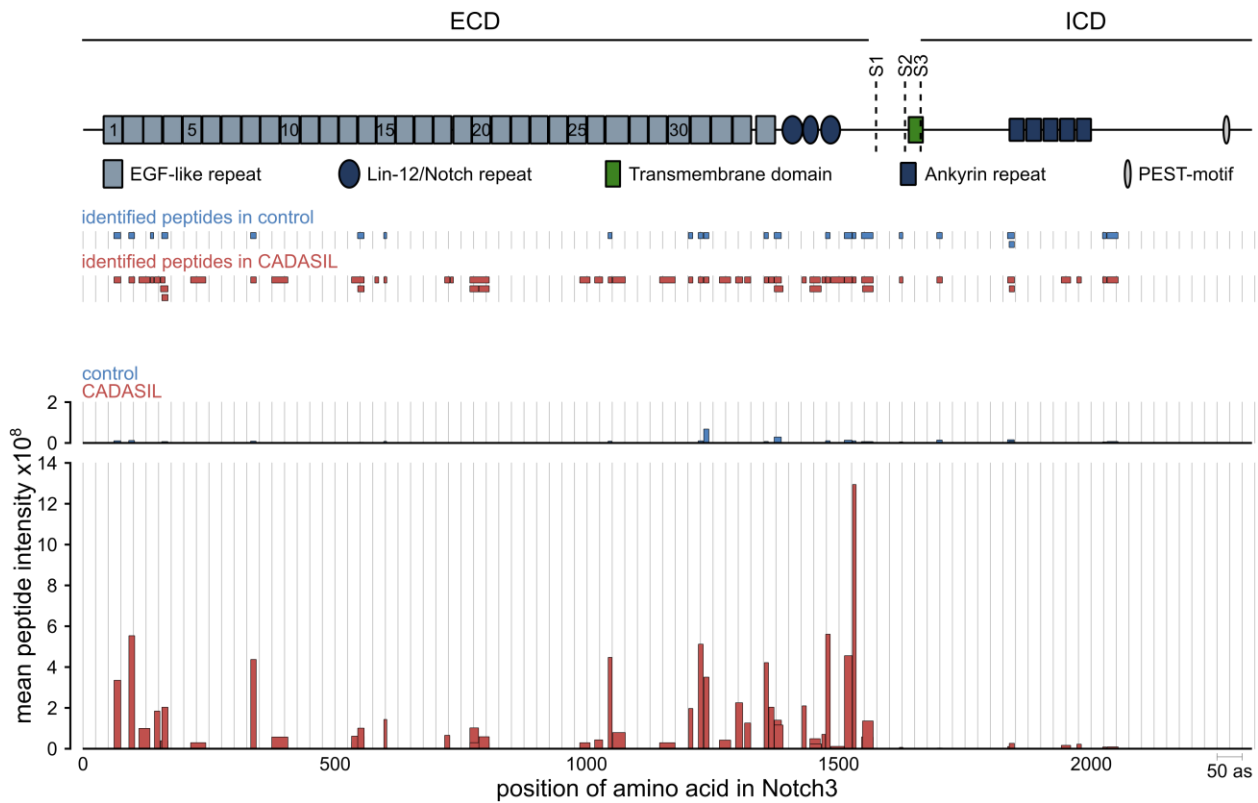
Figure 3.5: Notch3 accumulation in CADASIL vessels is restricted to its extracellular domain. (**top**): Domain cartoon of Notch3 and mapping of peptides identified by LC-MS/MS in CADASIL patients (red) and control subjects (blue). (**bottom**): Mean intensities of Notch3 peptides depicted above. ECD: extracellular domain; ICD: intracellular domain

3.3.2 Enrichment of secreted and extracellular matrix proteins

Categorization of all 3339 statistically evaluated proteins according to subcellular localization information from the UniProt database demonstrated that all major cellular compartments were represented (Figure 3.6, left panel). A comparison between the group of significantly altered proteins and all quantified proteins revealed a strong overrepresentation of the categories "extracellular space" (~6-fold, $p = 1.3 \times 10^{-19}$), "secreted" (~4-fold, $p = 4.1 \times 10^{-23}$) and "mitochondrion" (~2-fold, $p = 6.4 \times 10^{-8}$) (Figure 3.6, right panel).
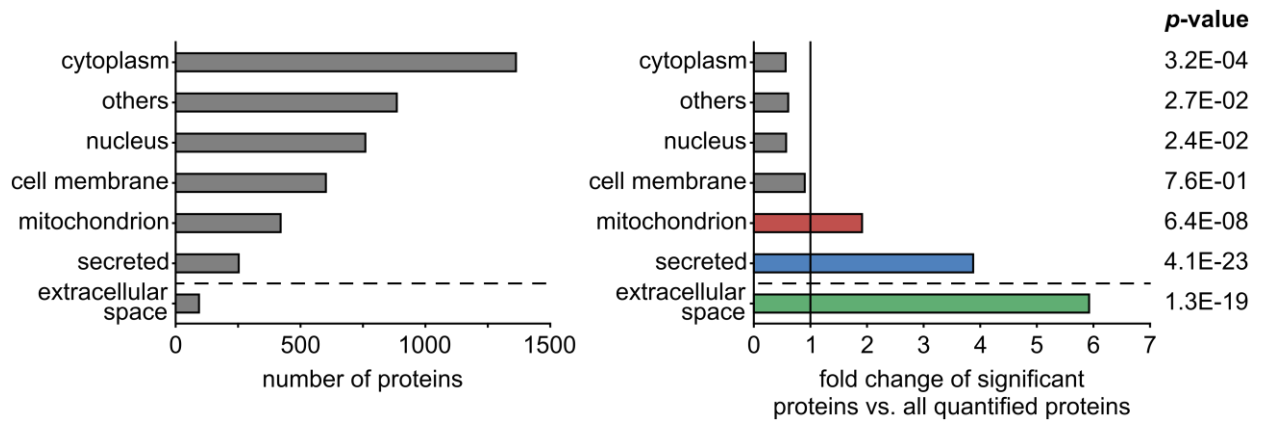
Figure 3.6: Overrepresentation of mitochondrial, secreted and extracellular space proteins in CADASIL brain vessels. (**left**): Classification of the 3339 quantified proteins according to UniProt subcellular location information. (**right**): Over- / underrepresentation of significantly altered proteins within each category. *p*-values were calculated by Fisher's exact test. The category of extracellular space proteins represents a subgroup of secreted proteins.

Interestingly, all significantly altered mitochondrial proteins (with only a single exception) were depleted (Figure 3.7) and Ingenuity pathway analysis revealed "oxidative phosphorylation" as significantly affected pathway ($p = 2.8 \times 10^{-15}$), indicating a reduction in energy metabolism. In contrast, the vast majority of secreted (89%, 50/56) and extracellular space proteins (84%, 27/32) were enriched, including various collagens (COL1A1, COL1A2, COL6A1, COL6A2, COL8A1, COL12A1), proteoglycans (biglycan, decorin, lumican, mimecan), structural components (fibrillin-1, fibulin-1, fibulin-2, elastin) and a number of other matrisomal proteins (Figure 3.7). This was in line with the extracellular location of GOM deposits and the matrisome hypothesis of CADASIL pathogenesis (Joutel et al. 2016). The small number of secreted and extracellular space proteins with lower abundance (6.8%, 6/88) included the three hyaluronan-binding proteoglycans versican, brevican and neurocan as well as the two hyaluronan and proteoglycan link proteins (HAPLN-1 and HAPLN-2), indicating a role of hyaluronan metabolism in the disease.
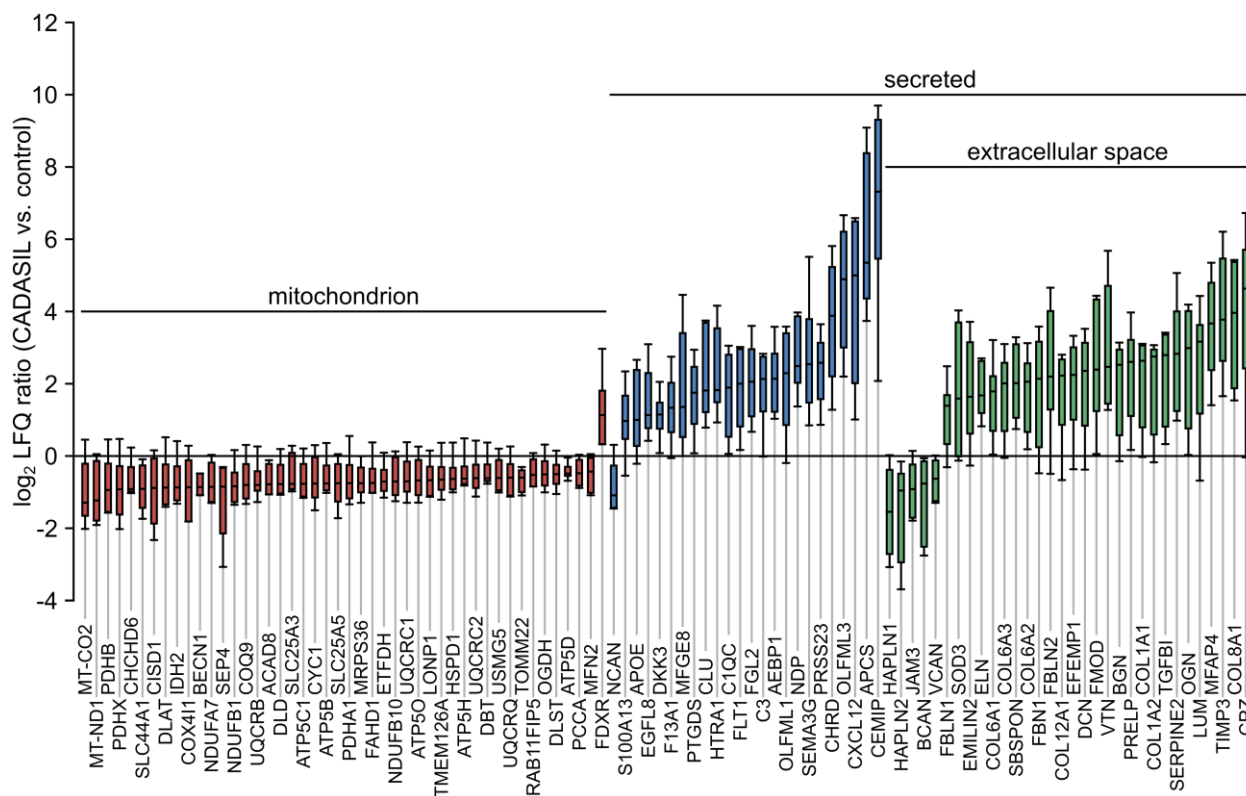
Figure 3.7: Secreted and extracellular space proteins are enriched, mitochondrial proteins are depleted in CADASIL brain vessels. Boxplots of the log$_2$ LFQ values (CADASIL vs. control) of significantly altered proteins. Corresponding gene names are displayed below.

Within the proteomic CADASIL profile (consisting of the 190 significantly changed proteins), multivariate statistical analysis revealed significant abundance changes for Notch3 and 16 additional accumulating proteins (Table 3.2).

Table 3.2: Proteins altered in CADASIL patients which passed multivariate statistical analysis

Gene names	Ratio	*p*-value
NOTCH3	144.51	3.5E-07
CEMIP	130.79	4.8E-04
APCS	65.92	5.8E-04
OLFML3	25.38	8.9E-04
CXCL12	21.16	6.7E-03
TIMP3	15.28	4.6E-04
CHRD	13.34	5.9E-03
COL8A1	13.05	1.2E-02
MFAP4	11.88	2.2E-03
VTN	7.80	3.7E-03
SERPINE2	6.88	4.1E-03
NDP	6.65	1.5E-04
GPNMB	5.72	1.2E-03
PRSS23	5.31	2.9E-03
HTRA1	4.89	1.6E-03
CLU	4.58	1.6E-03
PCMT1	2.24	4.9E-04

Parameters for multivariate statistical analysis: FDR = 0.05, S0 = 0.3
For a complete list of significantly altered proteins see Appendix, Table 5.1.

Serum amyloid P-component (APCS), tissue inhibitor of metalloproteinases 3 (TIMP3), vitronectin (VTN) and clusterin (CLU) have previously been reported to be enriched in CADASIL vessels and to colocalize with Notch3^{ECD} deposits (Nagatoshi et al. 2017; Monet-Lepretre et al. 2013; Arboleda-Velasquez et al. 2011). APCS is a plasma protein of the pentraxin family with a high affinity to amyloid protein deposits (Pepys 2018). TIMP3 and vitronectin are matrisome components involved in ECM homeostasis and were both proposed to be involved in specific aspects of CADASIL pathogenesis (Capone, Cognat, et al. 2016; Capone, Dabertrand, et al. 2016). Clusterin is considered as a molecular chaperone contributing to extracellular protein homeostasis (Wilson et al. 2017). Among the other proteins were signaling factors (stromal cell-derived factor 1 [CXCL12], chordin [CHRD], norrin [NDP]), proteases and protease inhibitors (serine protease 23 [PRSS23], high-temperature requirement protein A1 [HTRA1] and glia-derived nexin [SERPINE2]) as well as extracellular space proteins (cell migration-inducing and hyaluronan-binding protein [CEMIP], olfactomedin-like 3 [OLFML3], collagen VIII α1 chain and microfibril-associated glycoprotein 4 [MFAP4]).

CEMIP, the most strongly enriched protein after Notch3, and TIMP3 were selected for confirmation of their increased abundance by Western Blot analysis using vessel lysates of five

CADASIL patients and five control subjects. CEMIP staining revealed a band of ~153 kDa, corresponding to the predicted molecular weight of the full-length protein, and several additional bands of smaller mass, possibly representing proteolytical cleavage products (Figure 3.8, left panel). Immunoreactivity was also observed at the height of the stacking gel, likely representing high-molecular-weight material not efficiently entering the gel. Staining intensities over the full molecular weight range showed a considerable variation in both groups, but were consistently stronger in CADASIL than in control samples, and roughly corresponded to the LFQ values obtained by mass spectrometry (Figure 3.8, right panel). TIMP3 immunoreactivity was detected as a single band at the expected molecular weight of ~24 kDa in all CADASIL patients, but in none of the control subjects, and corresponded well with the LFQ values. CEMIP and TIMP3 labeling intensities in individual samples were roughly comparable, with CADASIL patient #2 showing the strongest signals for both proteins. However, Notch3 LFQ values were much more uniform and provided no clear explanation for the varying CEMIP and TIMP3 levels.
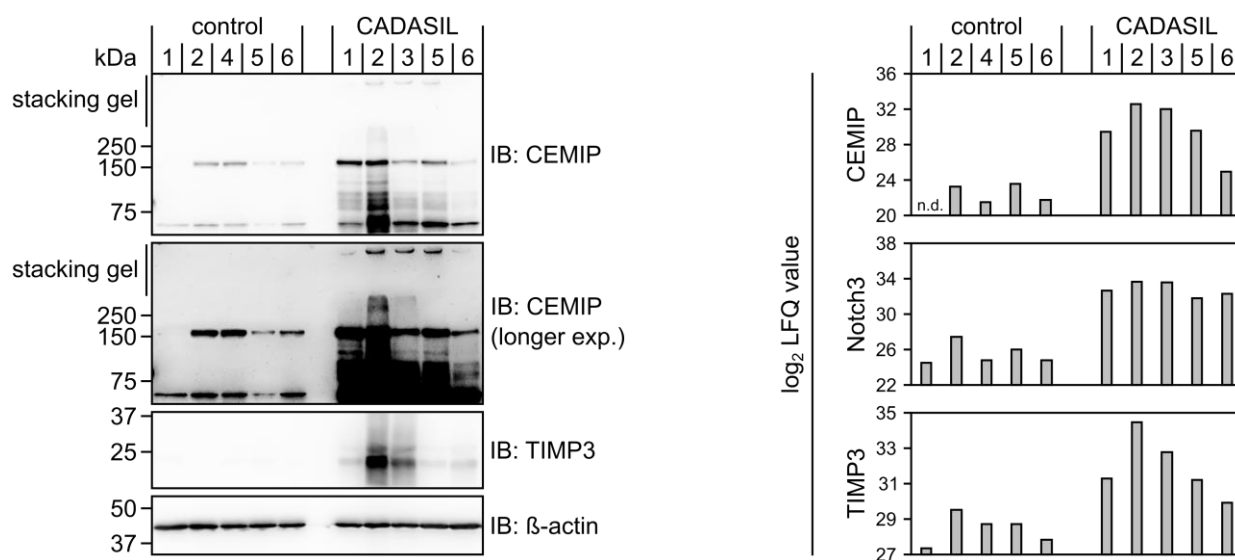
Figure 3.8: Accumulation of CEMIP and TIMP3 in CADASIL brain vessels. (left): CEMIP and TIMP3 expression levels were determined in brain vessel protein extracts from CADASIL patients and control subjects by Western Blotting. Expected molecular weights: CEMIP ~153 kDa, TIMP3 ~24 kDa. Stacking gel is shown to demonstrate CEMIP immunoreactivity of high-molecular-weight material not efficiently entering the gel. CEMIP bands of lower molecular weight possibly represent processed fragments. ß-actin was used as loading control (expected molecular weight: ~42 kDa). (**right**): Corresponding $\log_2$ LFQ values from the proteomic analysis. n.d.: not detected

3.4   HTRA1 accumulates in CADASIL brain vessels

The most intriguing protein emerging from the proteomic study was high temperature requirement protein A1 (HTRA1), as mutations in this conserved serine protease cause CARASIL (Hara et al. 2009), a hereditary small vessel disease with a phenotype very similar to CADASIL. HTRA1 showed a strong enrichment (4.9-fold) and one of the lowest p-values ($p = 1.6 \times 10^{-3}$) in the proteomic CADASIL profile (Figure 3.9, left panel). For verification, its abundance levels in brain vessel protein extracts were determined by a capillary-based Simple Western assay, allowing a precise quantification of immunosignals derived from submicrogram amounts of protein lysates (Figure 3.9, right panel). While HTRA1 levels were close to the detection limit in all but one control sample, they were clearly measurable in all CADASIL samples and shown to be significantly elevated.
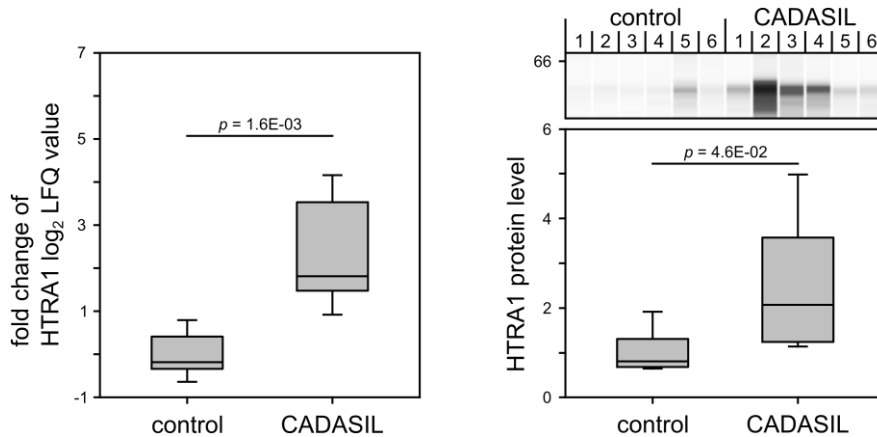
Figure 3.9: Enrichment of HTRA1 in CADASIL brain vessel extracts. (**left**): HTRA1 log₂ LFQ values of the proteomic analysis. (**right**): HTRA1 protein levels determined by Simple Western immunoassay including quantification.

To investigate whether HTRA1 accumulation also occurs in sporadic SVD, brain samples from three patients were analyzed, who had been diagnosed with non-familial vascular dementia and shown by neuropathological analysis to suffer from a severe arteriopathy of small and medium-sized cerebral vessels including fibrotic thickening of vessel walls. Simple Western immunoassay analysis revealed, in contrast to a CADASIL sample (4.6-fold), no increase (0.9 ± 0.5 -fold) relative to a control sample (Figure 3.10).
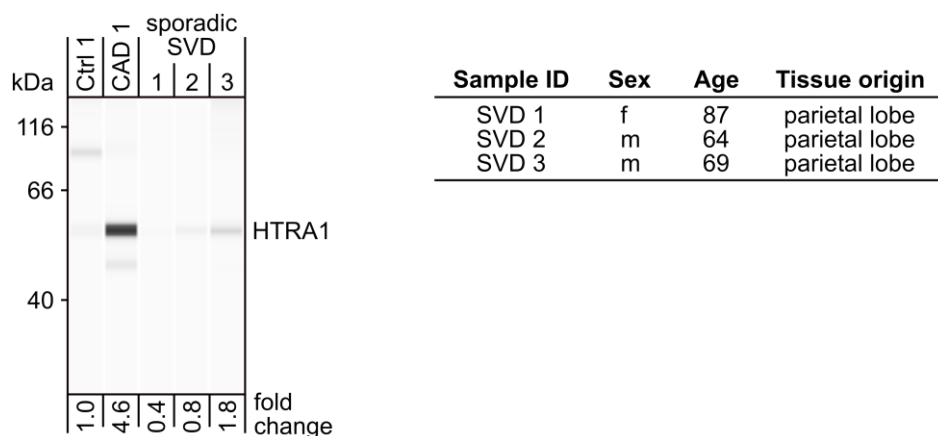
Figure 3.10: HTRA1 protein levels in brain vessel protein extracts from patients with sporadic cerebral small vessel disease (SVD). (**left**): Protein levels were determined by Simple Western immunoassay including quantification. (**right**): Main characteristics of brain autopsy samples from the three SVD patients. CADASIL patient and control subject features are listed in Table 3.1.

To further substantiate the link between HTRA1 and CADASIL, in situ staining of HTRA1 and Notch3^{ECD} was performed in isolated human brain vessels, using the newly established immunolabeling protocol (see 3.2). While in control vessels HTRA1 was hardly detectable, a strong signal was observed in vessels from patients (Figure 3.11). The significance of the signal difference was demonstrated by a quantification of the mean gray value, using 11 images from three different individuals in each group. In addition, immunoreactivity was observed as focal granules reminiscent of Notch3^{ECD} deposits.
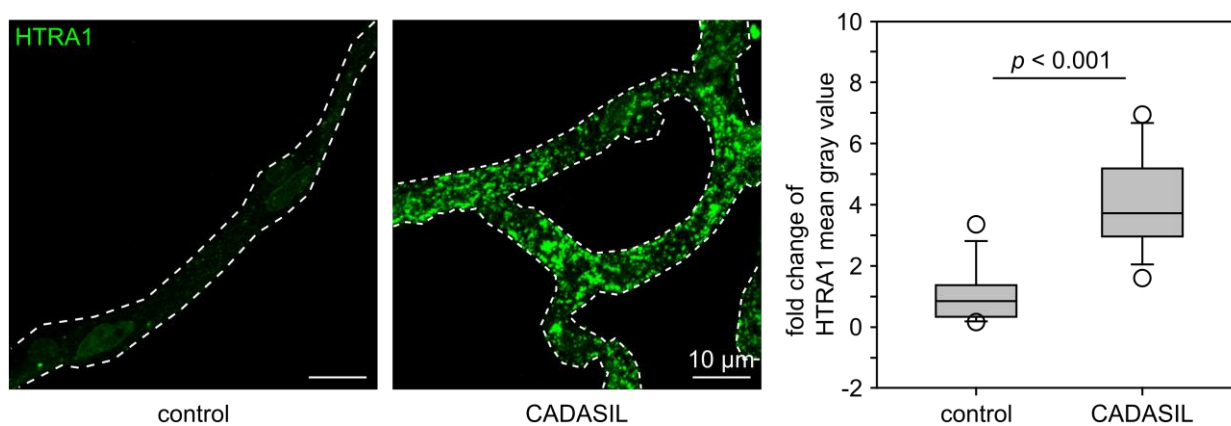
Figure 3.11: HTRA1 shows focal accumulation in CADASIL vessels. (**left**): Immunofluorescence staining of HTRA1 in an isolated brain capillary of a control subject and a CADASIL patient. Dashed line indicates vessel outline. (**right**): Quantification of the mean gray values of immunofluorescence images (n = 11) from vessels of three patients and three controls.

Next, costaining experiments of HTRA1 and Notch3^{ECD} were performed and analyzed by confocal microscopy. Importantly, immunofluorescence images revealed an almost perfect overlap

demonstrating a close spatial proximity (Figure 3.12) and strongly suggesting the recruitment and accumulation of HTRA1 within pathological Notch3^{ECD} deposits.
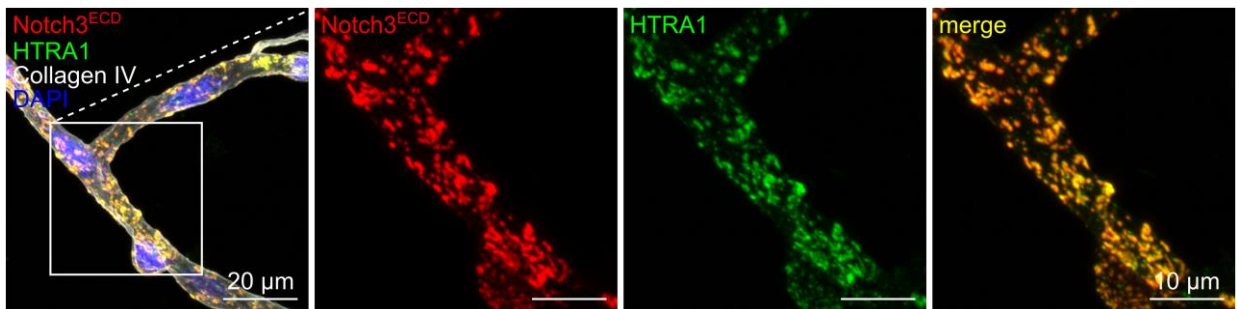
Figure 3.12: HTRA1 accumulates within Notch3^{ECD} deposits. Capillary from a CADASIL patient costained for Notch3^{ECD}, HTRA1, collagen IV and cell nuclei.

3.5 The CADASIL brain vessel proteome shows a HTRA1 loss-of-function profile

The sequestration of proteins into pathological aggregates is often accompanied by an impairment of their cellular function, primarily by the depletion from their normal cellular locations (Olzscha et al. 2011; Yang et al. 2016). In the case of proteases such as HTRA1 this might result in reduced processing and accumulation of their substrates. Indeed, several proteins previously reported as HTRA1 substrates (vitronectin, clusterin and elastin) (An et al. 2010; Vierkotten et al. 2011) were significantly enriched in the CADASIL brain vessel profile (Figure 3.13).
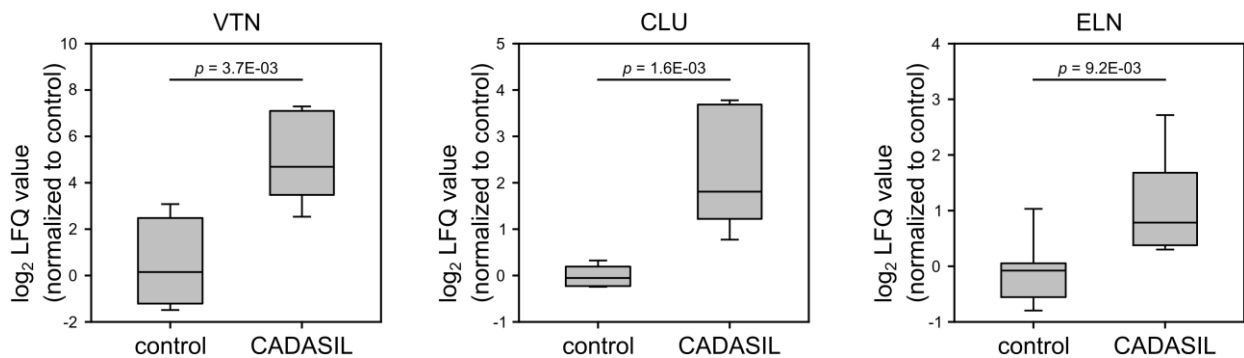
Figure 3.13: Enrichment of HTRA1 substrates in the CADASIL brain vessel proteome. Boxplots of log$_2$ LFQ values (normalized to control) for vitronectin (VTN), clusterin (CLU), and elastin (ELN) from the proteomic analysis of isolated brain vessel from CADASIL patients and control subjects.

To rule out genetic causes for a reduction in HTRA1 function (as in CARASIL), sequencing of all nine HTRA1 exons in four of the six CADASIL patients was performed, demonstrating the absence of any pathogenic mutations (data not shown). A transcriptional mechanism as cause for the increased HTRA1 abundance was investigated by quantifying its mRNA levels in full brain samples using real-time PCR, but no significant differences were observed (Figure 3.14).
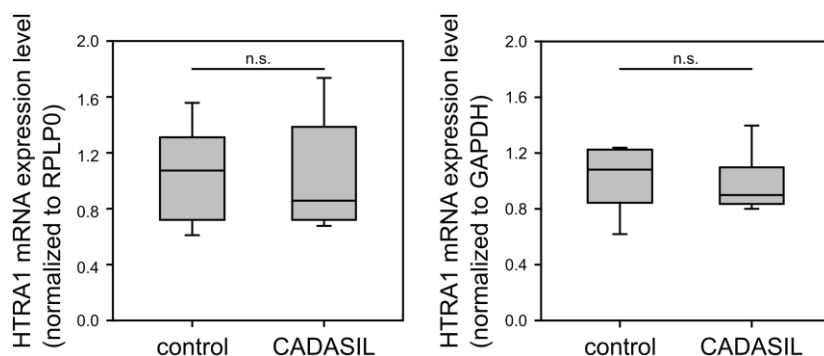
Figure 3.14: HTRA1 mRNA levels are not altered in CADASIL patients. Real-time PCR analysis was performed in CADASIL and control brain samples (n = 6). RPLP0 (**left**) and GAPDH (**right**) were used as housekeeping genes. Control values were set to 1.

3.5.1   The HTRA1 knockout mouse brain vessel proteome

To substantiate the assumption of a reduced HTRA1 activity in CADASIL, a better understanding of the full range of its substrates in brain vessels was required. This could be achieved by a comparison of the CADASIL proteome with a HTRA1 loss-of-function proteome. In the absence of post-mortem tissue from CARASIL patients suitable for vessel isolation, the brain vessel proteome of aged (20 months) HTRA1-deficient mice (Jones et al. 2011) was determined in comparison to wild-type controls (n = 5 for each group). HTRA1$^{-/-}$ mice have a normal life expectancy, show no clearly detectable vascular phenotype and are thus well suited to determine proteomic alterations in the absence of overt vessel pathology. The experimental procedures including the vessel isolation, the extraction of proteins as well as the proteomic analysis were performed as described earlier (see 3.3). Of the 5,285 proteins identified by two or more unique peptides, 3,884 were detected in at least three samples of each group and used for calculation of abundance ratios (HTRA1$^{-/-}$ vs. HTRA1$^{+/+}$) and for statistical analysis (Figure 3.15). HTRA1 peptides were exclusively detected in control animals, validating their absence in the knockout strain.
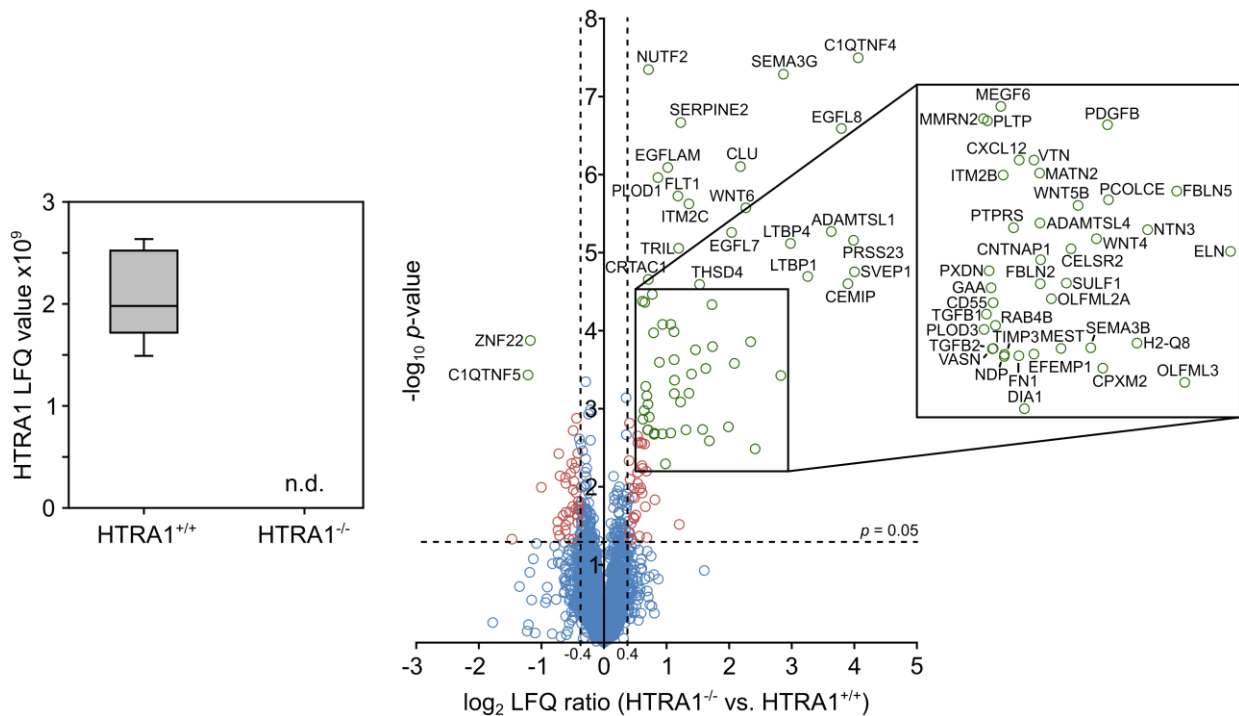
Figure 3.15: Proteomic analysis of isolated brain vessels from HTRA1$^{-/-}$ and HTRA1$^{+/+}$ mice. (left): HTRA1 log$_2$ LFQ values in wildtype and knockout animals. n.d.: not detected. (**right**): Volcano plot of log$_2$ LFQ ratios (HTRA1$^{-/-}$ vs. HTRA1$^{+/+}$) and -log$_{10}$ p-values of all quantified proteins. Red circles indicate proteins with a significant change in abundance ($p < 0.05$, log$_2$ ratio < -0.4/ > 0.4). Proteins labeled as green circles passed multivariate statistical analysis (FDR = 0.05, S0 = 0.1).

The distribution of all quantified proteins between major cellular compartments (according to the UniProt subcellular localization information) was very similar to the human study demonstrating comparable protein extraction efficiencies (Figure 3.16, top left panel, compare with Figure 3.6). 127 proteins were found to be significantly altered in their abundance ($p < 0.05$ and a log$_2$ abundance ratio of > 0.4 [~1.32-fold] or < -0.4 [~0.76-fold]) (for a complete list see Appendix, Table 5.2) and a strong and overall tendency towards protein enrichment was observed (Figure 3.15). In agreement with the expectation of substrate accumulation in the absence of HTRA1, the majority of significantly altered proteins (72%; 91/127) exhibited higher abundance. In addition, the extent of enrichment (up to 17-fold) was much higher than that of depletion (up to 2.8-fold).

Similar to the CADASIL proteome, a strong overrepresentation of secreted and extracellular space proteins among the significantly altered proteins was observed (Figure 3.16, top right panel). In these two categories, 92% (54/59) and 100% (27/27) of proteins were enriched (Figure 3.16, bottom panel), in agreement with HTRA1 being a primarily extracellular protease with a preference for extracellular matrix proteins.
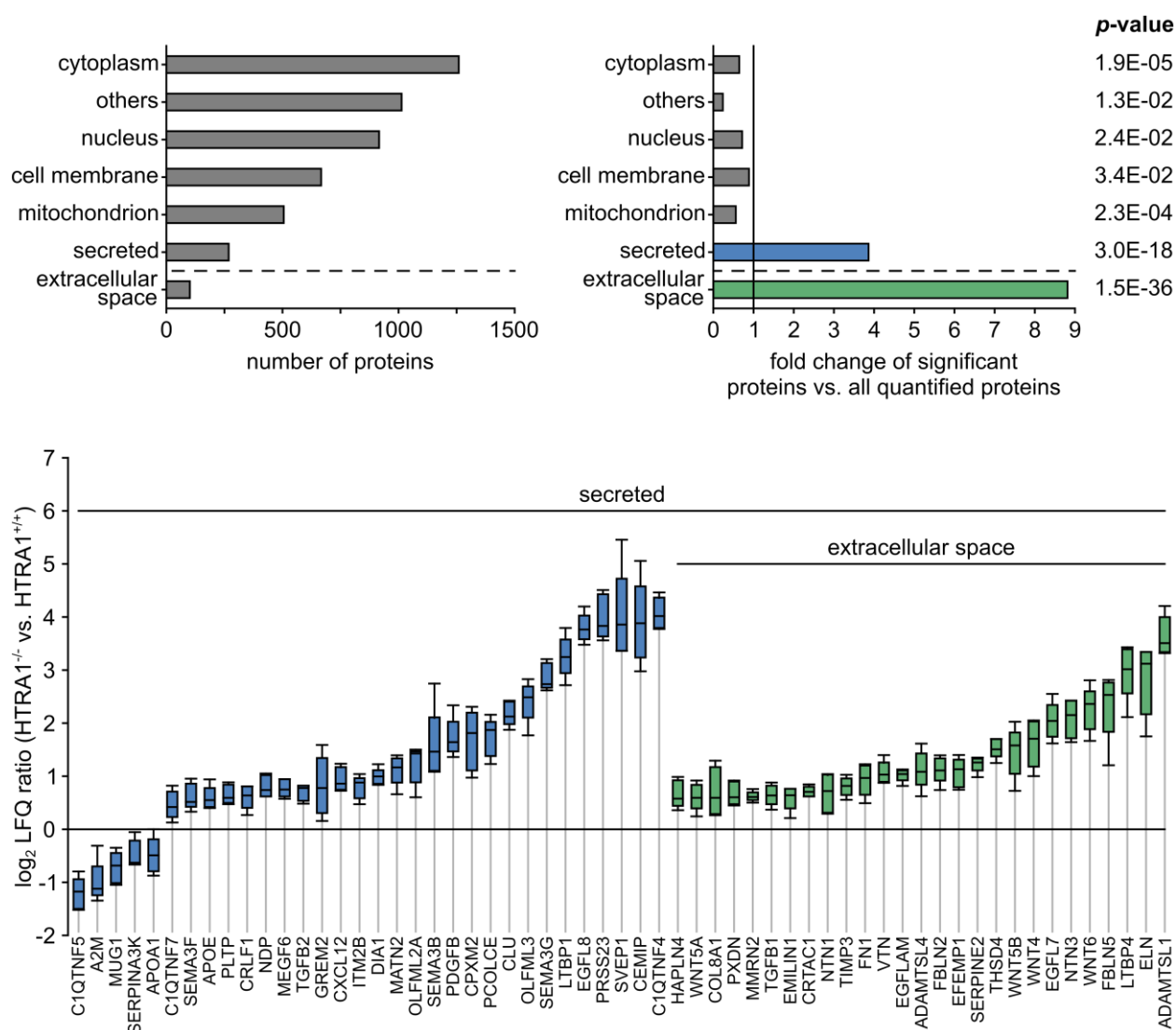
Figure 3.16: Secreted and extracellular space proteins are enriched in vessels from HTRA1$^{-/-}$ mice. (**top, left**): Classification of the 3,884 quantified proteins according to UniProt subcellular location information. (**top, right**): Over-/ underrepresentation of significantly altered proteins within each category. *p*-values were calculated by Fisher's exact test. The category of extracellular space proteins represents a subgroup of secreted proteins. (**bottom**): Boxplots of log$_2$ LFQ ratios (HTRA1$^{-/-}$ vs. HTRA1$^{+/+}$) of secreted and extracellular space proteins. Corresponding gene names are displayed below.

The HTRA1$^{-/-}$ profile included the well-described substrates vitronectin (VTN) (2.1-fold, $p = 8.4 \times 10^{-5}$), clusterin (CLU) (4.5-fold, $p = 7.9 \times 10^{-7}$) and elastin (ELN) (7.1-fold, $p = 3.8 \times 10^{-4}$). In addition, elevated levels of LTBP-1 (9.5-fold, $p = 2.0 \times 10^{-5}$), an important HTRA1 substrate our group has identified recently (Beaufort et al. 2014), and of its close homolog LTBP-4 (7.9-fold, $p = 7.7 \times 10^{-6}$) were found. In summary, the data supported the hypothesis that HTRA1 deficiency in mice causes a vascular accumulation of its substrates. The obtained proteomic profile was therefore used to more precisely determine the status of HTRA1 activity in the CADASIL brain vasculature.

3.5.2 Proteomic overlap of brain vessels from CADASIL and HTRA1 deficient mice

To determine the overlap of the two proteomic profiles only proteins were considered, for which abundance ratios and *p*-values had been calculated in both analyses. A comparison between the 3339 proteins of the CADASIL proteome and the 3884 proteins of the mouse HTRA1$^{-/-}$ proteome yielded a shared set of 2509 proteins. Among the proteins with significantly higher abundance, 78 from the CADASIL profile and 50 from the HTRA1$^{-/-}$ profile were eligible (Figure 3.17, top left panel). A total number of 18 proteins was present in both profiles representing a highly significant overlap ($p = 2.2 \times 10^{-16}$). In contrast, only one protein (of 76 respectively 20 eligible proteins from the two profiles) was found to have lower abundance in both datasets, representing a non-significant overlap. Moreover, overlapping proteins were among the proteins with the highest abundance changes in each individual dataset, including seven out of the ten most strongly enriched proteins (Figure 3.17, bottom panel).
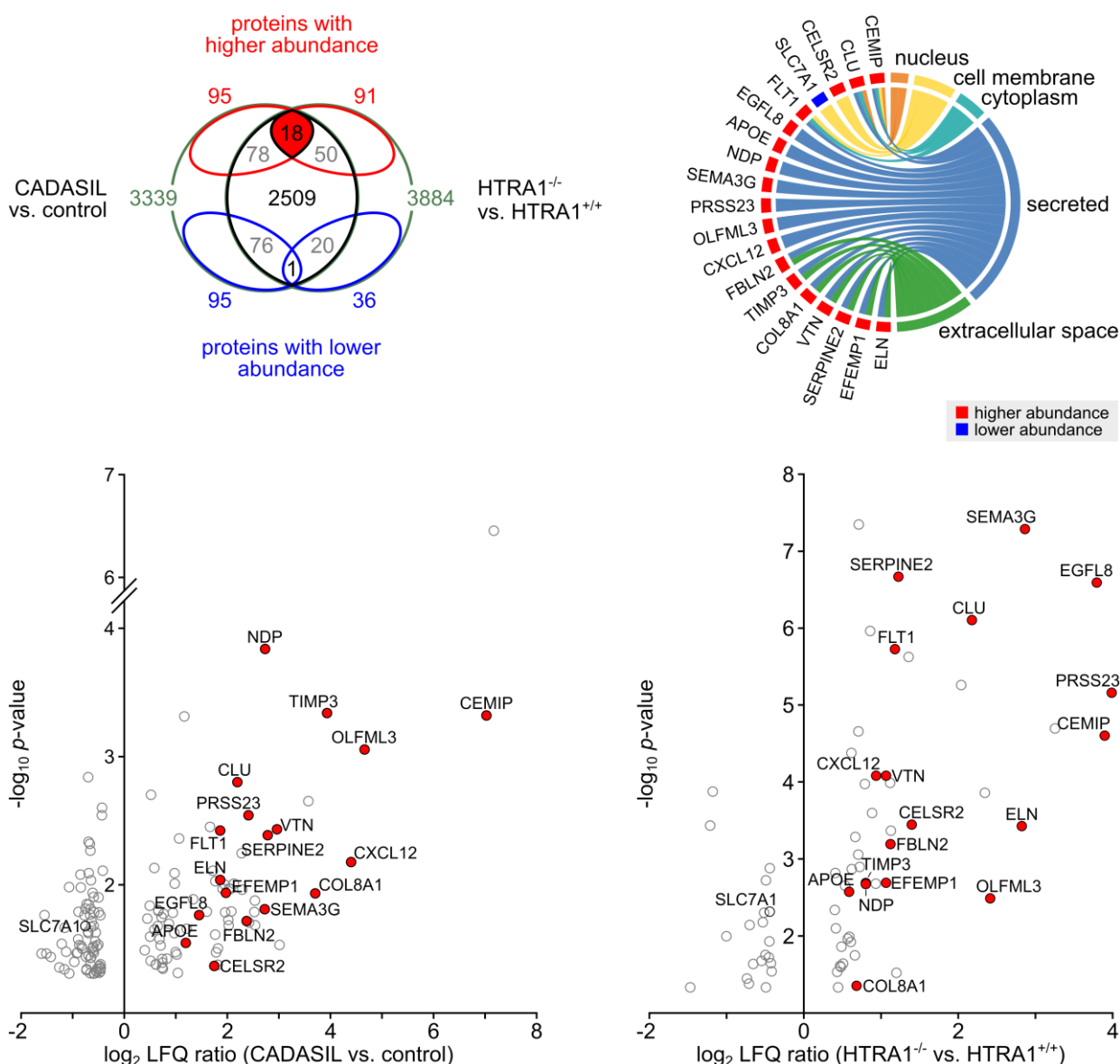
Figure 3.17: Overlap between the CADASIL and the HTRA1$^{-/-}$ proteomic profiles. (**top, left**): Venn diagram illustrating the overlap between all quantified proteins (green outlines) and proteins with significantly higher and lower abundance (red/blue outlines) of both proteomic analyses. Within the shared set of 2509 quantified proteins (black outline) a comparison of the 78 (CADASIL vs. control) and 50 (HTRA1$^{-/-}$ vs. HTRA1$^{+/+}$) enriched proteins revealed a significant ($p = 2.2 \times 10^{-16}$) overlap of 18 proteins (red filling). No significant overlap was obtained between the 76 and 20 depleted proteins. (**right**): Circos diagram illustrating subcellular locations (UniProt) and abundance changes of shared proteins. (**bottom**): Volcano plots of log$_2$ LFQ ratios and $-$log$_{10}$ p-values of the 154 significantly altered proteins in CADASIL patients vs. control subjects (**left**) and the 70 significantly altered proteins in HTRA1$^{-/-}$ vs. HTRA1$^{+/+}$ mice (**right**). Red filling indicates overlapping proteins. Y-axis starts at 1.

An analysis of the subcellular localization of the overlapping proteins revealed a strong preference for secreted and extracellular space proteins (Figure 3.17, top right panel), providing further support for their role as HTRA1 substrates.

Collectively, these results suggested that a substantial portion of proteins accumulating in CADASIL brain vessels represent HTRA1 substrates, an observation compatible with a reduction in its proteolytic activity.

3.5.3   Identification of novel HTRA1 substrates

Except for vitronectin, clusterin and elastin, none of the overlapping proteins was known to be processed by HTRA1 (An et al. 2010; Vierkotten et al. 2011). To experimentally validate HTRA1-mediated proteolytic cleavage of some of them, a previously established *in vitro* assay was used (Beaufort et al. 2014; Verdura et al. 2015). It is based on the coincubation of conditioned supernatants from transiently transfected human embryonic kidney (HEK) 293 cells. From the list of proteins significantly changed in CADASIL patients and HTRA1$^{-/-}$ mice, CEMIP, semaphorin-3G (SEMA3G), vitronectin (VTN), OLFML3 and TIMP3 were selected for analysis on the basis of their abundance ratio in the CADASIL profile and their secretion behavior in the assay. Chordin (CHRD) was additionally included due to its high accumulation in the CADASIL profile (13.3-fold, $p = 5.9 \times 10^{-3}$) and a strong accumulation tendency in the HTRA1$^{-/-}$ profile (detected in all HTRA1$^{-/-}$ animals, but only in one out of five HTRA1$^{+/+}$ animals preventing the calculation of an abundance ratio). Since HTRA1$^{-/-}$ mice did not show Notch3 accumulation, the Notch3$^{EGF\ 1-15}$ fragment, the longest Notch3^{ECD} fragment efficiently secreted from cultured cells, was used as a negative control. The C-terminally truncated LTBP-1ΔC variant was selected as a positive control, as Beaufort and coworkers have recently shown its efficient processing in this assay (Beaufort et al. 2014).

All constructs were cloned as fusion proteins with a C-terminal Myc tag and transiently transfected into HEK293 cells. To ensure roughly equal concentrations of potential substrates, the α-Myc Western Blotting signal intensities of individual conditioned supernatants were used for adjustment by volume reduction via Amicon Ultra Centrifugal Filters with a 3-kDa cut-off. Figure 3.18 displays expression levels of adjusted conditioned supernatants used for HTRA1 coincubation experiments.
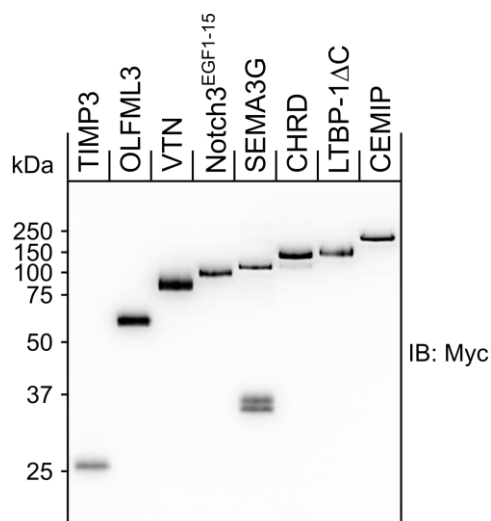
Figure 3.18: Adjusted protein levels of potential HTRA1 substrates. α-Myc Western Blot of conditioned supernatants derived from transiently transfected HEK293 cells expressing Myc-tagged TIMP3, OLFML3, VTN, Notch3$^{EGF\ 1\text{-}15}$, SEMA3G, CHRD, LTBP-1ΔC and CEMIP.

Potential substrates as well as LTBP-1ΔC and Notch3$^{EGF\ 1-15}$ were incubated with HTRA1 or the active site mutant HTRA1^{S328A} (serving as a negative control). While the levels of Notch3$^{EGF\ 1-15}$ did not change detectably after 24 h incubation, LTBP-1ΔC was almost completely converted from its full-length form into a truncated fragment (Figure 3.19). Importantly, CEMIP, chordin, SEMA3G, vitronectin and OLFML3 showed a clear degradation in the presence of HTRA1, only TIMP3 was less efficiently processed. No cleavage was observed with the active-site mutant HTRA1^{S328A}.
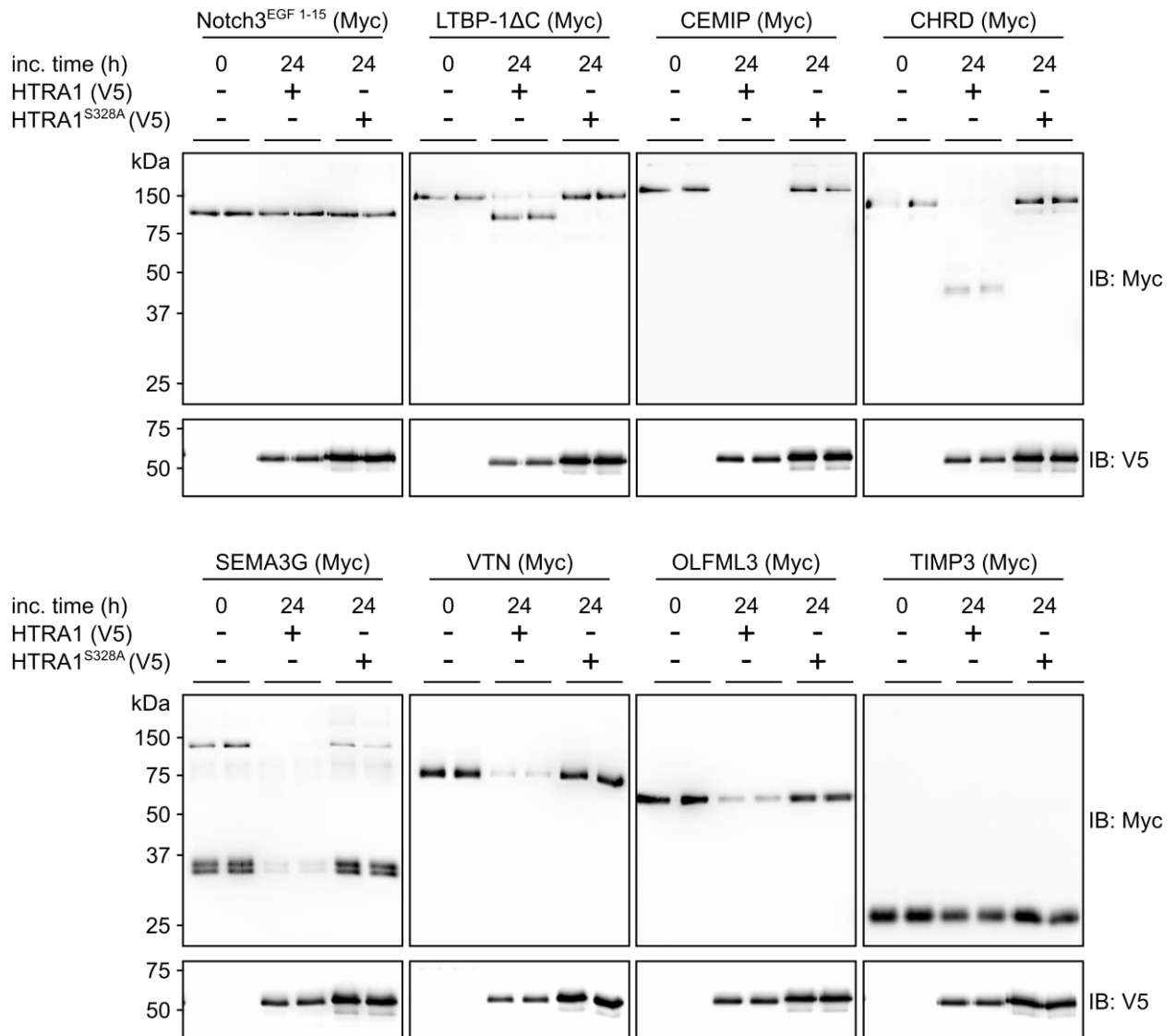
Figure 3.19: Validation of novel HTRA1 substrates by in vitro cleavage. Immunoblots of conditioned media from HEK293 cells expressing Myc-tagged Notch3[EGF 1–15], LTBP-1ΔC, CEMIP, CHRD, SEMA3G, VTN, OLFML3 and TIMP3 were coincubated with supernatants containing V5-tagged HTRA1 or the active site mutant HTRA1[S328A]. SEMA3G bands of lower molecular weight likely represent fragments generated by other proteases.

HTRA1-mediated degradation of CEMIP was highly efficient and therefore further analyzed in time-course coincubations for up to 24 h revealing a time-dependent processing and almost complete degradation already after 9 h (Figure 3.20, top panel). To exclude CEMIP cleavage by another protease potentially present in cell supernatants, purified full-length HTRA1 was used and degradation with comparable efficiency observed (Figure 3.20, right bottom panel). Furthermore, in the presence of a HTRA1-specifc inhibitor (Grau et al. 2005), CEMIP degradation by conditioned supernatants or purified HTRA1 was completely prevented (Figure 3.20, left and right bottom panels).
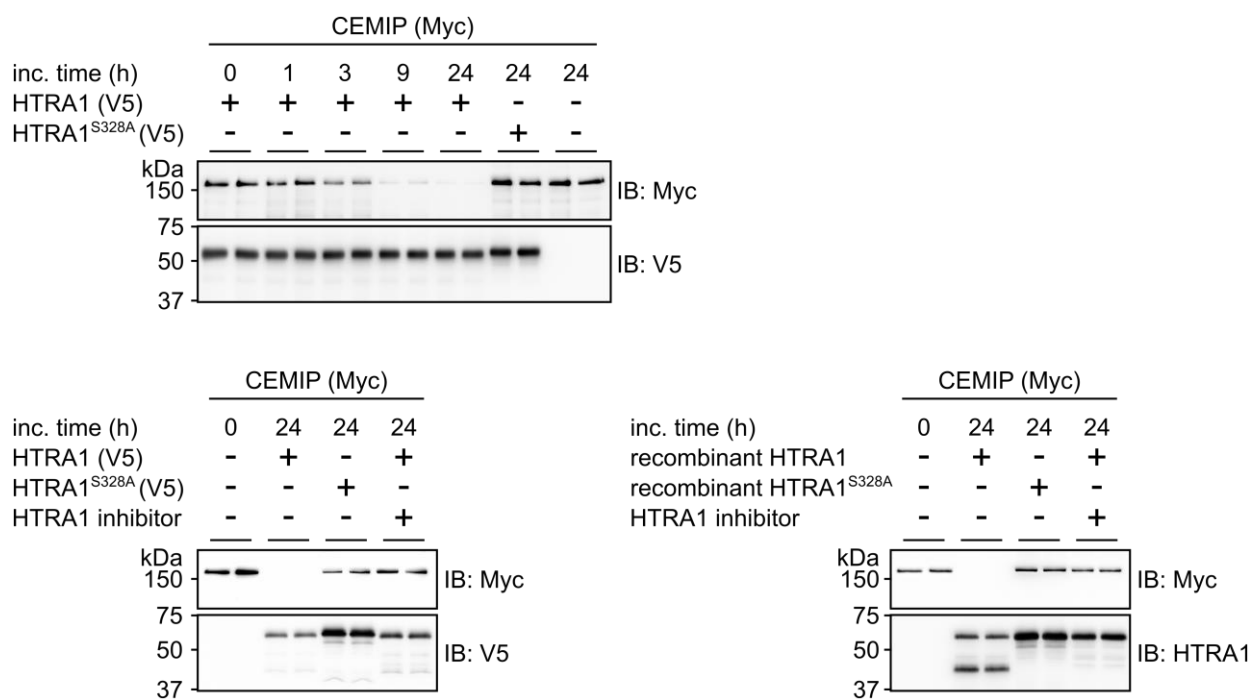
Figure 3.20: CEMIP is efficiently processed by HTRA1. (**top**): Time dependent coincubation of conditioned supernatants containing Myc-tagged CEMIP and V5-tagged HTRA1. (**bottom**): CEMIP processing by HTRA1-containing media (**left**) or by recombinant HTRA1 (100 nM) (**right**) in the presence or absence of a HTRA1-specifc inhibitor (5 µM NVP-LBG976, Novartis) (Grau et al. 2005).

Thus, by selecting CEMIP, SEMA3G, OLFML3 and chordin from the proteomic profile overlap, four novel HTRA1 substrates with a putative role in CADASIL and CARASIL pathogenesis were identified. Collectively, the comparison of the two proteomic profiles provided strong evidence for an impairment of HTRA1 catalytic activity in CADASIL, most likely via recruitment of HTRA1 to pathological Notch3^{ECD} aggregates.

3.6 HTRA1^{S270Lfs*69} causes a loss-of-function

Genetic HTRA1 mutations causing dominant and recessive forms of hereditary SVD with phenotypic similarity to CADASIL primarily represent missense variants (Nozaki et al. 2014). While it is widely accepted that they result in a reduction of HTRA1 catalytic activity, null mutations resulting in a complete loss of HTRA1 function are rather rare and barely studied in humans on a molecular level. During the course of this thesis, a novel homozygous HTRA1 mutation was identified in three patients from a consanguineous pedigree in Isfahan province (Iran) using homozygosity mapping and whole-exome sequencing (Ziaei et al. 2019). In addition to typical clinical CARASIL manifestations, these patients presented inflammatory-like features and recurrent rhinitis. They were found to carry an insertion of a guanine at position 805 in the

HTRA1 coding region (c.805_806insG), predicted to result in a 69-amino acid frameshift followed by a premature stop codon (S270Lfs*69). The encoded protein was expected to represent a truncation variant lacking a portion of the catalytic domain including the active site serine residue (Ser-328). To verify whether protein is produced from the mutant mRNA and to investigate the expression and secretion behavior of the truncation mutant, plasmids encoding wildtype and mutated HTRA1 were transfected into HEK293 cells and conditioned media and cell lysates were analyzed by Western Blotting (Figure 3.21).The truncated protein was present at the predicted molecular weight of ~37 kDa in cell lysates, albeit at strongly reduced levels compared with wildtype HTRA1. Interestingly, in conditioned supernatants the mutant protein could not be detected, whereas wildtype HTRA1 was clearly identified. This suggested rapid intracellular degradation or a defect in secretion of the S270Lfs*69 mutant, a phenomenon observed in the presence or absence of a C-terminal V5/His tag, excluding the possibility of differences in antibody detection.
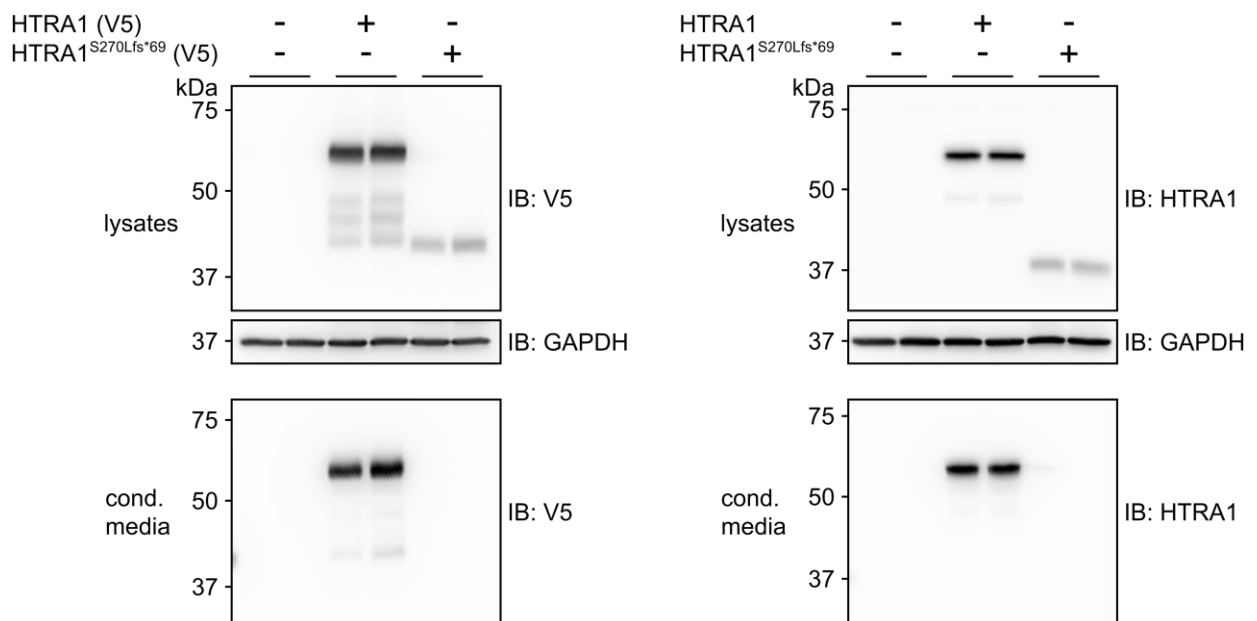
Figure 3.21: HTRA1^{S270Lfs*69} shows low expression and inefficient secretion. Immunoblots of cell lysates and conditioned media from HEK293 cells transiently transfected with plasmids encoding wildtype HTRA1 or the truncated variant HTRA1^{S270Lfs*69} with V5/His tag (**left**), or without epitope tag (**right**). For the detection of untagged HTRA1, a polyclonal antibody against amino acids 120–179 of HTRA1 was used (Sigma-Aldrich). Equal volumes of conditioned media were analyzed. For the cell lysates, GAPDH was used as a loading control.

Thus, the S270Lfs*69 variant, in addition to lacking the catalytic active site of HTRA1, is instable or secretion deficient and can clearly be considered as HTRA1 loss-of-function mutation.

3.7 HTRA1 in cerebral amyloid angiopathy (CAA)

CAA is a common, mostly sporadic, age-related cerebral SVD and a major cause of intracerebral hemorrhage. Similar to CADASIL, it is caused by protein misfolding as well as aggregation, and is characterized by protein deposits mainly consisting of amyloid-beta (Aβ) peptides in brain vessel walls (Charidimou et al. 2017).

To investigate, whether HTRA1 might also be involved in CAA pathology, pilot experiments were performed on three samples of a larger collection of brain autopsy material from CAA patients (Table 3.3), which had been selected on the basis of neuropathological findings compatible with CAA (e.g. vascular Aβ and/ or Congo Red reactivity). Brain vessels were isolated from these samples as described earlier (Figure 3.1) and HTRA1 protein levels in vessel extracts were determined by a quantitative Simple Western immunoassay in comparison to a CADASIL and a control sample (Figure 3.22). HTRA1 signal intensity differed considerably between the CAA samples, however, two of them showed enrichment (5.7-fold and 82.9-fold) similar to or even exceeding the levels of the CADASIL sample (4.6-fold).
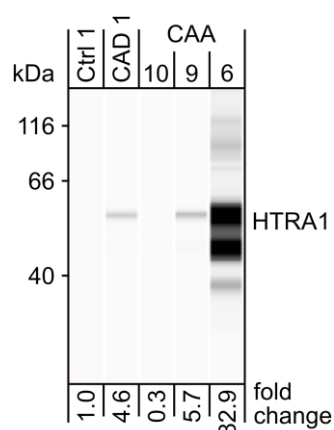
Figure 3.22: HTRA1 enrichment in CAA brain vessel extracts. HTRA1 protein levels in brain vessel protein lysates from three CAA patients, one CADASIL patient and one control subject determined by the Simple Western immunoassay. Quantification relative to the control sample is shown below.

Next, immunofluorescence costaining of HTRA1 and Aβ was performed using CAA brain sections from patient #9. In brain vessels with a clearly detectable Aβ signal, an extensive colocalization between Aβ and HTRA1 was observed (Figure 3.23), indicating the presence of HTRA1 in or very

close to pathological Aβ deposits. This finding extended previously reported data (Grau et al. 2005; Hondius et al. 2018) and strongly suggested a role of HTRA1 in CAA.
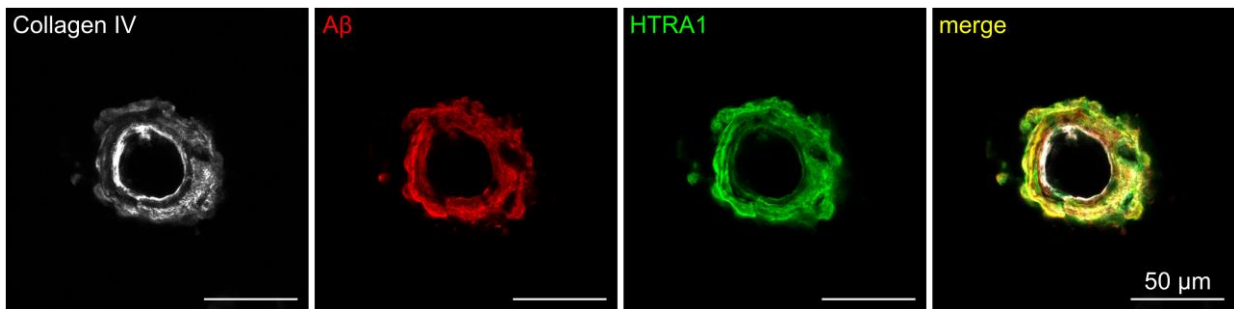
Figure 3.23: HTRA1 colocalizes within vascular Aβ deposits. An arteriole from CAA patient #9 costained for collagen IV, Aβ and HTRA1.

3.8   The CAA brain vessel proteome shows a HTRA1 loss-of-function profile

Recruitment of HTRA1 to Aβ deposits in CAA might, similar as in CADASIL, result in an impairment of its catalytic function, possibly resulting in an accumulation of its substrates. Several proteomic studies aimed to identify protein abundance alterations in the cerebral vasculature of CAA patients had previously been reported (Manousopoulou et al. 2017; Endo et al. 2019; Inoue et al. 2017; Hondius et al. 2018). However, all of them differed considerably from the mass spectrometry approach in this study with respect to the tissue isolation procedure, peptide mass detection sensitivity and quantification methodology. Moreover, only a limited number of altered proteins had emerged from these studies, so that no proteomic dataset was available which allowed a meaningful and comprehensive comparison with the CADASIL or HTRA1 loss-of-function profiles. Therefore, a new attempt was made to determine a quantitative and high-quality CAA brain vessel proteome using experimental settings fully comparable with the MS analyses described earlier (3.3 and 3.5.1).

3.8.1 The CAA brain vessel proteome

The cohort comprised 15 CAA patients (mean age 74.9 ± 9.4 years) and nine age-matched control subjects (mean age 69.8 ± 10.9 years) (Table 3.3).

Table 3.3: Main characteristics of brain autopsy samples from CAA patients and control subjects

Sample ID	Sex	Age	APOE genotype	Tissue origin
CAA 1	male	70	ε3 / ε3	occipital lobe
CAA 2	male	78	ε3 / ε3	occipital lobe
CAA 3	female	93	ε3 / ε4	occipital lobe
CAA 4	male	63	ε3 / ε4	occipital lobe
CAA 5	male	73	ε3 / ε4	occipital lobe
CAA 6	female	78	ε4 / ε4	parietal lobe
CAA 7	male	68	ε3 / ε4	occipital lobe
CAA 8	male	70	ε3 / ε3	occipital lobe
CAA 9	male	61	ε3 / ε3	parietal lobe
CAA 10	female	88	ε2 / ε3	parietal lobe
CAA 11	male	75	ε4 / ε4	occipital lobe
CAA 12	male	68	ε4 / ε4	parietal lobe
CAA 13	male	71	ε2 / ε3	parietal lobe
CAA 14	male	77	ε3 / ε3	occipital lobe
CAA 15	female	90	ε3 / ε4	occipital lobe
Control 1	male	51	ε3 / ε4	frontal lobe
Control 2	male	67	ε3 / ε3	occipital lobe
Control 3	male	59	ε3 / ε4	occipital lobe
Control 4	male	75	ε3 / ε4	occipital lobe
Control 5	female	75	ε3 / ε3	occipital lobe
Control 6	female	76	ε3 / ε3	occipital lobe
Control 7	female	63	ε3 / ε3	occipital lobe
Control 8	male	87	ε2 / ε3	occipital lobe
Control 9	female	64	ε3 / ε3	occipital lobe

N/A: Information not available

Since Aβ pathology can differ substantially between CAA patients and even between different brain regions of the same patient, the Aβ load of the available samples was determined by immunoblotting of brain vessel extracts prior to proteomic analysis. As observed in the pilot experiment, strong individual differences were detected, prompting the classification in three groups (Figure 3.24). Five samples exhibiting high Aβ levels (CAA_{high}), whereas in seven samples a considerably lower immunoreactivity was observed (CAA_{med}). In three samples, Aβ levels were below the detection limit and indistinguishable from control subjects (CAA_{low}).
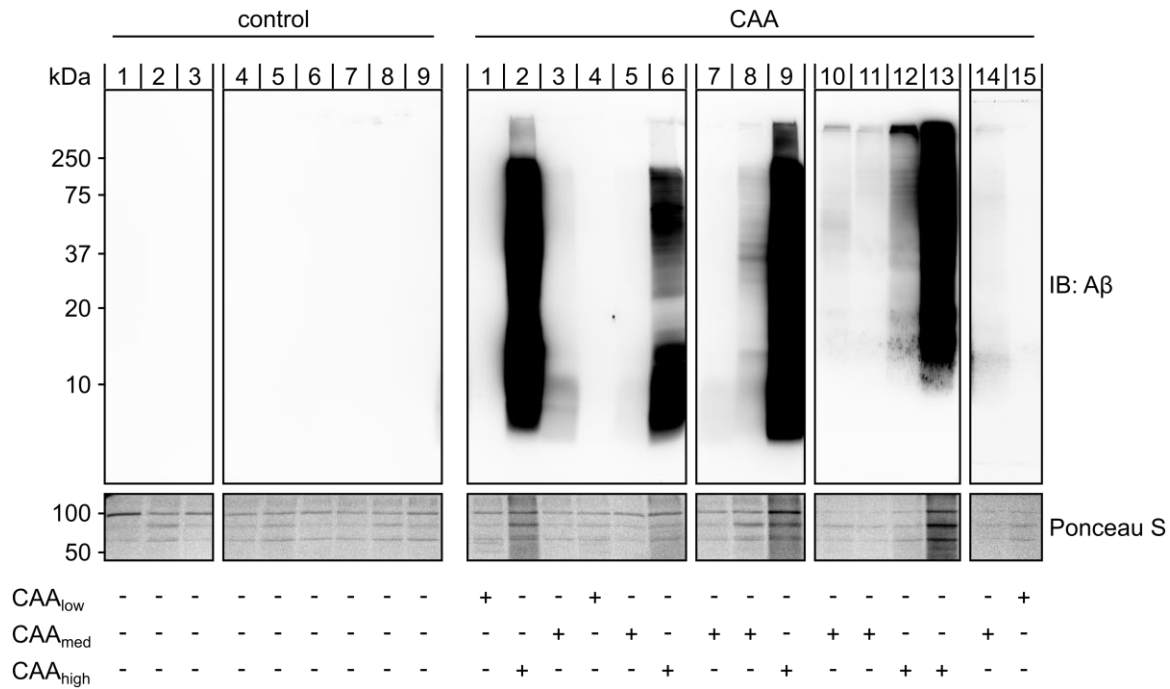
Figure 3.24: Vascular Aβ load is variable in the available CAA autopsy material. Aβ levels in brain vessel extracts from individual CAA and control samples were determined by Western Blotting and used to classify them in CAA_{high}, CAA_{med} and CAA_{low}. Ponceau S staining was used as a loading control.

Proteome analysis was performed for all CAA subgroups (Figure 3.25) and individual protein abundance changes were normalized to the control group. The thresholds used for statistical analysis ($p < 0.05$, $\log_2$ ratio $< -0.4/ > 0.4$) were identical to CADASIL and HTRA1$^{-/-}$ studies. The total number of proteins included in the statistical analyses (CAA_{low}: 3111, CAA_{med}: 3739, CAA_{high}: 3312) diverged from group to group due to the differences in group size (CAA_{low}: 3, CAA_{med}: 7, CAA_{high}: 5). In the CAA_{low} group only 3.9% (122) of the proteins were significantly altered and none of them passed multivariate statistical analysis. In the CAA_{med} group, 9.6% (360) of the proteins showed significant abundance differences, but only two remained significant after multivariate statistical analysis (Table 5.3 and Table 5.4). In the CAA_{high} group, 9.7% (322) of the proteins were significantly altered and 33 of them passed multivariate statistical analysis (Table 5.5). In addition, the overall extent of enrichment was much higher in the CAA_{high} group (up to 170-fold) compared to CAA_{med} and CAA_{low} patients (up to 10-fold and 16-fold) (Figure 3.25).
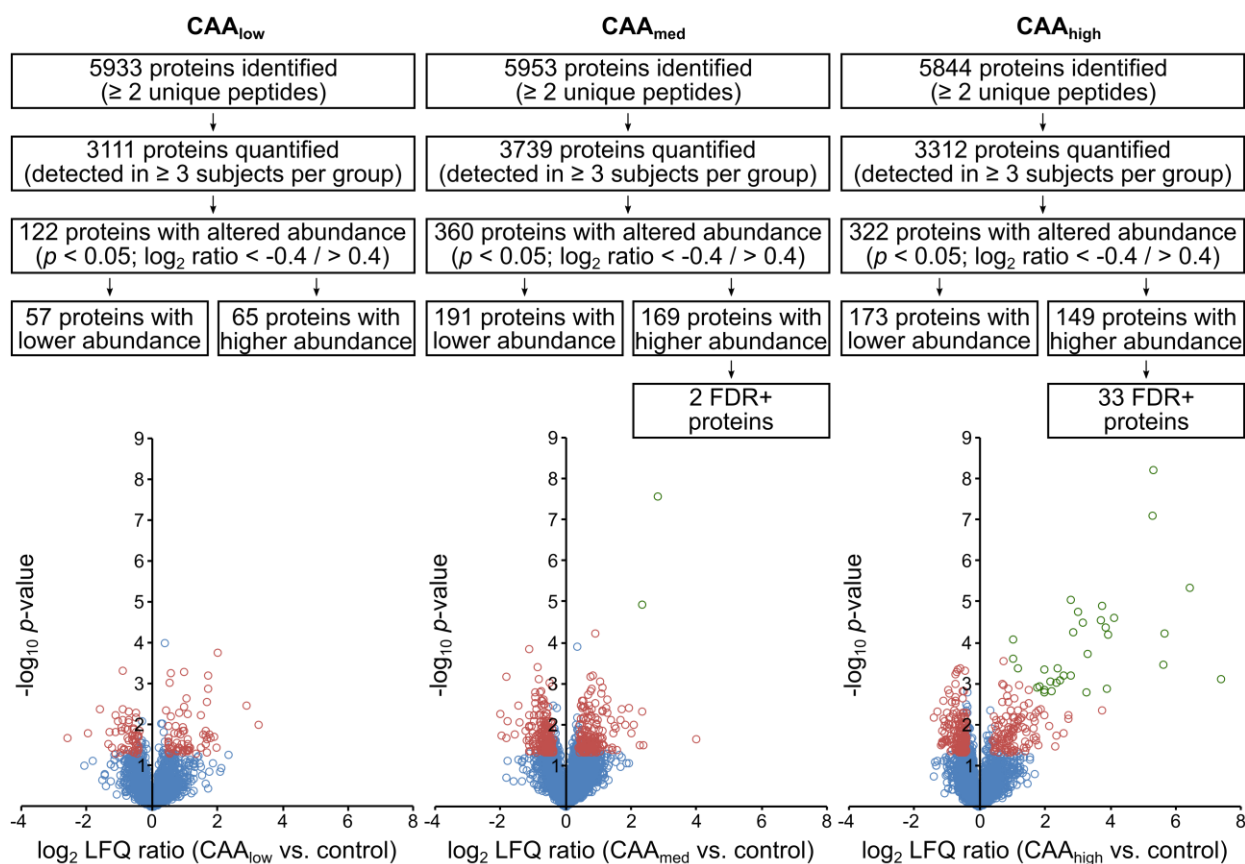
Figure 3.25: Proteomic analysis of isolated brain vessels from CAA patients with low, medium and high Aβ load. (**top**): Summary of LC-MS/MS and label-free quantification (LFQ) results from CAA$_{low}$ patients vs. control subjects (**left**), CAA$_{med}$ patients vs. control subjects (**middle**) and CAA$_{high}$ patients vs. control subjects (**right**). (**bottom**): Volcano plots of log$_2$ LFQ ratios and -log$_{10}$ p-values of all quantified proteins. Red circles indicate proteins with a significant change in abundance ($p < 0.05$, log$_2$ ratio $< -0.4/ > 0.4$). Proteins labeled as green circles passed multivariate statistical analysis (FDR = 0.05, S0 = 0.1).

3.8.2   Overlap with CADASIL and HTRA1$^{-/-}$ profiles

A comparison of the CADASIL profile with the three individual CAA profiles revealed increasing degrees of overlap from CAA$_{low}$ and CAA$_{med}$ to CAA$_{high}$. While only five proteins were shared with the CAA$_{low}$ group, 20 and 42 common proteins were found with the CAA$_{med}$ and CAA$_{high}$ groups, respectively (Figure 3.26). This trend was further supported by plotting the LFQ values of the overlapping proteins, visualizing the directionality of the abundance changes; while in the CAA$_{low}$ and the CAA$_{med}$ group only four and ten proteins respectively showed the same directionality, this was the case for all 42 proteins in the CAA$_{high}$ group (Figure 3.26). These results suggested an increasing proteomic similarity between CAA and CADASIL with increasing Aβ load. Moreover, HTRA1, not altered in the CAA$_{low}$ group, was 2.2-fold enriched in the CAA$_{med}$ group ($p = 4.8 \times 10^{-3}$) and 17.4-fold enriched in the CAA$_{high}$ group ($p = 2.5 \times 10^{-5}$) (Figure 3.26), supporting the hypothesis of an Aβ-dependent HTRA1 accumulation.
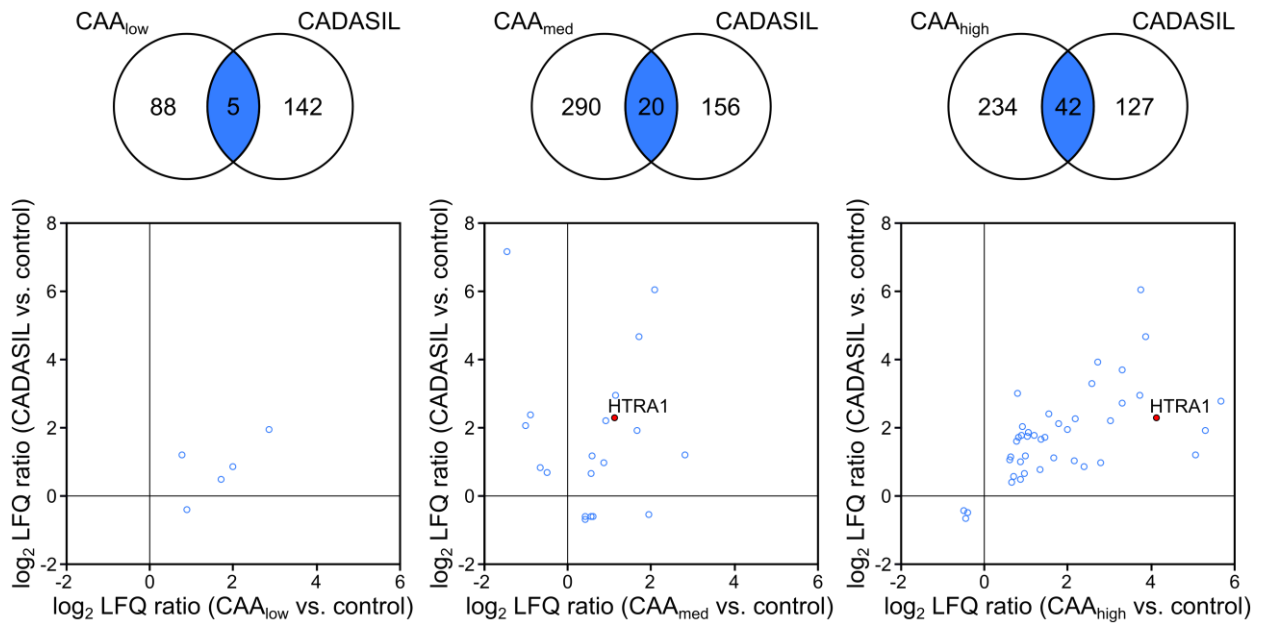
Figure 3.26: Increasing overlap between the CAAlow, CAAmed, CAAhigh and CADASIL proteomic profiles. (**top**): Venn diagrams illustrating the overlap between the CAA and CADASIL profiles for proteins with $p < 0.05$ and a $\log_2$ ratio $< -0.4/ > 0.4$. (**bottom**): correlation of $\log_2$ ratios for each overlapping protein. For each comparison, only proteins identified in at least three samples of the respective groups were considered.

The enrichment of many HTRA1 substrates in the CADASIL profile (Figure 3.17) provided strong evidence for a loss of HTRA1 proteolytic activity in disease pathogenesis. To investigate whether this phenomenon can also be observed in CAA, the CAAlow, CAAmed and CAAhigh proteomes were compared with the HTRA1 knockout mouse (HTRA1$^{-/-}$) proteome. While only six overlapping proteins were found in CAAlow, 10 and 17 overlapping proteins were identified in CAAmed and CAAhigh, respectively (Figure 3.27). Strikingly, when focusing on proteins with higher abundance, only one protein was identified in CAAlow, four proteins in CAAmed, but 15 proteins in CAAhigh. Moreover, all proteins with higher abundance in CAAlow (Apolipoprotein E, [APOE]) or in CAAmed (APOE, CLU, VTN and OLFML3) were also enriched in CAAhigh (Figure 3.27). Thus, along with HTRA1 accumulation, the degree of overlap with the CADASIL and HTRA1$^{-/-}$ profiles appeared to correlate with CAA amyloid severity, suggesting an impairment of HTRA1 proteolytic activity in CAA.
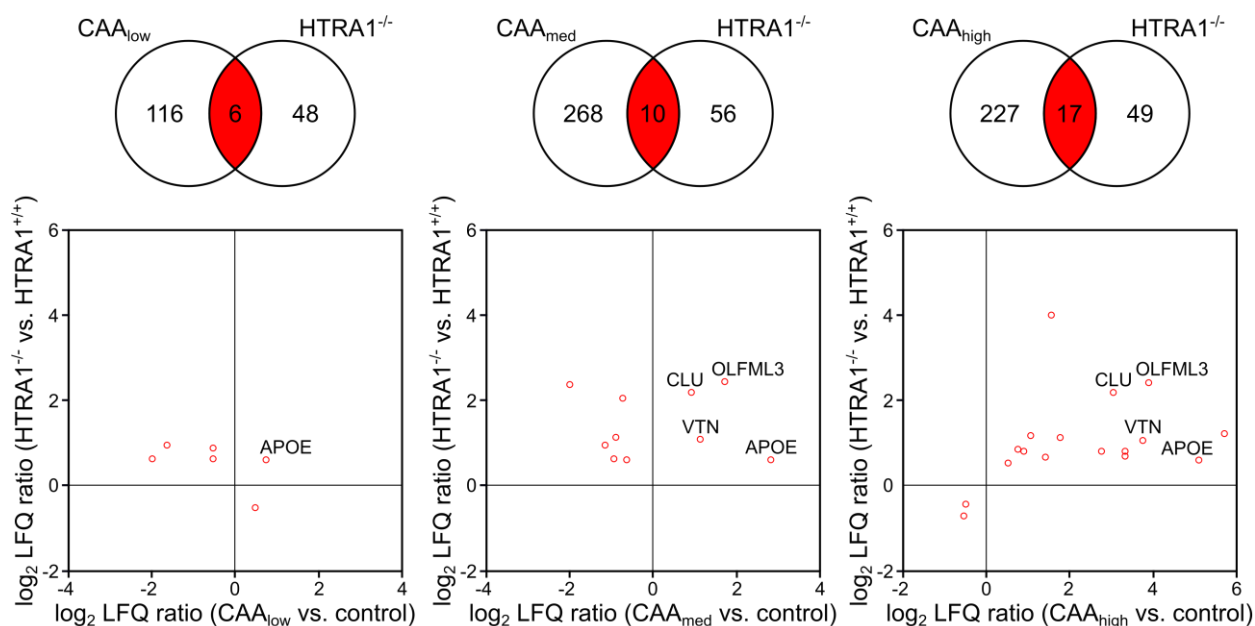
Figure 3.27: Proteins altered in CAA show a substantial overlap with the HTRA1$^{-/-}$ profile. (**top**): Venn diagrams illustrating the overlap of significantly altered proteins ($p < 0.05$, $\log_2$ ratio $< -0.4/ > 0.4$) in HTRA1$^{-/-}$ and CAA$_{low}$ (**left**), CAA$_{med}$ (**middle**) and CAA$_{high}$ (**right**). (**bottom**): correlation of $\log_2$ ratios for each overlapping protein. For each comparison, only proteins identified in at least three samples of the respective groups were considered.

To examine whether HTRA1 loss-of-function is a major contributor to the overlap between the CADASIL and the CAA$_{high}$ profile, a three-way comparison with the HTRA1$^{-/-}$ profile was performed resulting in 10 shared proteins (Figure 3.28 and Table 5.6). Strikingly, they included almost all of the most strongly accumulating proteins in the CADASIL-CAA$_{high}$ overlap and the vast majority of highly enriched proteins in the CAA$_{high}$ profile, demonstrating a critical contribution of the HTRA1 loss-of-function profile. Thus, a lack in HTRA1-mediated substrate cleavage might represent a key process in CADASIL as well as in CAA pathogenesis.
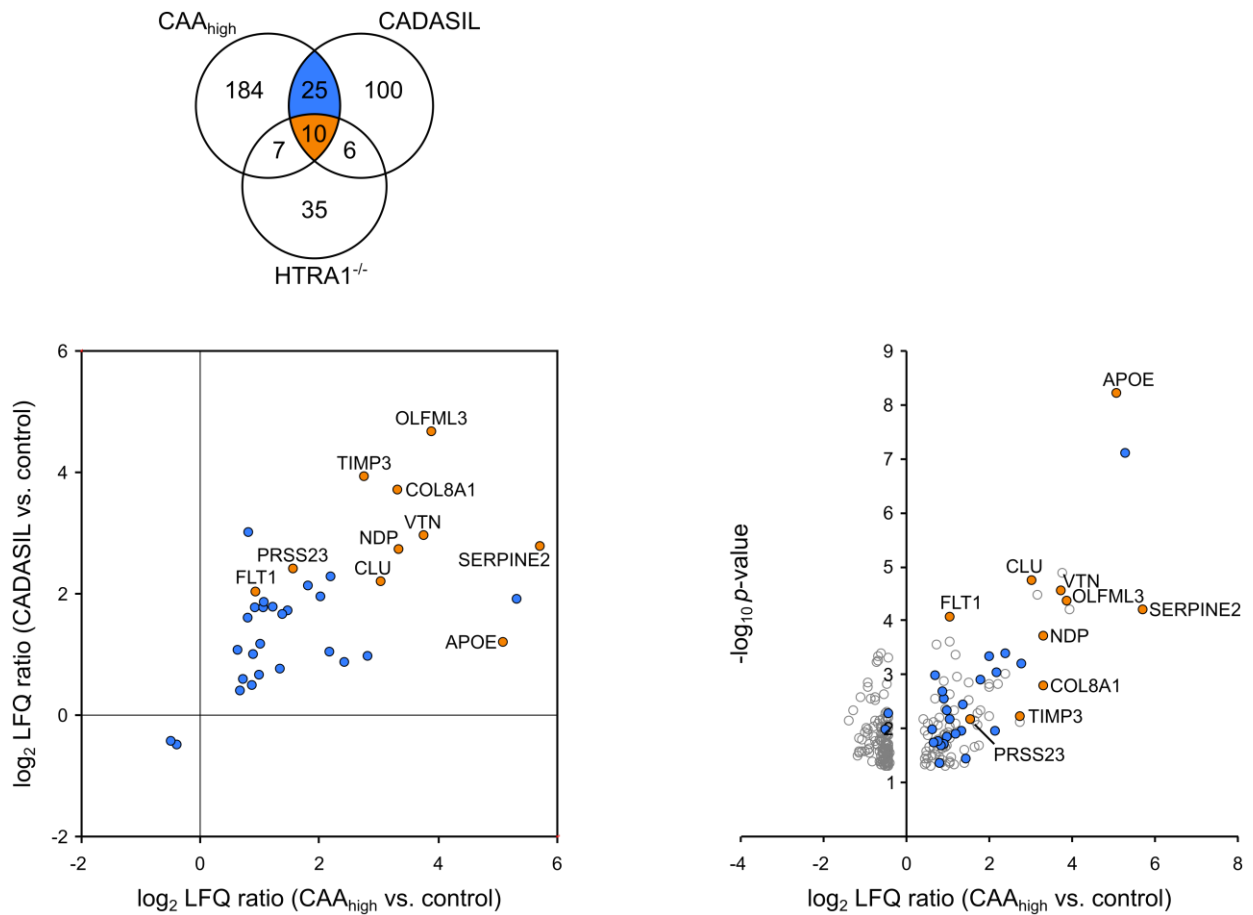
Figure 3.28: Correlation of abundance changes between CAA$_{high}$ and CADASIL. (**top**): Overlap of significantly altered proteins ($p < 0.05$, log$_2$ ratio $< -0.4/ > 0.4$) in CADASIL, HTRA1$^{-/-}$ and CAA$_{high}$ proteomic profiles. Only proteins were considered identified in at least three samples of each groups. (**bottom, left**): Log$_2$ LFQ ratios of overlapping proteins between CAA$_{high}$ vs. control and CADASIL vs. control. The 10 proteins additionally overlapping with the HTRA1$^{-/-}$ profile are labeled with gen names and are filled in orange. (**bottom, right**): Volcano plot of log$_2$ LFQ ratios and $-$log$_{10}$ p-values of the 226 significantly altered proteins in CAA$_{high}$ patients vs. control subjects. Blue filling indicates proteins overlapping with the CADASIL profile, orange filling indicates proteins additionally overlapping with the HTRA1$^{-/-}$ profile.

4 DISCUSSION

The pathomechanisms underlying CADASIL and CAA, two important protein misfolding diseases of the cerebral microvasculature, are so far only incompletely understood impeding the development of therapeutic approaches. In this thesis, proteomic analyses of patient autopsy samples were conducted to determine disease-specific protein abundance profiles, to elucidate cellular pathways involved in disease pathogenesis and to search for potential therapeutic targets.

4.1 The CADASIL and CAA brain vessel proteomes

In CADASIL, the mutation-induced accumulation and deposition of Notch3^{ECD} in small brain vessels represents an early manifestation and hallmark of the disease (Chabriat et al. 2009). As this process begins more than a decade prior to the appearance of neurological symptoms, it is considered as the starting point of pathogenesis followed by the recruitment and sequestration of functionally important extracellular matrix (ECM) and ECM-associated (matricellular) proteins, and vascular dysfunction (Joutel 2011). In the past, several studies have aimed to elucidate the composition of CADASIL-typical protein aggregates by applying proteomic approaches. However, they all differed fundamentally from the present study and exhibited various limitations. While Monet-Leprêtre and colleagues analyzed Notch3^{ECD} enriched samples by performing sequential biochemical fractionation of whole brain material (Monet-Lepretre et al. 2013), Arboleda-Velasquez et al. and Nagatoshi et al. used laser capture microdissection to collect brain arteries and arterioles for proteomic measurement (Arboleda-Velasquez et al. 2011; Nagatoshi et al. 2017). The overall small sample size (one, two or three patients respectively) and a limited sensitivity in peptide mass identification precluded a comprehensive quantification and resulted in the identification of only a short list of disease-associated protein candidates.

In the present study, a vessel isolation technique yielding highly pure fractions of small and medium-sized brain vessels from post-mortem autopsy samples was combined with state-of-the-art liquid chromatography coupled with tandem mass spectrometry (LC-MS/MS) and label-free quantification. The proteomic profile obtained from six patients showed unprecedented depth, represents the most comprehensive analysis of CADASIL-affected vessels to date and reveals a detailed view of disease-relevant protein abundance alterations. An overall tendency towards protein accumulation was observed, with Notch3 exhibiting the highest enrichment and the lowest p-value. Among the proteins with significantly increased abundance, secreted and extracellular

space proteins were strongly overrepresented, and almost all proteins previously reported to accumulate in CADASIL could be confirmed. These data thus provide further evidence for an essential role of the ECM in CADASIL. Additionally, a number of proteins with reduced abundance were identified which primarily locate to the mitochondrion. Pathway analysis revealed oxidative phosphorylation as the most significantly affected pathway and indicated a defect in energy metabolism. Considering that mitochondrial dysfunction contributes to various neurological conditions (Karbowski et al. 2012) and that structural and functional mitochondrial abnormalities have been reported in CADASIL (de la Pena et al. 2001; Malandrini et al. 2002), a reduction of mitochondrial energy production might contribute to disease progression, but could also be the result from an adaptation of vascular cells to chronic ischemia. Further studies are required to reveal the underlying molecular details.

In cerebral amyloid angiopathy (CAA), pathogenesis is initiated by the accumulation of amyloid beta peptides (Aβ) in brain vessel walls. To identify proteins coaccumulating with Aβ deposits in CAA patients, several proteomic studies have analyzed dissected leptomeningeal arteries or vascular material obtained by laser capture microdissection (Endo et al. 2019; Inoue et al. 2017; Manousopoulou et al. 2017; Hondius et al. 2018). However, only a small number of significantly altered proteins has emerged from these studies and due to the differences in sample material (predominantly large vessels) and proteomic methodology, a meaningful comparison with the CADASIL brain vessel proteome was not possible. Therefore, in this thesis a more comprehensive profile, based on 15 CAA cases and nine control subjects, was determined by using the vessel isolation procedure and mass spectrometry technique established in the CADASIL study. Since the amyloid load in CAA is known to vary considerably between different brain regions (Charidimou et al. 2012), Aβ levels in individual brain vessel extracts were determined by immunoblotting prior to proteomic analyses, leading to a classification in three groups (CAA$_{low}$, CAA$_{med}$ and CAA$_{high}$). The corresponding proteomes exhibited increasing divergence from the control group, with CAA$_{high}$ showing the highest extent of protein abundance changes, resulting in the identification of various significantly altered proteins. While the majority of previously reported proteins were confirmed, a large number of novel candidates was identified. Thus, this study provides a comprehensive picture of CAA-associated protein abundance changes and the opportunity to study pathological processes shared by CADASIL and CAA.

A comparison between the CADASIL and CAA$_{high}$ brain vessel proteomes revealed a massive overlap of significantly altered proteins, with the vast majority enriched in both profiles and

classified as secreted or part of the extracellular space. The most intriguing among the shared proteins was high temperature requirement protein A1 (HTRA1), a protease genetically linked to cerebral small vessel disease. Therefore, the potential consequences of HTRA1 accumulation in the protein deposits characterizing CADASIL and CAA pathology were investigated in more detail.

4.2 HTRA1 inactivation in cerebral small vessel diseases

HTRA1 belongs to a family of serine proteases which is highly conserved across pro- and eukaryotes. Genetic data highlight an important role of HTRA1 in the human vasculature, as mutations affecting its catalytic activity (Beaufort et al. 2014; Hara et al. 2009; Nozaki et al. 2016; Verdura et al. 2015) or mRNA stability (Hara et al. 2009; Shiga et al. 2011) are reported to cause the cerebral small vessel disease CARASIL. This is now further supported by a biochemical characterization of a novel HTRA1 mutation (S270Lfs*69) recently identified in patients with CARASIL symptoms (Ziaei et al. 2019). The variant was shown to lack large parts of the proteolytic domain and revealed defects in stability and/ or secretion; thus, it can clearly be considered as a loss-of-function mutation.

In addition to elevated protein levels of HTRA1 in brain vessel extracts of CADASIL and CAA patients, immunostaining experiments revealed a strong colocalization with vascular Notch3^{ECD} and Aβ deposits indicating HTRA1 recruitment. Sequestration of proteins into aggregates followed by their functional inactivation has been proposed as a critical mechanism in the pathogeneses of various neurodegenerative diseases (Olzscha et al. 2011; Hartl 2017). Thus, HTRA1 proteolytic capacity might be impaired in CADASIL and CAA, a hypothesis in agreement with the established genetic loss-of-function of HTRA1 in the SVD CARASIL. Indeed, in both CADASIL and CAA$_{high}$ proteomic profiles, the enrichment of several previously reported HTRA1 substrates was observed. Earlier studies using peptide library screenings suggested a broad range of potential HTRA1 substrates including several structural and extracellular matrix proteins (Runyon et al. 2007; Chien et al. 2009). To learn more about the vascular consequences of a complete loss of HTRA1 activity in humans, the analysis of CARASIL patient brain vessels would have been desirable, but was not possible due to a lack of suitable autopsy material. Therefore, the brain vessel proteome of HTRA1 deficient mice was determined revealing a significant enrichment of nearly hundred proteins, among them various reported substrates. For a number of so far undescribed substrates, processing was verified *in vitro*. A comparison of the proteomic HTRA1

loss-of-function signature with the CADASIL or CAA$_{high}$ profiles demonstrated a strong overlap of 19 and 17 proteins respectively. Strikingly, these proteins included the majority of the most highly enriched proteins in each individual dataset. Additionally, more than 50% of the overlapping proteins were shared between the CADASIL and CAA profiles, suggesting common pathological processes downstream of HTRA1. The strong overrepresentation of extracellular factors was in agreement with the preferential location of HTRA1 and its well described role in the extracellular space (Clausen et al. 2011; Grau et al. 2005; Tiaden et al. 2013). Collectively, these data propose an important role of HTRA1 in the vasculature and suggest an impairment of HTRA1 catalytic activity in CADASIL and CAA due to its recruitment and sequestration into pathological protein deposits (Figure 4.1).
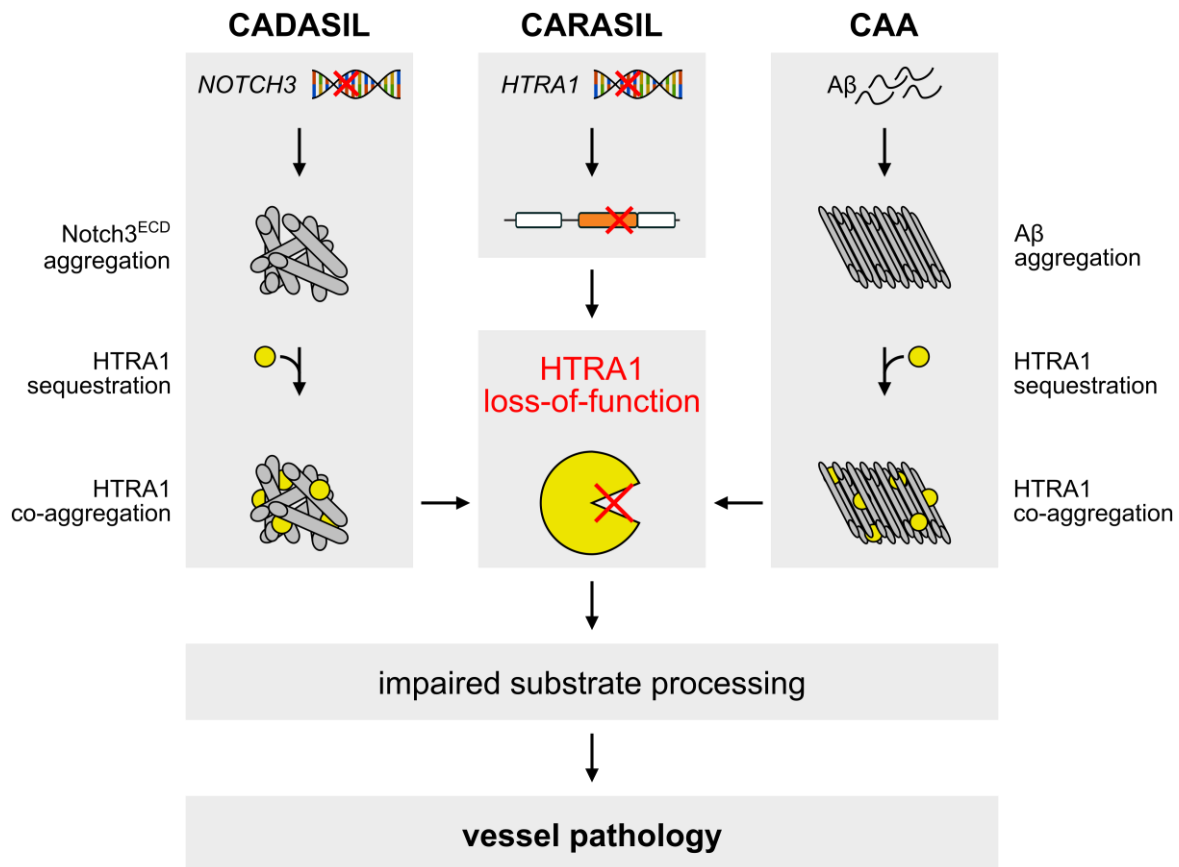
Figure 4.1: HTRA1 inactivation as shared pathomechanism in CARASIL, CADASIL and CAA. While in CARASIL genetic mutations directly affect HTRA1 proteolytic activity, in CADASIL and CAA a loss-of-function is caused by HTRA1 sequestration into pathological Notch3^{ECD} or Aβ aggregates. Impaired substrate processing might represent a key step towards a failure in maintaining vascular function in SVD pathogenesis.

So far, a loss of HTRA1 proteolytic activity in CARASIL was believed to result in the accumulation of definite substrates with specific roles in disease pathogenesis. The loss of vascular smooth muscle cells as well as the fibrotic thickening of vessel walls have been suggested to be

the result of a dysregulation of the TGFβ signaling pathway (Nozaki et al. 2014), however, the molecular details are still an unresolved question. While Beaufort and coworkers previously demonstrated HTRA1-mediated processing of latent TGFβ-binding protein 1 (LTBP-1) and observed reduced TGFβ pathway activity in HTRA1 knockout mice (Beaufort et al. 2014), others identified TGFβ receptors or TGFβ itself as a substrate and reported pathway activation under HTRA1 deficiency (Hara et al. 2009; Shiga et al. 2011; Graham et al. 2013).

LTBPs control and regulate the availability of biological active TGFβ ligands by sequestration of their latent forms within the ECM (Hynes 2009). The elevated levels of LTBP-1 and LTBP-4 in the HTRA1 knockout mouse proteome provided further support for their HTRA1-mediated processing *in vivo*. In the CADASIL proteomic profile a strong accumulation of LTBP-1 was observed, in agreement with a recent study demonstrating its colocalization with Notch3[ECD] deposits in patients and its coaggregation with mutant Notch3[ECD] *in vitro* (Kast et al. 2014). All other LTBP forms were rarely or not at all detected in control samples preventing statistical evaluation. However, LTBP-2 and LTBP-4 were present in 50% respectively 100% of patient samples indicating higher abundance in CADASIL. In CAA, the situation is less clear, since none of the LTBPs was found to be elevated in our study. This is in contrast to the study by Manousopoulou and coworkers which reported LTBP-1, LTBP-2 and LTBP-4 accumulation in leptomeningeal arteries (Manousopoulou et al. 2017). Antibody-based detection approaches might be required to determine their protein levels in CADASIL and CAA conclusively. In both the CADASIL and the CAA dataset, other components of the TGFβ pathway including TGFβ ligands and classical TGFß target proteins such as PAI-1 and CTGF were identified only in isolated samples or not at all preventing conclusions about pathway activity. Further studies assessing the phosphorylation status of the TGFβ downstream signaling mediators SMAD2/ SMAD3 or quantifying TGFβ target gene transcription are required to address this question in more detail.

HTRA1 substrates present in the CADASIL and the CAA profiles included several proteins previously implicated in both diseases such as TIMP3, vitronectin and clusterin (Endo et al. 2019; Craggs et al. 2016; Arboleda-Velasquez et al. 2011; Hondius et al. 2018; Inoue et al. 2017; Monet-Lepretre et al. 2013; Manousopoulou et al. 2017), thus providing a plausible mechanism for their accumulation.

Clusterin is a secreted extracellular chaperone capable of inhibiting protein aggregation by binding to hydrophobic regions of misfolded proteins (Humphreys et al. 1999; Poon et al. 2000; Wyatt et al. 2012). It was found to be associated with numerous pathological conditions including

age-related macular degeneration (Crabb et al. 2002), Creutzfeldt-Jakob disease (Freixes et al. 2004), Parkinson disease (Sasaki et al. 2002) and Alzheimer disease (AD) (Calero et al. 2000). In CADASIL, elevated clusterin levels were reported in two independent studies, which however, provided contradictory data on its precise localization with regard to pathological aggregates (Arboleda-Velasquez et al. 2011; Craggs et al. 2016). While Arboleda-Velasquez and coworkers proposed an accumulation in close proximity to Notch3^{ECD} deposits in the tunica media, Craggs and colleagues demonstrated the enrichment in the adventitial layer of blood vessel walls and excluded a colocalization with Notch3^{ECD}. Further studies are necessary to resolve this discrepancy. In addition, clusterin levels were reported to correlate with white matter damage, although the molecular mechanism remains elusive (Craggs et al. 2016). In the context of CAA and AD, several studies demonstrated its ability to inhibit Aβ aggregation and fibril formation *in vitro* (Narayan et al. 2011; Endo et al. 2019; Yerbury et al. 2007). Moreover, in different transgenic mouse models of AD, clusterin deficiency was reported to be associated with reduced fibrillary amyloid plaques in the brain parenchyma and a striking increase in amyloid load in the vasculature (DeMattos et al. 2004; Wojtas et al. 2017). These effects have been reported to be the result of a change in Aβ$_{40}$/Aβ$_{42}$ ratio and the impairment of the perivascular drainage system in the absence of clusterin. While the mechanistic insights in the pathological role of clusterin have been reported almost exclusively in the field of AD and CAA, its accumulation in CADASIL and its involvement in different protein misfolding diseases suggests a more general role in the clearance of pathological protein deposits.

Elevated TIMP3 levels were recently reported to affect cerebral blood flow and myogenic response deficits in a mouse model of CADASIL (Capone, Cognat, et al. 2016) by modulating voltage dependent potassium (K_V) channel number in cerebral arterial myocytes via the ADAM17-HB-EGF pathway (Capone, Dabertrand, et al. 2016). In the same model, increased vitronectin levels were suggested to result in white matter lesions, although the underlying mechanism was not elucidated (Capone, Cognat, et al. 2016). In addition to CADASIL, a role of vitronectin was suggested in several other diseases characterized by protein deposition including AD (Akiyama et al. 1991), age-related macular degeneration (AMD) (Crabb et al. 2002) and CAA (Endo et al. 2019). Strikingly, purified vitronectin was reported to form oligomers and amyloid fibrils *in vitro*, which were shown to cause cellular toxicity and to disrupt membrane integrity (Shin et al. 2008). Thus, higher vitronectin levels might facilitate pathological processes contributing to disease pathogenesis.

Cell migration-inducing and hyaluronan-binding protein (CEMIP) was the second most strongly enriched protein in CADASIL and CAA$_{high}$ patients with an accumulation of more than 100-fold in both profiles (for CAA patients, a *p*-value could not be calculated due to low prevalence in the control group). In addition, it was found highly accumulated under HTRA1 deficiency and shown to be efficiently processed by HTRA1 *in vitro*. CEMIP has been shown to promote the depolymerization of the glycosaminoglycan hyaluronan (Yoshida et al. 2013; Yoshida et al. 2018), a process which is associated with a loss in vascular integrity and vascular barrier disruption (Lennon et al. 2011). Additionally, a very recent study identified CEMIP to be involved in actin cytoskeleton organization inducing fibroblast-like cell morphology in human osteoblastic stem cells (Chen et al. 2019). Fibroblasts produce important structural ECM components and considering the arteriopathy in SVD, this mechanism might be relevant for the observed fibrotic processes. It is thus conceivable that the accumulation of CEMIP could cause an impairment of hyaluronan metabolism, with possible consequences for ECM composition and vessel function. Further studies are required to elucidate the role of CEMIP and other HTRA1 substrates in the brain vasculature.

Apolipoprotein E (APOE), one of the most highly enriched proteins in the CAA$_{high}$ profile, is known to be a strong genetic risk factor for both AD and CAA (depending on the combination of the three human isoforms APOE ε2, APOE ε3 and APOE ε4) (Charidimou et al. 2017; Yamazaki et al. 2019). It had already been shown to bind Aβ peptides and to be recruited to amyloid deposits and suggested to modulate Aβ deposition by several mechanisms including acceleration of Aβ aggregation, promoting Aβ uptake by brain cells, enhancement of enzymatic Aβ degradation or facilitation of Aβ clearance via transport across the blood-brain barrier or by drainage via the interstitial fluid and the perivasculature (Yu et al. 2014). The presence of APOE in vascular Aβ deposits has been reported in a previous histological study (Verbeek et al. 1998). Moreover, enrichment of APOE (and interestingly also HTRA1) has likewise been demonstrated in a proteomic study in Tg-SwDI mice, a CAA model carrying three human amyloid precursor protein (APP) mutations (Swedish, Dutch and Iowa) (Searcy et al. 2014). APOE accumulation under HTRA1 deficiency is in agreement with a recent study from Chu and coworkers, who demonstrated APOE processing by HTRA1 *in vitro* (Chu et al. 2016). Interestingly, they observed an isoform specificity with a preference for the APOE ε4 risk allele and provided evidence for a compensatory inhibition of HTRA1-mediated Tau processing by APOE ε4, proposing a new mechanisms contributing to AD and CAA pathogenesis. The significance of APOE accumulation

in CADASIL is more difficult to assess, since no detailed experimental analyses have been reported. The influence of the APOE genotype on clinical CADASIL features was investigated in two studies, but while in one increased white matter hyperintensity volumes in APOE ε2, but not APOE ε4 carriers were reported (Gesierich et al. 2016), in the other no association with MRI lesion volumes or disease phenotype (age of onset, presence of stroke) could be detected (Singhal et al. 2004). Collectively, APOE is an important player in vascular health, but the precise molecular mechanisms underlying its contribution to SVD have still to be elucidated.

4.3   Role of HTRA1 in the degradation of misfolded proteins

In a variety of species including bacteria and plants, HTRA proteases have been described to be implicated in protein quality control processes and in the degradation of misfolded proteins (Clausen et al. 2011). HTRA1 is one of the best characterized family members in humans and besides CARASIL, it has been associated with pathological conditions such as cancer and arthritis (Skorko-Glonek et al. 2013; Milner et al. 2008)(Milner, Patel, and Rowan 2008), but also with various protein misfolding diseases including lattice corneal dystrophy (LCD) (Venkatraman et al. 2017), age-related macular degeneration (AMD) (Coleman et al. 2008) and AD (Grau et al. 2005).

In the context of AD, HTRA1 has been reported to be in close proximity to parenchymal plaques (Grau et al. 2005) and was proposed to be involved in the turnover of Aβ deposits and Tau fibrils by disintegrating its core structure (Poepsel et al. 2015) and degrading both monomers and multimers (Grau et al. 2005; Tennstaedt et al. 2012). In LCD, which is caused by the mutation-induced misfolding of transforming growth factor beta induced protein (TGFBI) and the formation of insoluble aggregates in the cornea, proteomic analysis of microdissected patients' amyloid material also revealed a strong accumulation of HTRA1 (Venkatraman et al. 2017). Moreover, Poulsen and coworkers have recently demonstrated that HTRA1 is able to process wildtype TGFBI but shows a strong preference for amyloidogenic variants (Poulsen et al. 2019). In contrast to Aβ, Tau or TGFBI processing, no HTRA1-mediated cleavage of Notch3 was observed in this study, however, considering that these experiments were performed with wildtype fragments (containing the EGF repeats 1-15), one possible explanation could be that HTRA1 requires either full length or misfolded Notch3^{ECD} for its processing. Thus, further experiments including different construct lengths with CADASIL-typical cysteine mutations are necessary to elucidate the processability of Notch3^{ECD} monomers and aggregates.

Interestingly, Sorsby fundus dystrophy (SFD), an autosomal-dominant macular disease characterized by amorphous protein deposits and an abnormal accumulation of extracellular material (Anand-Apte et al. 2019), is caused by mutations in TIMP3, which follow a stereotypic pattern highly similar to Notch3^{ECD} mutations. They also almost exclusively affect cysteine residues resulting in the disruption of structurally essential disulfide bonds. In this thesis, HTRA1-mediated TIMP3 processing was demonstrated *in vitro*, although its efficiency was only moderate. It is tempting to speculate that, similar to the processing of pathological LCD variants of TGFBI, SFD-associated mutations in TIMP3 could also increase HTRA1 processability, but further experiments are needed to address this question.

HTRA1 is characterized by the presence of a C-terminal PDZ domain, which mediates the interaction with a broad range of binding partners containing either a C-terminal or internal hydrophobic stretch (Runyon et al. 2007). Considering that the surface of a correctly folded protein is typically hydrophilic, whereas misfolded proteins tend to expose hydrophobic regions, HTRA1 might use its PDZ domain for the recognition of misfolded proteins, a process resembling the mechanism of bacterial HTRA family members (Wilken et al. 2004) as well as the proposed biological function of HtrA2/ Omi in the mitochondria (Zhang et al. 2007).

Collectively, these data suggest an involvement of HTRA1 in the degradation of misfolded extracellular proteins in a physiological situation. It might be part of an extracellular proteostasis machinery regulating protein abundance in the vessel wall (and possibly in other tissues). Under pathophysiological conditions such as mutation-induced increase in protein aggregation or aging, its capacity may be exceeded, leading to an accumulation of its substrates and eventually resulting in a collapse of the proteostasis system (Hipp et al. 2019). This is very well in agreement with the observed HTRA1 loss-of-function profile in CADASIL and CAA. Additional support is provided by proteomic analysis of amyloid plaque material in AD (Drummond et al. 2017), drusen material in AMD (Wang et al. 2010) and corneal aggregates in LCD (Venkatraman et al. 2017), in all of which elevated levels of proteins meanwhile known to be HTRA1 substrates have been reported. HTRA1 could therefore play a general role in the maintenance of extracellular proteins with implications in the pathomechanism of various protein misfolding diseases.

4.4 Conclusion

There is ample evidence for a genetic loss of HTRA1 function as cause for rare recessive as well as dominant forms of hereditary SVDs. The data obtained in this study on CADASIL and CAA patient autopsy tissue provide strong evidence for a more common role of HTRA1 in SVD pathogenesis and suggest the presence of a novel mechanism of HTRA1 inactivation on a protein level. It likely includes the recruitment of HTRA1 to pathological protein deposits in brain vessel walls and the depletion from its physiological environment. Thus, the findings of this thesis represent a major advancement in the SVD field and open new avenues for treatment approaches. HTRA1 proteolytic function requires the formation of trimers whose activation is driven by an allosteric mechanism of intermonomer communication, an elegant way for reversibly regulating protease activity (Cabrera et al. 2017). This mechanism holds the potential for the discovery or design of agents modulating HTRA1 activity and thus for developing therapeutic approaches suitable for ameliorating pathologies associated with dysregulated HTRA1 function.

5 APPENDIX

Table 5.1: Proteins significantly altered in CADASIL patients

Gene name	Ratio	p-value	Gene name	Ratio	p-value	Gene name	Ratio	p-value
NOTCH3	**144.51**	**3.53E-07**	EGFL8	2.74	1.73E-02	DBT	0.73	4.20E-02
CEMIP	**130.79**	**4.80E-04**	F13A1	2.53	1.30E-02	PCCA	0.73	1.75E-02
APCS	**65.92**	**5.79E-04**	IQGAP2	2.36	3.08E-02	OGDH	0.73	4.76E-02
OLFML3	**25.38**	**8.87E-04**	FDXR	2.32	2.22E-02	RAB11FIP5	0.72	4.58E-02
CXCL12	**21.16**	**6.68E-03**	APOE	2.29	2.86E-02	RELL1	0.72	4.90E-02
CPZ	17.11	2.26E-02	**PCMT1**	**2.24**	**4.88E-04**	ATP5H	0.72	4.32E-02
TIMP3	**15.28**	**4.61E-04**	FBLN1	2.22	1.99E-02	ZADH2	0.71	4.34E-02
CHRD	**13.34**	**5.86E-03**	DKK3	2.16	3.34E-03	EDC4	0.71	1.65E-02
COL8A1	**13.05**	**1.17E-02**	EZR	2.09	4.37E-03	DLST	0.71	1.26E-02
MFAP4	**11.88**	**2.24E-03**	STAB1	2.06	4.90E-02	MFN2	0.71	2.95E-02
CHST14	9.95	1.95E-02	CES1	2.05	6.28E-03	BTN3A3	0.71	2.00E-02
ITGB3	8.07	2.97E-02	DSG1	2.04	3.67E-02	FAM63A	0.70	4.45E-02
VTN	**7.80**	**3.71E-03**	NDUFA4L2	2.02	3.53E-02	SLC25A3	0.70	4.54E-02
SERPINE2	**6.88**	**4.12E-03**	S100A13	2.00	3.37E-02	USMG5	0.69	3.04E-02
NDP	**6.65**	**1.46E-04**	AQP1	1.97	9.85E-03	UQCRC2	0.69	4.75E-02
SEMA3G	6.61	1.56E-02	NT5E	1.97	8.16E-03	PLXNA2	0.69	4.82E-02
LUM	5.82	2.08E-02	GAS7	1.96	2.40E-02	SPECC1	0.68	2.37E-02
FMOD	5.80	1.33E-02	DAD1	1.92	1.66E-02	HSPD1	0.68	2.77E-02
OGN	5.76	1.64E-02	MLC1	1.82	2.03E-02	SACS	0.67	3.89E-02
GPNMB	**5.72**	**1.19E-03**	FAM26E	1.78	3.79E-02	CTNNA3	0.67	4.95E-02
CTSH	5.36	1.99E-02	HSPB8	1.78	3.29E-02	GRIA1	0.67	1.64E-02
PRSS23	**5.31**	**2.88E-03**	ITGB2	1.70	1.69E-02	UQCRC1	0.66	3.41E-02
FBLN2	5.18	1.93E-02	ASPH	1.68	4.55E-02	GBE1	0.66	1.25E-02
PRELP	4.89	1.10E-02	ALYREF	1.67	4.08E-02	TMEM126A	0.66	4.98E-02
HTRA1	**4.89**	**1.57E-03**	PAK2	1.66	3.81E-02	UQCRQ	0.66	2.11E-02
TGFBI	4.84	5.70E-03	SLC29A1	1.66	4.45E-02	ATP5B	0.66	3.05E-02
CLU	**4.58**	**1.59E-03**	SND1	1.65	1.80E-02	ATP5O	0.66	3.30E-02
AEBP1	4.37	9.82E-03	PPP3CB	1.63	3.00E-02	NDUFB10	0.65	3.13E-02
OLFML1	4.25	4.27E-02	JAM2	1.61	2.67E-02	RHOG	0.65	1.16E-02
COL1A1	4.22	1.62E-02	DPYSL3	1.58	1.61E-02	FAHD1	0.65	1.95E-02
SBSPON	4.18	1.08E-02	MAPK1	1.58	1.58E-02	STK39	0.64	3.71E-02
FGL2	4.09	1.07E-02	EDNRA	1.57	2.12E-02	DLD	0.64	2.15E-02
COL1A2	4.08	2.09E-02	GNG12	1.53	4.23E-02	LONP1	0.64	9.27E-03
DCN	4.05	1.89E-02	PTPRC	1.53	4.21E-02	IGBP1	0.64	4.87E-02
EFEMP1	3.92	1.16E-02	PLEC	1.50	2.26E-02	CYC1	0.64	3.74E-02
BGN	3.89	1.65E-02	CORO1C	1.50	7.43E-03	GLIPR2	0.64	1.55E-02
GFAP	3.85	9.99E-03	NUP205	1.44	4.92E-02	AFAP1L2	0.64	1.69E-02
C3	3.76	1.08E-02	LUC7L2	1.44	2.00E-03	ETFDH	0.64	5.44E-03
ELN	3.64	9.19E-03	DDX6	1.43	3.95E-02	NME2;NME2P1	0.63	4.58E-03
FLT1	3.63	3.80E-03	PPP2R5E	1.42	2.56E-02	PDHA1	0.63	4.95E-02
EMILIN2	3.57	3.65E-02	PLCD3	1.41	1.46E-02	VCAN	0.63	4.20E-02
MFGE8	3.53	3.16E-02	DGKA	1.39	3.55E-02	ATP5C1	0.63	1.72E-02
FBN1	3.52	4.25E-02	RAB12	1.37	1.85E-02	TOMM22	0.63	4.82E-03
SOD3	3.44	3.39E-02	PLSCR4	1.32	3.26E-02	DNAJB4	0.62	8.15E-03
COL6A2	3.41	9.41E-03	FAM171A1	0.76	3.91E-02	UQCRB	0.62	1.43E-02
COL12A1	3.40	2.47E-02	ACAA1	0.75	1.62E-02	ACAD8	0.62	3.59E-02
CELSR2	3.36	4.33E-02	FAM160B1	0.75	2.19E-02	MRPS36	0.62	4.65E-03
COL6A3	3.33	1.31E-02	PURA	0.75	7.81E-03	COQ9	0.62	2.40E-02
C1QC	3.29	7.80E-03	SLC12A2	0.74	2.51E-03	ATP6V1G1	0.62	1.45E-03
PTGDS	3.17	3.55E-03	ATP5D	0.74	2.88E-03	CHCHD6	0.62	2.34E-02
COL6A1	3.04	1.63E-02	COPZ1	0.73	4.48E-02	STXBP6	0.61	2.42E-02

Significance threshold: $p < 0.05$; abundance ratio > 1.32-fold ($2^{0.4}$) or < 0.76-fold ($2^{-0.4}$)
Bold entries passed multivariate statistical testing (FDR = 0.05, S0 = 0.3).

Table 5.1: Proteins significantly altered in CADASIL patients (continued)

Gene name	Ratio	*p*-value	Gene name	Ratio	*p*-value	Gene name	Ratio	*p*-value
FTL	0.61	4.51E-02	FTH1	0.56	1.05E-02	NCALD	0.46	3.35E-02
USP47	0.61	1.63E-02	SLC27A4	0.56	8.36E-03	GNG7	0.45	2.18E-02
DHRS4	0.60	1.42E-02	NCAN	0.55	2.98E-02	BCAN	0.45	4.59E-02
IDH2	0.60	4.58E-02	SLC44A1	0.54	1.63E-02	SEP4	0.43	2.91E-02
GNAI1	0.60	4.67E-02	COX4I1	0.54	2.68E-02	CADM4	0.42	4.45E-02
DLAT	0.60	3.66E-02	PDHX	0.53	3.42E-02	PMP2	0.40	7.22E-03
NDUFA7	0.59	1.54E-02	JAM3	0.53	3.44E-02	SIRT2	0.37	3.68E-02
SLC7A1	0.59	2.11E-02	AKR1C1	0.52	2.15E-02	HAPLN2	0.35	3.47E-02
SLC25A5	0.59	1.74E-02	CISD1	0.51	4.03E-02	HAPLN1	0.34	1.73E-02
NDUFB1	0.57	6.22E-03	MT-ND1	0.49	4.00E-02	MAG	0.33	3.47E-02
BECN1	0.57	3.20E-02	MT-CO2	0.49	3.22E-02	HLA-C	0.17	4.03E-02
HIP1R	0.57	3.17E-02	MBP	0.48	4.95E-02	-	-	-
PDHB	0.56	3.03E-02	LIMS2	0.48	1.05E-02	-	-	-

Significance threshold: $p < 0.05$; abundance ratio > 1.32-fold ($2^{0.4}$) or < 0.76-fold ($2^{-0.4}$)

Table 5.2: Proteins significantly altered in HTRA1$^{-/-}$ mice

Gene name	Ratio	p-value	Gene name	Ratio	p-value	Gene name	Ratio	p-value
C1QTNF4	**16.74**	**3.21E-08**	**PTPRS**	**1.85**	**2.56E-04**	SLC38A2	1.35	4.85E-02
SVEP1	**16.05**	**1.77E-05**	**PLOD1**	**1.81**	**1.10E-06**	TPP2	1.33	8.13E-03
PRSS23	**15.90**	**6.97E-06**	GREM2	1.76	1.48E-02	PEF1	1.33	3.88E-02
CEMIP	**14.93**	**2.52E-05**	**TIMP3**	**1.75**	**2.08E-03**	PSMB5	1.33	1.55E-03
EGFL8	**13.89**	**2.58E-07**	**NDP**	**1.74**	**2.15E-03**	LANCL1	1.32	4.68E-03
ADAMTSL1	**12.42**	**5.38E-06**	**ITM2B**	**1.73**	**1.07E-04**	ZBTB20	0.76	2.00E-02
LTBP1	**9.54**	**2.04E-05**	**MEGF6**	**1.71**	**3.44E-05**	RPRD1B	0.76	1.78E-02
LTBP4	**7.90**	**7.67E-06**	**RAB4B**	**1.65**	**1.29E-03**	ADAM9	0.75	1.55E-02
SEMA3G	**7.29**	**5.21E-08**	**NUTF2**	**1.64**	**4.53E-08**	CDH2	0.75	2.95E-02
ELN	**7.09**	**3.77E-04**	**CRTAC1**	**1.63**	**2.22E-05**	ARID1A	0.75	3.78E-03
OLFML3	**5.33**	**3.31E-03**	**CD55**	**1.63**	**8.86E-04**	CBX1	0.74	2.31E-02
FBLN5	**5.08**	**1.40E-04**	**VASN**	**1.63**	**1.89E-03**	LUC7L3	0.74	1.34E-03
WNT6	**4.81**	**2.67E-06**	**TGFB2**	**1.62**	**1.89E-03**	SLC7A1	0.74	4.93E-03
CLU	**4.53**	**7.93E-07**	COL8A1	1.61	4.52E-02	NHP2	0.73	1.20E-02
NTN3	**4.24**	**2.64E-04**	**GAA**	**1.61**	**6.93E-04**	CAMKV	0.73	1.93E-02
EGFL7	**4.11**	**5.56E-06**	NTN1	1.60	6.40E-03	GFER	0.72	5.83E-03
H2-Q8	**3.97**	**1.73E-03**	**PXDN**	**1.59**	**5.23E-04**	SERPINA3K	0.72	8.63E-03
PCOLCE	**3.33**	**1.61E-04**	HAPLN4	1.58	1.82E-02	BUD31	0.71	1.11E-02
PDGFB	**3.31**	**4.68E-05**	**PLTP**	**1.57**	**4.38E-05**	APOA1	0.71	4.75E-02
CPXM2	**3.21**	**2.61E-03**	JAG1	1.57	2.87E-03	CTCF	0.71	1.93E-03
WNT4	**3.08**	**3.07E-04**	**TGFB1**	**1.56**	**1.07E-03**	NTRK2	0.71	1.80E-02
SEMA3B	**2.98**	**1.87E-03**	**PLOD3**	**1.54**	**1.38E-03**	PSD3	0.70	5.09E-03
THSD4	**2.88**	**2.57E-05**	**MMRN2**	**1.53**	**4.22E-05**	FYN	0.69	6.78E-03
WNT5B	**2.75**	**1.76E-04**	SEMA3F	1.53	5.88E-03	SFPQ	0.68	2.15E-02
CELSR2	**2.64**	**3.61E-04**	CRLF1	1.53	1.22E-02	KLHL22	0.68	4.76E-02
ITM2C	**2.56**	**2.39E-06**	WNT5A	1.52	2.81E-03	ATP11A	0.68	2.71E-02
SULF1	**2.56**	**6.41E-04**	JAG2	1.52	5.44E-03	COX17	0.66	2.15E-02
MEST	**2.48**	**1.89E-03**	EMILIN1	1.50	1.05E-02	ZFPL1	0.66	9.17E-03
SERPINE2	**2.34**	**2.16E-07**	APOE	1.50	2.71E-03	RBM4B;RBM4	0.65	3.13E-02
OLFML2A	**2.34**	**8.32E-04**	ARHGDIA	1.48	1.10E-02	MAZ	0.65	7.69E-03
TSPO	2.30	3.08E-02	SH3D21	1.48	4.35E-02	DNTTIP1	0.65	3.69E-02
TRIL	**2.28**	**8.85E-06**	RAB11A	1.46	2.77E-03	RPL36	0.63	2.36E-02
FLT1	**2.27**	**1.89E-06**	MCTS1;MCTS2	1.45	9.18E-03	PLSCR1	0.62	7.35E-03
CNTNAP1	**2.18**	**4.33E-04**	SH3BGRL	1.45	6.63E-03	SPTB	0.61	4.26E-02
FBLN2	**2.18**	**6.47E-04**	PLD3	1.45	2.26E-03	MUG1	0.61	3.82E-03
ADAMTSL4	**2.18**	**2.36E-04**	SH3GL1	1.42	2.34E-02	YIPF5	0.60	3.64E-02
MATN2	**2.17**	**1.04E-04**	CAB39	1.40	1.40E-02	D2HGDH	0.60	2.84E-02
EFEMP1	**2.09**	**2.07E-03**	ST3GAL6	1.40	1.06E-02	A2M	0.50	1.03E-02
VTN	**2.09**	**8.35E-05**	BZW1	1.40	2.58E-02	**ZNF22**	**0.44**	**1.34E-04**
EGFLAM	**2.03**	**8.15E-07**	PARVA	1.39	2.49E-02	**C1QTNF5**	**0.43**	**3.71E-04**
DIA1	**1.98**	**5.10E-03**	C1QTNF7	1.37	1.36E-02	SLC4A1	0.36	4.75E-02
CXCL12	**1.91**	**8.38E-05**	TPD52	1.36	4.76E-02	-	-	-
FN1	**1.91**	**2.13E-03**	TAGLN	1.35	2.99E-02	-	-	-

Significance threshold: $p < 0.05$; abundance ratio > 1.32-fold ($2^{0.4}$) or < 0.76-fold ($2^{-0.4}$)
Bold entries passed multivariate statistical testing (FDR = 0.05, S0 = 0.1).

Table 5.3: Proteins significantly altered in CAA$_{low}$ patients

Gene name	Ratio	*p*-value	Gene name	Ratio	*p*-value	Gene name	Ratio	*p*-value
MAPT	9.56	9.68E-03	HDHD2	1.74	1.64E-02	PCYOX1	0.69	1.86E-02
GFAP	7.31	3.42E-03	LPAR1	1.71	4.56E-02	KIAA1429	0.68	4.02E-02
MLC1	3.99	1.78E-04	APOE	1.70	3.62E-02	NID1	0.68	4.69E-02
CTNND2	3.88	3.50E-02	SDSL	1.69	4.21E-02	SUMF2	0.68	1.33E-02
PSAT1	3.73	2.01E-02	CTNNA2	1.68	2.68E-02	TM9SF3	0.67	1.25E-02
PITRM1	3.38	2.13E-02	PGK1	1.67	4.32E-02	SNF8	0.67	2.57E-02
SLC14A1	3.32	1.76E-02	MACROD1	1.64	1.07E-02	GRM3	0.66	4.59E-02
GJA1	3.28	6.14E-04	ADD3	1.61	1.62E-02	ARAF	0.66	1.84E-02
PLCD3	3.24	1.32E-03	ALDH4A1	1.54	3.36E-02	SNRPA	0.66	1.82E-02
CUL3	3.18	4.71E-02	NIT2	1.49	6.29E-03	PNN	0.65	2.40E-02
MAOB	3.18	2.75E-03	PRDX1	1.49	3.88E-02	STAT1	0.65	2.21E-02
PLXNB1	3.16	2.24E-02	ARHGAP5	1.46	5.46E-04	PCDH1	0.65	4.35E-02
PLCD1	3.12	2.96E-02	CASK	1.45	3.57E-02	MYOF	0.65	4.54E-02
CPNE6	3.06	1.39E-02	ST13;ST13P5;ST13P4	1.45	4.68E-02	CASP1	0.61	7.52E-03
HEPACAM	3.05	1.90E-02	ADD1	1.44	4.98E-02	DHRS1	0.60	4.77E-03
SERPINA3	2.94	1.74E-02	EGFR	1.42	9.20E-04	MAP6D1	0.60	4.00E-02
PBXIP1	2.78	5.94E-03	CAPNS1	1.42	2.75E-02	TBC1D24	0.60	2.40E-02
CSRP1	2.77	3.52E-02	RHEB	1.41	2.15E-02	LAMA4	0.60	8.51E-03
DDAH1	2.51	4.99E-02	GRHPR	1.41	2.66E-02	SLC6A13	0.60	2.07E-02
PHGDH	2.20	3.65E-02	FYN	1.40	3.25E-02	AGRN	0.59	1.29E-02
FBXO2	2.19	4.17E-02	MCCC1	1.39	2.49E-02	GGT1;GGT3P;GGT2	0.56	1.20E-02
COTL1	2.18	3.51E-02	BCKDHB	1.39	1.09E-02	XPC	0.55	4.23E-02
CD44	2.13	3.04E-02	BPHL	1.39	4.42E-02	SULT1A4;SULT1A3	0.55	3.86E-02
GLO1	2.12	4.56E-02	SEP11	1.32	4.51E-03	MCAM	0.54	4.19E-03
GPR37L1	2.10	5.42E-03	STRN4	0.75	1.36E-02	HIST1H1C	0.54	4.89E-04
PGD	2.09	2.26E-02	TRAPPC8	0.74	1.80E-02	EWSR1	0.53	7.44E-03
AQP4	2.08	4.00E-02	ABCC9	0.74	3.29E-02	FAM105A	0.52	3.68E-02
ITIH4	2.05	4.18E-02	PRKAB1	0.74	4.25E-02	AMPD2	0.52	1.43E-02
SRR	2.03	2.19E-03	RPS14	0.73	1.91E-02	CLSTN1	0.51	1.18E-02
BPNT1	2.01	4.42E-02	NEK9	0.73	4.06E-02	ALPL	0.51	4.79E-02
CAPN5	1.96	3.63E-03	KDELC2	0.72	4.90E-02	ACVRL1	0.48	7.91E-03
ENO1	1.94	1.36E-02	LMF1	0.72	2.01E-02	CYP7B1	0.46	1.51E-02
F3	1.94	5.01E-04	NUP37	0.72	2.99E-02	PLCG2	0.46	4.93E-02
PADI2	1.93	4.75E-02	NID2	0.72	4.09E-02	CLEC14A	0.45	5.97E-03
GPD1L	1.92	4.12E-02	DNAJC3	0.71	3.11E-02	HMGN4	0.42	3.51E-02
PRDX6	1.90	1.11E-02	IST1	0.71	5.02E-03	TNXB	0.40	1.50E-02
MTSS1L	1.90	1.37E-02	PLOD3	0.70	3.20E-02	DTX3L	0.39	2.90E-02
FAM171A1	1.85	3.00E-02	PLOD1	0.70	2.61E-02	FN1	0.32	4.20E-03
PYGM	1.82	1.76E-02	NEK7	0.70	6.84E-03	MMRN2	0.25	1.58E-02
SNTA1	1.77	5.20E-03	RAD23B	0.70	1.48E-02	IGHM	0.16	2.04E-02
AKR7A2	1.76	3.69E-02	RNPS1	0.69	2.20E-02	–	–	–

Significance threshold: *p* < 0.05; abundance ratio > 1.32-fold ($2^{0.4}$) or < 0.76-fold ($2^{-0.4}$)

Table 5.4: Proteins significantly altered in CAA_med patients

Gene name	Ratio	*p*-value	Gene name	Ratio	*p*-value	Gene name	Ratio	*p*-value
APOA4	15.91	2.33E-02	RAP1GAP2	1.84	1.25E-02	DPYSL2	1.52	2.84E-02
APOE	**7.04**	**2.68E-08**	SRGAP3	1.84	1.94E-02	SLC30A9	1.52	4.35E-02
PREPL	5.10	3.23E-02	CBR1	1.84	4.48E-02	CRKL	1.52	2.41E-02
NRXN1	**5.08**	**1.16E-05**	GAS7	1.83	2.18E-02	NDUFB10	1.52	2.99E-02
PTN	4.77	3.32E-02	DDT;DDTL	1.80	2.65E-02	ARL8B	1.51	3.30E-02
APCS	4.21	1.02E-02	NAGK	1.79	3.10E-02	AKT3	1.51	7.93E-03
ALDH1L1	3.99	1.67E-02	ROGDI	1.79	3.73E-02	UFC1	1.51	4.28E-02
USMG5	3.84	4.09E-03	MAP2K1	1.77	2.55E-02	GRPEL1	1.51	2.31E-02
FKBP4	3.54	1.05E-02	NIT2	1.77	6.30E-04	IGSF9B	1.50	4.80E-02
OLFML3	3.29	4.15E-03	GSK3A	1.75	2.33E-02	TOM1	1.50	3.18E-02
C3	3.15	7.91E-03	PPM1H	1.75	3.10E-02	CDC37	1.50	1.30E-02
KIF5C	2.91	4.23E-02	PA2G4	1.74	3.28E-02	PCMT1	1.50	4.50E-02
UNC13A	2.84	1.26E-02	UBXN1	1.74	4.36E-03	IDH3A	1.50	4.90E-02
GPI	2.78	1.10E-02	TPI1	1.74	3.14E-02	RABEP1	1.49	4.30E-02
GSTM2	2.70	1.60E-02	OSBPL1A	1.73	3.91E-02	ATP5L	1.49	3.63E-02
CASKIN1	2.68	3.64E-02	FARSB	1.73	3.44E-02	DPYSL3	1.48	4.70E-02
GAD1	2.67	4.14E-02	CSRP1	1.72	4.75E-02	F3	1.48	1.51E-02
CLASP1	2.59	8.07E-03	CLIP2	1.72	4.25E-02	COTL1	1.48	3.61E-03
DLG2	2.46	4.04E-02	MVD	1.72	6.42E-03	ATP5O	1.47	4.12E-02
RGS7	2.41	5.36E-03	LRRC4B	1.71	4.91E-02	PYGM	1.46	3.42E-02
PEA15	2.39	2.55E-03	TIAM2	1.71	1.36E-03	PFN2	1.46	4.52E-02
CAPG	2.32	3.94E-03	NDUFAF4	1.71	2.19E-02	EPN1	1.46	4.88E-02
ENOPH1	2.23	3.24E-02	ITIH4	1.70	2.06E-02	FAM84B	1.46	4.18E-02
SPON1	2.20	1.24E-03	ENO2	1.70	2.88E-02	KBTBD11	1.45	3.20E-02
VTN	2.20	4.62E-03	LINGO1	1.70	4.91E-02	MCCC1	1.45	7.50E-03
HTRA1	2.18	4.85E-03	IDH3B	1.68	1.76E-02	PMPCA	1.45	2.31E-02
OLA1	2.18	3.11E-02	ENO1	1.67	1.49E-03	DIP2B	1.44	2.79E-02
TPPP	2.17	2.17E-02	YWHAE	1.67	3.50E-02	PEBP1	1.44	4.64E-02
ARHGAP26	2.16	1.42E-02	NECAP1	1.67	5.81E-03	ARMC1	1.44	3.72E-03
AKR1B1	2.16	3.13E-02	HCN2	1.67	6.95E-04	MAP2K2	1.43	2.65E-03
PLCB1	2.09	1.80E-03	TXNL1	1.66	3.52E-02	BPHL	1.43	6.83E-03
RAB3C	2.09	2.34E-02	NRXN3	1.66	3.85E-02	AP1G1	1.42	1.32E-02
PPFIA3	2.08	4.51E-02	MAOB	1.65	2.39E-02	HEBP1	1.42	3.87E-03
MPI	2.07	1.95E-02	PRDX5	1.65	4.89E-03	ST13;ST13P5;ST13P4	1.42	1.77E-02
FKBP5	2.06	3.68E-02	ADCK3	1.63	3.47E-03	CMPK1	1.41	3.50E-02
MTSS1L	2.06	9.24E-04	PAK1	1.63	4.03E-02	NDUFB4	1.40	4.42E-02
PSAT1	2.03	2.93E-02	CACNA2D3	1.62	3.86E-02	LPGAT1	1.40	2.24E-02
C6orf136	2.00	1.35E-02	RAP2A	1.61	3.30E-02	ARHGAP5	1.39	2.74E-03
HINT1	1.98	2.13E-02	COPS5	1.61	3.76E-02	FH	1.39	2.82E-02
IGSF21	1.98	3.98E-02	KIFAP3	1.61	1.67E-02	TMEM55A	1.39	3.53E-02
GSTO1	1.97	7.86E-03	PLCD1	1.61	4.13E-02	TTLL12	1.39	7.31E-03
ATP6V1G2	1.94	3.65E-02	CA2	1.60	7.02E-03	AKR7A2	1.39	2.40E-02
TPRG1L	1.93	3.50E-02	LYPLA2	1.60	3.21E-02	ALDOA	1.39	3.02E-02
AK1	1.91	3.23E-02	SH3GLB2	1.60	3.96E-02	PPAP2B	1.39	2.74E-02
ACLY	1.91	9.32E-03	XPNPEP1	1.59	1.19E-02	AK4	1.38	3.74E-02
ALDOC	1.91	1.04E-02	L2HGDH	1.58	2.64E-02	DAGLB	1.38	2.62E-02
DDAH1	1.90	4.79E-02	PGK1	1.58	1.05E-02	PPP1R7	1.38	3.37E-02
FASN	1.90	4.66E-02	MACROD1	1.58	1.85E-03	HDHD2	1.37	2.86E-02
C1QB	1.88	4.31E-02	APP	1.58	2.56E-02	ASNA1	1.37	3.38E-03
CLU	1.88	6.84E-03	FN3K	1.56	4.58E-03	STAMBP	1.36	1.87E-02
SEC14L2	1.88	3.02E-02	EIF4A2	1.56	3.66E-02	SLC25A10	1.35	9.96E-03
SLC25A18	1.88	2.06E-02	CCDC132	1.55	1.85E-02	NUDCD2	1.34	4.85E-02
ADRBK1	1.87	3.22E-02	HAGH	1.55	1.39E-02	GRHPR	1.34	3.50E-02
RAPGEF4	1.85	2.99E-03	OGT	1.54	4.69E-02	ATP6V1G1	1.34	1.66E-02
SULT4A1	1.85	2.07E-02	CKAP5	1.54	3.89E-02	TMEM126A	1.33	2.27E-02
HECTD4	1.84	6.05E-05	ACAN	1.53	2.88E-02	NDUFS2	1.33	3.92E-02

Significance threshold: $p < 0.05$; abundance ratio > 1.32-fold ($2^{0.4}$) or < 0.76-fold ($2^{-0.4}$)
Bold entries passed multivariate statistical testing (FDR = 0.05, S0 = 0.1).

Table 5.4: Proteins significantly altered in CAA_med patients (continued)

Gene name	Ratio	*p*-value	Gene name	Ratio	*p*-value	Gene name	Ratio	*p*-value
OSBPL2	1.32	3.69E-02	NUP155	0.68	1.80E-02	TRIP12	0.63	3.53E-02
EIF2AK2	0.76	4.85E-02	WDFY1	0.68	2.58E-02	ESAM	0.63	4.10E-02
KHDRBS1	0.76	2.29E-02	ILF2	0.68	3.00E-02	MCAM	0.63	6.16E-03
DNASE1L1	0.76	4.17E-02	SNAP23	0.68	3.54E-02	ZFR	0.62	3.21E-03
SF3B1	0.76	4.53E-02	ZAK	0.68	4.92E-02	SLCO2B1	0.62	4.38E-02
PRDX4	0.75	3.84E-02	SGPL1	0.68	1.91E-02	SYPL1	0.62	8.11E-03
RPL7A	0.75	3.89E-02	RPL35A	0.67	2.57E-02	CD2AP	0.61	3.87E-02
RPN2	0.75	2.98E-02	RPL32	0.67	3.21E-02	MECP2	0.61	2.60E-03
UNC45A	0.75	2.62E-02	TPR	0.67	1.76E-02	IGHG3	0.61	1.49E-02
DNM2	0.74	3.87E-02	ERC1	0.67	4.69E-02	EGFL7	0.61	2.15E-02
GHDC	0.74	1.28E-02	PRPF6	0.67	3.32E-02	PODXL	0.61	2.52E-02
AGT	0.74	2.82E-02	FUBP3	0.67	1.85E-02	OCIAD2	0.61	2.23E-02
DNAJB11	0.74	1.21E-03	CTSZ	0.67	3.64E-02	RAPH1	0.61	1.57E-02
CKAP4	0.74	9.86E-03	MYO1B	0.67	3.87E-02	ITIH5	0.60	1.14E-02
RPL6	0.74	3.72E-02	PRKD2	0.66	4.82E-02	CD151	0.60	2.46E-02
STX7	0.74	4.75E-02	RPS2	0.66	3.83E-02	HIST1H1B	0.60	4.53E-02
SF3B3	0.73	3.15E-02	NID1	0.66	5.50E-03	LEMD2	0.60	3.61E-02
HNRNPUL1	0.73	1.58E-02	CDH5	0.66	3.61E-02	PALMD	0.60	2.33E-02
LAMC1	0.73	2.56E-02	SPCS2	0.66	3.95E-02	CALD1	0.59	4.29E-02
PECAM1	0.73	3.53E-02	KANK3	0.66	2.69E-02	ITGA1	0.59	1.04E-02
STT3B	0.72	3.37E-02	RAI14	0.66	4.25E-02	GGT1;GGT3P;GGT2	0.59	1.27E-02
TRIM28	0.72	8.83E-03	GIMAP1	0.66	2.35E-02	KIAA1462	0.59	2.50E-02
ARIH2	0.72	8.28E-03	LAMA2	0.66	1.06E-02	SLC9A3R2	0.59	3.92E-02
RPL24	0.72	3.48E-02	RBMX	0.66	2.38E-02	MSH2	0.59	1.65E-02
SNRNP200	0.72	2.32E-02	HSPG2	0.65	6.50E-03	MXRA7	0.59	3.55E-03
SRPRB	0.72	3.62E-02	MYL6	0.65	8.45E-03	AKAP2	0.59	1.92E-02
PREB	0.72	9.44E-04	ACTN4	0.65	3.81E-02	MAP4K2	0.58	2.65E-02
JAM2	0.71	1.97E-02	RPS12	0.65	1.90E-02	DNMT1	0.58	1.57E-03
ARHGEF12	0.71	1.44E-02	NID2	0.65	5.32E-03	TF	0.58	2.65E-03
SNRNP40	0.71	3.29E-02	EMILIN1	0.65	4.13E-02	CD74	0.58	1.66E-02
CTSB	0.71	3.62E-02	PSIP1	0.65	1.05E-02	LAMA1	0.58	3.26E-02
GRM3	0.71	3.78E-02	CYP4X1	0.65	1.92E-02	RAD50	0.58	4.03E-02
MYH9	0.71	3.62E-02	SCARB2	0.65	4.23E-02	TFRC	0.58	1.68E-03
SEC11A	0.71	4.72E-02	ANO6	0.65	3.74E-02	PPP1R12C	0.58	5.46E-03
SHROOM1	0.71	2.59E-02	BANF1	0.65	2.12E-02	GNG4	0.57	8.68E-03
HNRNPUL2	0.71	2.04E-02	DIABLO	0.65	3.67E-02	H1F0	0.57	1.59E-02
NOS3	0.71	4.93E-02	PDLIM7	0.64	1.31E-02	SF3A1	0.56	2.13E-02
EFTUD2	0.71	4.32E-02	THRAP3	0.64	1.60E-02	LAMA4	0.56	7.73E-04
ITGA6	0.70	2.46E-02	NUP93	0.64	1.70E-02	COL18A1	0.56	6.11E-03
ANXA11	0.70	3.95E-02	DHX38	0.64	3.49E-02	SLC16A2	0.55	4.37E-02
HSD17B11	0.70	3.23E-02	PCDH1	0.64	1.26E-02	AGRN	0.55	4.08E-04
SLC20A2	0.70	4.67E-02	RANBP2	0.64	4.03E-02	STT3A	0.54	1.78E-02
MTA2	0.70	1.16E-02	ITPR3	0.64	4.05E-02	SMC3	0.54	4.25E-02
ALDH16A1	0.70	4.96E-02	SNRPD1	0.64	1.13E-02	UACA	0.54	3.36E-02
RRAS2	0.70	3.75E-03	GABPA	0.64	1.94E-02	GPR116	0.54	3.06E-02
RPL19	0.70	1.77E-02	RALY	0.64	1.27E-02	FBLN2	0.54	4.14E-03
SNF8	0.70	8.51E-03	NUMA1	0.64	1.05E-02	ENG	0.54	1.85E-02
SRSF1	0.70	4.55E-02	WFS1	0.64	4.85E-02	SGCD	0.53	4.89E-02
TRIP6	0.69	3.62E-02	CGNL1	0.64	2.89E-02	TNXB	0.53	4.15E-02
PML	0.69	2.31E-02	FAM26E	0.63	4.77E-02	CLEC14A	0.53	3.11E-03
ITGB1	0.69	1.58E-02	FGF2	0.63	9.64E-03	VWA1	0.52	2.15E-03
KIF3B	0.69	2.11E-02	ZNF512	0.63	3.19E-02	MMRN2	0.52	1.63E-03
LAMB2	0.69	1.20E-02	NOP56	0.63	4.56E-02	LSR	0.51	3.39E-02
KANK2	0.69	3.30E-02	CYB5A	0.63	3.16E-03	ADAMTSL5	0.50	8.22E-03
HSPA12B	0.69	3.81E-02	ILF3	0.63	2.35E-02	EWSR1	0.50	5.97E-03
MPRIP	0.68	1.63E-02	SAFB	0.63	2.55E-03	ELTD1	0.50	2.69E-02
HP1BP3	0.68	3.89E-02	NUMB	0.63	1.59E-02	GIMAP8	0.50	1.66E-02

Significance threshold: *p* < 0.05; abundance ratio > 1.32-fold ($2^{0.4}$) or < 0.76-fold ($2^{-0.4}$)

Table 5.4: Proteins significantly altered in CAA$_{med}$ patients (continued)

Gene name	Ratio	*p*-value	Gene name	Ratio	*p*-value	Gene name	Ratio	*p*-value
COL1A1	0.49	2.96E-02	TOP2B	0.46	2.01E-02	NOTCH3	0.36	3.53E-03
BPI	0.48	1.12E-02	CHD4	0.46	2.53E-02	JUP	0.33	1.75E-02
CSPG4	0.47	4.51E-02	FN1	0.45	1.49E-04	LAMA3	0.29	8.45E-03
C10orf54	0.46	3.32E-02	ALPL	0.45	1.10E-02	IGHM	0.28	2.17E-02
SCARF1	0.46	1.16E-02	NTN4	0.44	2.40E-02	CYP7B1	0.28	6.73E-04
SET;SETSIP	0.46	4.51E-02	HMGN2;HMGN3	0.42	1.39E-02	DSP	0.26	1.84E-02
H1FX	0.46	6.00E-03	PLXDC1	0.37	8.87E-03	FBLN5	0.25	5.52E-03

Significance threshold: $p < 0.05$; abundance ratio > 1.32-fold ($2^{0.4}$) or < 0.76-fold ($2^{-0.4}$)

Table 5.5: Proteins significantly altered in CAA$_{high}$ patients

Gene name	Ratio	p-value	Gene name	Ratio	p-value	Gene name	Ratio	p-value
APOA4	**169.92**	**7.62E-04**	HAPLN4	2.63	4.41E-02	SLC9A3R1	1.75	3.33E-02
PTN	**88.05**	**4.70E-06**	S100A16	2.61	3.66E-02	PPAP2B	1.74	6.45E-03
SERPINE2	**51.41**	**6.14E-05**	PTGDS	2.57	3.51E-03	ITGB3	1.73	4.27E-02
SRPX	**49.92**	**3.46E-04**	CYBA	2.56	5.39E-03	COL6A1	1.72	1.68E-02
C3	**39.14**	**8.01E-08**	ITGB2	2.50	1.13E-02	CPLX2	1.70	1.59E-02
APOE	**33.41**	**6.01E-09**	TNFRSF6B	2.45	6.69E-03	ENO1	1.69	8.92E-03
HTRA1	**17.42**	**2.52E-05**	HLA-DRA	2.39	7.27E-03	MVD	1.69	1.79E-02
NRXN1	**15.26**	**6.36E-05**	GJA1	2.35	1.09E-03	SYN1	1.69	2.73E-02
MGAT1	**14.85**	**1.34E-03**	SOD3	2.29	1.25E-02	TRAF2	1.67	1.10E-03
OLFML3	**14.55**	**4.23E-05**	**APOD**	**2.27**	**4.33E-04**	PLOD1	1.66	2.80E-04
PLCB1	**13.66**	**1.28E-05**	EPHA4	2.27	7.97E-03	APRT	1.65	2.35E-02
APCS	13.44	4.43E-03	WNT2B	2.26	8.14E-03	TLN2	1.64	2.77E-03
VTN	**13.23**	**2.81E-05**	TTR	2.25	4.69E-03	PLEC	1.63	1.03E-03
NDP	**9.89**	**1.88E-04**	AKR1B1	2.21	4.63E-02	SLC4A4	1.62	2.97E-02
COL8A1	**9.81**	**1.65E-03**	NAGK	2.18	1.12E-02	IPO9	1.60	2.86E-02
C1QB	**9.00**	**3.30E-05**	DDAH1	2.13	3.49E-02	RGS7	1.59	2.35E-02
CLU	**8.07**	**1.83E-05**	COTL1	2.10	7.04E-03	KBTBD11	1.58	7.78E-03
SPON1	**7.43**	**5.49E-05**	PSAT1	2.10	4.13E-02	PLSCR4	1.57	1.79E-02
MTSS1L	**7.02**	**8.85E-06**	NPTX1	2.09	2.35E-03	FBLN1	1.55	3.59E-02
GAS7	**6.90**	**6.28E-04**	FBXO2	2.09	9.17E-03	RAB31	1.54	3.27E-02
ALDH1L1	6.63	7.52E-03	COL26A1	2.08	1.29E-02	STAMBP	1.53	1.68E-02
TIMP3	6.63	6.04E-03	EDIL3	2.08	4.48E-02	EZR	1.53	1.04E-02
CFH	**6.06**	**6.30E-04**	**FLT1**	**2.07**	**8.48E-05**	DIP2B	1.49	4.97E-02
CHST14	5.94	1.64E-02	SLC1A4	2.06	1.55E-02	CYFIP2	1.48	2.17E-02
SERPINA3	**5.56**	**8.64E-04**	**F3**	**2.06**	**2.42E-04**	PFN2	1.44	3.59E-02
MLC1	**5.28**	**4.14E-04**	COL12A1	2.05	6.94E-03	PLD3	1.43	7.93E-03
B3GALT1	5.19	1.83E-02	SLC14A1	2.05	2.06E-02	SLC6A11	1.43	1.35E-02
CAPG	**5.19**	**9.84E-04**	SRPX2	2.04	4.39E-02	PFKM	1.42	3.16E-02
FBLN7	5.03	3.46E-02	AQP4	2.03	1.31E-02	CORO2B	1.42	2.63E-02
CST3	**4.58**	**1.53E-03**	SYN2	2.03	1.22E-02	CALCOCO2	1.40	1.99E-02
TGFBI	**4.51**	**9.07E-04**	GRN	1.99	2.09E-02	CTNNA2	1.40	4.26E-02
STAB1	4.43	1.10E-02	PCMT1	1.99	1.40E-02	ELMO2	1.38	1.08E-02
GFAP	**3.99**	**4.59E-04**	LGI4	1.99	4.56E-02	PYGB	1.38	3.70E-02
GPC1	3.99	5.84E-03	MPI	1.98	1.44E-02	CAPN5	1.36	4.60E-02
FGA	**3.99**	**1.69E-03**	DPYSL3	1.95	4.53E-03	ERBB2IP	1.36	2.69E-02
APP	**3.99**	**1.48E-03**	SH3GL2	1.93	1.24E-02	SDCBP	1.35	6.55E-03
C4BPA	3.73	4.12E-03	PTGR1	1.93	3.73E-02	TNS3	1.32	2.51E-02
ITIH4	**3.56**	**1.15E-03**	CD44	1.93	4.45E-03	TRIM28	0.76	2.87E-02
NQO1	3.52	3.16E-02	OLFM1	1.93	4.85E-02	RPS13	0.75	2.43E-02
HEPACAM	3.49	4.56E-03	S100A6	1.91	2.25E-02	RPL9	0.75	3.92E-02
AEBP1	**3.45**	**1.26E-03**	PLCD1	1.88	1.91E-02	DNAJB11	0.75	6.52E-03
CNTNAP1	3.34	2.04E-02	COL1A2	1.88	2.83E-03	SNRNP200	0.75	3.12E-02
FGG	3.31	5.27E-03	PBXIP1	1.86	1.35E-02	CARKD	0.75	1.00E-02
NRXN3	3.30	2.43E-02	SLC1A3	1.86	1.31E-02	DNM2	0.75	2.37E-02
FGB	3.26	8.43E-03	COL14A1	1.86	2.05E-02	SGPL1	0.75	3.27E-02
DKK3	3.18	1.26E-02	COL6A2	1.86	1.96E-02	FXR2	0.75	8.91E-03
GSTM2	3.15	2.21E-02	ITM2B	1.86	1.31E-03	PACS2	0.75	1.36E-02
DTNA	3.13	7.00E-03	ADH5	1.86	2.39E-02	RPS14	0.75	2.29E-02
PRSS23	2.90	6.58E-03	CYBB	1.84	1.17E-02	CTNND1	0.75	4.29E-02
APLP1	2.88	3.11E-02	SEP3	1.84	4.13E-02	EDC4	0.75	5.13E-03
CPNE6	2.86	1.42E-03	S100A13	1.83	2.05E-03	ACOX1	0.75	2.00E-02
SNTA1	2.86	2.95E-03	ACSBG1	1.82	3.78E-02	EIF2B3	0.75	4.26E-02
C1QC	2.73	3.75E-02	PLCD3	1.81	2.03E-02	HNRNPA1;HNRNPA1L2	0.75	9.86E-03
CLSTN1	2.70	1.58E-02	PROS1	1.80	4.95E-02	PRKAR1A	0.75	4.47E-02
GBA	2.67	2.56E-02	SLC1A2	1.77	4.31E-02	VCL	0.74	4.39E-02
C1QTNF3	2.64	1.26E-02	COL6A3	1.77	2.57E-02	RPS16	0.74	2.89E-02

Significance threshold: $p < 0.05$; abundance ratio > 1.32-fold ($2^{0.4}$) or < 0.76-fold ($2^{-0.4}$)
Bold entries passed multivariate statistical testing (FDR = 0.05, S0 = 0.1).

Table 5.5: Proteins significantly altered in CAA$_{high}$ patients (continued)

Gene name	Ratio	*p*-value	Gene name	Ratio	*p*-value	Gene name	Ratio	*p*-value
RUVBL2	0.74	5.02E-04	RALY	0.69	2.54E-02	NT5C2	0.62	3.93E-02
TAOK2	0.74	2.99E-02	RAI14	0.69	3.55E-02	RPL11	0.62	5.40E-04
RPL7	0.74	4.62E-02	HIP1	0.69	1.14E-02	PNPT1	0.61	6.04E-04
MYL6	0.74	2.73E-02	PRKAA1	0.69	1.24E-02	HDAC7	0.61	4.22E-02
TMEM245	0.74	3.28E-02	MVP	0.69	2.81E-02	EFHD1	0.61	3.90E-02
SAMM50	0.74	2.06E-02	MYLK	0.69	3.86E-02	CREB1;ATF1	0.60	2.16E-03
TNS1	0.74	3.56E-02	DDHD2	0.69	2.05E-02	RPS9	0.60	3.09E-03
ARHGEF12	0.74	4.14E-02	SRSF1	0.69	3.77E-02	CD2AP	0.60	3.35E-02
PSMD9	0.74	4.84E-02	UACA	0.69	4.79E-02	SNF8	0.60	1.04E-03
LSM3	0.73	4.11E-02	POLR2B	0.68	2.79E-02	RPL35A	0.60	2.67E-03
RPL13A	0.73	1.53E-03	LEMD3	0.68	2.31E-02	ACTN4	0.60	7.28E-03
TECR	0.73	5.03E-03	NADK2	0.68	2.68E-02	CYP4X1	0.60	9.98E-03
CDC42EP1	0.73	3.09E-02	SKIV2L	0.68	1.01E-02	PTEN	0.59	4.44E-03
PGAM5	0.73	6.47E-03	MRPL37	0.68	6.89E-03	NUCB2	0.59	1.69E-02
SART1	0.73	3.54E-02	PLSCR1	0.68	4.01E-02	EPM2AIP1	0.59	3.05E-02
TM9SF2	0.73	1.35E-02	THRAP3	0.68	3.81E-02	ABLIM1	0.58	9.36E-03
RPL28	0.73	4.28E-02	UCHL5	0.68	4.95E-02	ALPL	0.58	1.42E-02
CTTN	0.73	1.13E-02	ESAM	0.68	4.60E-02	TESC	0.57	5.50E-03
PTPN1	0.73	4.74E-02	SUMF2	0.68	1.21E-02	KHSRP	0.56	2.87E-03
CLMN	0.73	4.91E-02	TMED4	0.68	3.73E-02	MAP4K2	0.56	2.25E-02
RPL19	0.73	1.79E-02	PDLIM7	0.67	3.91E-02	CSRP2	0.56	4.24E-02
RPL23A	0.73	4.36E-02	AKT1	0.67	1.74E-02	OCLN	0.55	2.78E-02
PSMD4	0.73	1.93E-02	NUMB	0.67	4.54E-02	NIPSNAP3B	0.55	4.48E-02
AFAP1L2	0.73	4.13E-02	TOR4A	0.67	3.99E-02	SSFA2	0.54	1.94E-02
STRN3	0.72	2.38E-02	SCARB2	0.67	1.28E-02	SUN1	0.54	2.37E-02
TJP2	0.72	3.56E-02	RPL24	0.67	6.54E-03	ACADSB	0.53	1.29E-02
RPL17	0.72	7.01E-03	RPL35	0.66	4.06E-02	PLCG2	0.53	6.72E-03
MARC2	0.72	1.28E-02	EWSR1	0.66	1.04E-02	INPP5K	0.53	2.51E-02
GIMAP1	0.72	2.12E-02	SF3A3	0.66	1.70E-02	SORBS2	0.53	1.03E-02
IVD	0.72	2.57E-02	SHANK3	0.66	9.72E-03	PPP1R12C	0.53	1.74E-03
MIA3	0.72	2.58E-02	KANK3	0.66	4.75E-02	TFRC	0.52	1.46E-03
DCAKD	0.72	4.62E-02	SLC9A1	0.66	1.29E-02	CALD1	0.51	5.27E-03
STT3B	0.72	1.24E-02	TJP1	0.66	3.18E-02	PKP4	0.51	9.67E-03
MRPL1	0.72	1.38E-02	FDPS	0.66	2.49E-02	LAMP1	0.50	1.17E-02
TM9SF3	0.72	4.47E-02	NUP98	0.66	1.50E-02	HCFC1	0.50	2.62E-02
RPS3	0.71	1.81E-02	EMD	0.66	4.20E-04	RHAG	0.49	2.43E-02
DTX3	0.71	2.00E-02	MCAM	0.65	9.28E-03	TSC2	0.49	2.26E-02
PCCB	0.71	9.23E-03	RPL27	0.65	1.62E-02	EML3	0.48	1.12E-02
LIMCH1	0.71	3.53E-02	PICALM	0.65	4.68E-02	H1FX	0.48	8.52E-03
PITPNM1	0.71	5.15E-03	PCDH1	0.65	2.28E-02	SLFN5	0.48	2.72E-02
CAV1	0.71	3.73E-02	KIF3B	0.65	9.25E-03	DKK2	0.47	7.28E-03
CBX1	0.71	4.91E-02	FAM120A	0.65	2.74E-02	GPHN	0.47	1.67E-02
PDP1	0.71	1.99E-02	PSMA7	0.65	4.16E-02	CCAR1	0.46	1.48E-02
HSPA12B	0.71	3.42E-02	ARHGEF10	0.64	3.40E-02	SYNPO2	0.46	2.59E-02
RPL10A	0.71	1.64E-02	TF	0.64	1.58E-02	FUBP1	0.46	2.67E-03
OPA3	0.71	1.53E-03	ATPIF1	0.64	4.15E-02	ISG15	0.45	3.22E-02
TUBB	0.70	2.68E-02	SLC9A3R2	0.63	2.03E-02	PLXDC1	0.45	2.90E-02
KHDRBS1	0.70	2.34E-03	MPRIP	0.63	8.18E-03	DIS3	0.45	2.99E-02
PPT1	0.70	2.43E-02	RPL5	0.63	4.48E-04	PALMD	0.41	4.77E-03
STRN	0.70	4.40E-02	AKAP2	0.63	7.24E-03	LSR	0.38	6.99E-03
PCYT1A	0.70	4.97E-02	WDFY1	0.62	5.20E-03	–	–	–
SLC12A2	0.70	1.05E-02	H1F0	0.62	2.00E-02	–	–	–

Significance threshold: $p < 0.05$; abundance ratio > 1.32-fold ($2^{0.4}$) or < 0.76-fold ($2^{-0.4}$)

Table 5.6: Proteins significantly altered in CADASIL patients, CAA$_{high}$ patients and HTRA1$^{-/-}$ mice

Gene name	CADASIL vs. control		CAA$_{high}$ vs. control		HTRA1$^{-/-}$ vs. HTRA1$^{+/+}$	
	Ratio	*p*-value	Ratio	*p*-value	Ratio	*p*-value
OLFML3	**25.38**	**8.87E-04**	**14.55**	**4.23E-05**	**5.33**	**3.31E-03**
TIMP3	**15.28**	**4.61E-04**	6.63	6.04E-03	**1.75**	**2.08E-03**
COL8A1	**13.05**	**1.17E-02**	**9.81**	**1.65E-03**	1.61	4.52E-02
VTN	**7.80**	**3.71E-03**	**13.23**	**2.81E-05**	**2.09**	**8.35E-05**
SERPINE2	**6.88**	**4.12E-03**	**51.41**	**6.14E-05**	**2.34**	**2.16E-07**
NDP	**6.65**	**1.46E-04**	**9.89**	**1.88E-04**	**1.74**	**2.15E-03**
PRSS23	**5.31**	**2.88E-03**	2.90	6.58E-03	**15.90**	**6.97E-06**
CLU	**4.58**	**1.59E-03**	**8.07**	**1.83E-05**	**4.53**	**7.93E-07**
FLT1	3.63	3.80E-03	**2.07**	**8.48E-05**	**2.27**	**1.89E-06**
APOE	2.29	2.86E-02	**33.41**	**6.01E-09**	1.50	2.71E-03
CEMIP	**130.79**	**4.80E-04**	106.50	_a	**14.93**	**2.52E-05**
CXCL12	**21.16**	**6.68E-03**	-	_b	**1.91**	**8.38E-05**
SEMA3G	6.61	1.56E-02	2.97	7.16E-02	**7.29**	**5.21E-08**
FBLN2	5.18	1.93E-02	0.91	6.90E-01	**2.18**	**6.47E-04**
EFEMP1	3.92	1.16E-02	2.00	1.25E-01	**2.09**	**2.07E-03**
ELN	3.64	9.19E-03	2.81	2.74E-01	**7.09**	**3.77E-04**
CELSR2	3.36	4.33E-02	-	_c	**2.64**	**3.61E-04**
EGFL8	2.74	1.73E-02	1.02	9.42E-01	**13.89**	**2.58E-07**
SLC7A1	0.59	2.11E-02	0.89	6.99E-01	0.74	4.93E-03
PLOD1	1.41	2.42E-01	1.66	2.80E-04	**1.81**	**1.10E-06**
CBX1	1.27	3.48E-01	0.71	4.91E-02	0.74	2.31E-02
CNTNAP1	1.14	5.10E-01	3.34	2.04E-02	**2.18**	**4.33E-04**
PLSCR1	1.07	8.17E-01	0.68	4.01E-02	0.62	7.35E-03
ITM2B	1.06	7.71E-01	1.86	1.31E-03	**1.73**	**1.07E-04**
PLD3	1.05	5.77E-01	1.43	7.93E-03	1.45	2.26E-03
HAPLN4	0.66	2.69E-01	2.63	4.41E-02	1.58	1.82E-02

Significance threshold: $p < 0.05$; abundance ratio > 1.32-fold ($2^{0.4}$) or < 0.76-fold ($2^{-0.4}$)

Bold entries passed multivariate statistical testing: CADASIL vs. control (FDR = 0.05, S0 = 0.3); CAA$_{high}$ vs. control and HTRA1$^{-/-}$ vs. HTRA1$^{+/+}$ (FDR = 0.05, S0 = 0.1)

[a] Detected in 5 of 5 CAA$_{high}$ patients and 2 of 9 control subjects

[b] Detected in 5 of 5 CAA$_{high}$ patients and 0 of 9 control subjects

[c] Detected in 3 of 5 CAA$_{high}$ patients and 0 of 9 control subjects

Table 5.6: Proteins significantly altered in CADASIL patients, CAA$_{high}$ patients and HTRA1$^{-/-}$ mice (continued)

Gene name	CADASIL vs. control		CAA$_{high}$ vs. control		HTRA1$^{-/-}$ vs. HTRA1 $^{+/+}$	
	Ratio	*p*-value	Ratio	*p*-value	Ratio	*p*-value
APCS	**65.92**	**5.79E-04**	13.44	4.43E-03	-	-
CHST14	9.95	1.95E-02	5.94	1.64E-02	-	-
HTRA1	**4.89**	**1.57E-03**	**17.42**	**2.52E-05**	-	_^{d}
COL6A3	3.33	1.31E-02	1.77	2.57E-02	-	-
FBLN1	2.22	1.99E-02	1.55	3.59E-02	-	_^{e}
DKK3	2.16	3.34E-03	3.18	1.26E-02	-	-
ITGB3	8.07	2.97E-02	1.73	4.27E-02	0.98	8.82E-01
TGFBI	4.84	5.70E-03	**4.51**	**9.07E-04**	1.15	2.05E-01
AEBP1	4.37	9.82E-03	**3.45**	**1.26E-03**	1.14	5.26E-01
COL1A2	4.08	2.09E-02	1.88	2.83E-03	1.16	5.96E-01
GFAP	3.85	9.99E-03	**3.99**	**4.59E-04**	1.07	6.56E-01
C3	3.76	1.08E-02	**39.14**	**8.01E-08**	0.79	1.56E-01
SOD3	3.44	3.39E-02	2.29	1.25E-02	0.90	4.92E-01
COL6A2	3.41	9.41E-03	1.86	1.96E-02	1.13	3.20E-01
COL12A1	3.40	2.47E-02	2.05	6.94E-03	1.03	7.74E-01
C1QC	3.29	7.80E-03	2.73	3.75E-02	1.08	5.62E-01
PTGDS	3.17	3.55E-03	2.57	3.51E-03	1.12	3.74E-01
COL6A1	3.04	1.63E-02	1.72	1.68E-02	1.13	1.64E-01
PCMT1	**2.24**	**4.88E-04**	1.99	1.40E-02	1.32	3.95E-02
EZR	2.09	4.37E-03	1.53	1.04E-02	0.94	1.88E-01
STAB1	2.06	4.90E-02	4.43	1.10E-02	1.17	1.25E-01
S100A13	2.00	3.37E-02	1.83	2.05E-03	0.75	5.72E-02
GAS7	1.96	2.40E-02	**6.90**	**6.28E-04**	1.00	9.84E-01
MLC1	1.82	2.03E-02	**5.28**	**4.14E-04**	0.90	2.64E-01
ITGB2	1.70	1.69E-02	2.50	1.13E-02	0.95	5.58E-01
DPYSL3	1.58	1.61E-02	1.95	4.53E-03	1.32	1.05E-02
PLEC	1.50	2.26E-02	1.63	1.03E-03	1.06	4.86E-01
PLCD3	1.41	1.46E-02	1.81	2.03E-02	1.07	3.63E-01
PLSCR4	1.32	3.26E-02	1.57	1.79E-02	0.84	2.55E-01
SLC12A2	0.74	2.51E-03	0.70	1.05E-02	0.99	9.45E-01
EDC4	0.71	1.65E-02	0.75	5.13E-03	0.99	7.70E-01
AFAP1L2	0.64	1.69E-02	0.73	4.13E-02	-	-

Significance threshold: $p < 0.05$; abundance ratio > 1.32-fold ($2^{0.4}$) or < 0.76-fold ($2^{-0.4}$)
Bold entries passed multivariate statistical testing: CADASIL vs. control (FDR = 0.05, S0 = 0.3); CAA$_{high}$ vs. control and HTRA1$^{-/-}$ vs. HTRA1$^{+/+}$ (FDR = 0.05, S0 = 0.1)
^{d} Detected in 0 of 5 HTRA1$^{-/-}$ and 5 of 5 HTRA1$^{+/+}$ animals
^{e} Detected in 0 of 5 HTRA1$^{-/-}$ and 1 of 5 HTRA1$^{+/+}$ animals

ABBREVIATIONS

AD	Alzheimer's disease
AMD	age-related macular degeneration
ANKR	ankyrin repeats
APCS	serum amyloid P-component
APOE	apoliprotein E
APP	amyloid precursor protein
APS	ammonium persulfate
Aβ	amyloid-beta
BBB	blood-brain barrier
BCA	bicinchoninic acid
BSA	bovine serum albumin
CAA	cerebral amyloid angiopathy
CADASIL	cerebral autosomal dominant arteriopathy with subcortical infarcts and leukoencephalopathy
CARASIL	cerebral autosomal recessive arteriopathy with subcortical infarcts and leukoencephalopathy
cDNA	circular DNA
CEMIP	cell migration-inducing and hyaluronan-binding protein
CHRD	chordin
CLU	clusterin
C-terminal	carboxy-terminal
CTGF	connective tissue growth factor
CXCL12	stromal cell-derived factor 1
DAPI	4′,6-diamidin-2-phenylindol
DLL	delta-like ligand
DMEM	dulbecco's modified eagle's medium
DMSO	dimethylsulfoxid
DNA	deoxyribonucleic acid
DTT	dithiothreitol
E. coli	escherichia coli
ECD	extracellular domain
ECM	extracellular matrix

EDTA	ethylenediaminetetraacetic acid
EGF	epidermal growth factor
EGFr	EGF-like repeat
EM	electron microscopy
FASP	filter-assisted sample preparation
FBS	fetal bovine serum
FDR	false discovery rate
FL	full-length
GOM	granular osmiophilic material
HCl	hydrochloric acid
HD	heterodimerization domain
HEK	human embryonic kidney
HRP	horseradish peroxidase
HTRA1	high temperature requirement protein A1
ICD	intracellular domain
IF	immunofluorescence
IgG	immunoglobulin G
IHC	immunohistochemistry
Jag	jagged
LB	lysogeny broth
LCD	lattice corneal dystrophy
LC-MS/MS	liquid chromatography coupled with tandem mass spectrometry
LFQ	label-free quantification
LNR	lin-12/Notch Repeat
LRS	ligand recognition site
LTBP-1	latent TGFβ-binding protein 1
MEM	minimal essential medium
MFAP4	microfibril-associated glycoprotein 4
MRI	magnetic resonance imaging
mRNA	messenger RNA
MS	mass spectrometry
MWCO	molecular weight cut-off
NDP	norrin
NRR	negative regulatory region

N-terminal	amino-terminus
OLFML3	olfactomedin-like 3
PADMAL	pontine autosomal dominant microangiopathy with leukoencephalopathy
PAGE	polyacrylamide gel electrophoresis
PAI-I	plasminogen activator inhibitor-1
PBS	phosphate buffered saline
PCR	polymerase chain reaction
PDZ	postsynaptic density of 95 kDa discs large and zonula occludens 1
PRSS23	serine protease 23
qPCR	quantitative polymerase chain reaction
RNA	ribonucleic acid
Rnase	ribonuclease
RVCL	retinal vasculopathy with cerebral leukodystrophy
SERPINE2	glia-derived nexin
SDS	sodium dodecyl sulfate
SEMA3G	semaphorin-3G
SFD	Sorsby fundus dystrophy
SRPX	sushi repeat-containing protein X-linked
SVD	small vessel disease
TBS	tris buffered saline
TEMED	tetramethylethylenediame
TGFBI	transforming growth factor beta induced protein
TGF-β	transforming growth factor beta
TIMP3	tissue inhibitor of metalloproteinases 3
TM	transmembrane
Tris	tris(hydroxymethyl)-aminomethan
VD	vascular dementia
VTN	vitronectin
WB	western blotting
WMH	white matter hyperintensities

LIST OF FIGURES

LIST OF TABLES

REFERENCES

Akiyama, H., T. Kawamata, S. Dedhar, and P. L. McGeer. 1991. 'Immunohistochemical localization of vitronectin, its receptor and beta-3 integrin in Alzheimer brain tissue', *J Neuroimmunol*, 32: 19-28.

An, E., S. Sen, S. K. Park, H. Gordish-Dressman, and Y. Hathout. 2010. 'Identification of novel substrates for the serine protease HTRA1 in the human RPE secretome', *Invest Ophthalmol Vis Sci*, 51: 3379-86.

Anand-Apte, B., J. R. Chao, R. Singh, and H. Stohr. 2019. 'Sorsby fundus dystrophy: Insights from the past and looking to the future', *Journal of neuroscience research*, 97: 88-97.

Arboleda-Velasquez, J. F., J. Manent, J. H. Lee, S. Tikka, C. Ospina, C. R. Vanderburg, M. P. Frosch, M. Rodriguez-Falcon, J. Villen, S. Gygi, F. Lopera, H. Kalimo, M. A. Moskowitz, C. Ayata, A. Louvi, and S. Artavanis-Tsakonas. 2011. 'Hypomorphic Notch 3 alleles link Notch signaling to ischemic cerebral small-vessel disease', *Proc Natl Acad Sci U S A*, 108: E128-35.

Attems, J., K. Jellinger, D. R. Thal, and W. Van Nostrand. 2011. 'Review: sporadic cerebral amyloid angiopathy', *Neuropathol Appl Neurobiol*, 37: 75-93.

Baron-Menguy, C., V. Domenga-Denier, L. Ghezali, F. M. Faraci, and A. Joutel. 2017. 'Increased Notch3 Activity Mediates Pathological Changes in Structure of Cerebral Arteries', *Hypertension*, 69: 60-70.

Baudrimont, M., F. Dubas, A. Joutel, E. Tournier-Lasserve, and M. G. Bousser. 1993. 'Autosomal dominant leukoencephalopathy and subcortical ischemic stroke. A clinicopathological study', *Stroke*, 24: 122-5.

Beaufort, N., E. Scharrer, E. Kremmer, V. Lux, M. Ehrmann, R. Huber, H. Houlden, D. Werring, C. Haffner, and M. Dichgans. 2014. 'Cerebral small vessel disease-related protease HtrA1 processes latent TGF-beta binding protein 1 and facilitates TGF-beta signaling', *Proc Natl Acad Sci U S A*, 111: 16496-501.

Begley, D. J., and M. W. Brightman. 2003. 'Structural and functional aspects of the blood-brain barrier', *Prog Drug Res*, 61: 39-78.

Bousser, M. G., and E. Tournier-Lasserve. 1994. 'Summary of the proceedings of the First International Workshop on CADASIL. Paris, May 19-21, 1993', *Stroke*, 25: 704-7.

Bugiani, M., S. H. Kevelam, H. S. Bakels, Q. Waisfisz, C. Ceuterick-de Groote, H. W. Niessen, T. E. Abbink, S. A. Lesnik Oberstein, and M. S. van der Knaap. 2016. 'Cathepsin A-related arteriopathy with strokes and leukoencephalopathy (CARASAL)', *Neurology*, 87: 1777-86.

Cabrera, A. C., E. Melo, D. Roth, A. Topp, F. Delobel, C. Stucki, C. Y. Chen, P. Jakob, B. Banfai, T. Dunkley, O. Schilling, S. Huber, R. Iacone, and P. Petrone. 2017. 'HtrA1 activation is driven by an allosteric mechanism of inter-monomer communication', *Sci Rep*, 7: 14804.

Calero, M., A. Rostagno, E. Matsubara, B. Zlokovic, B. Frangione, and J. Ghiso. 2000. 'Apolipoprotein J (clusterin) and Alzheimer's disease', *Microsc Res Tech*, 50: 305-15.

Caplan, L. R. 1995. 'Binswanger's disease--revisited', *Neurology*, 45: 626-33.

Capone, C., E. Cognat, L. Ghezali, C. Baron-Menguy, D. Aubin, L. Mesnard, H. Stohr, V. Domenga-Denier, M. T. Nelson, and A. Joutel. 2016. 'Reducing Timp3 or vitronectin ameliorates disease manifestations in CADASIL mice', *Ann Neurol*, 79: 387-403.

Capone, C., F. Dabertrand, C. Baron-Menguy, A. Chalaris, L. Ghezali, V. Domenga-Denier, S. Schmidt, C. Huneau, S. Rose-John, M. T. Nelson, and A. Joutel. 2016. 'Mechanistic insights into a TIMP3-sensitive pathway constitutively engaged in the regulation of cerebral hemodynamics', *Elife*, 5.

Carare, R. O., C. A. Hawkes, M. Jeffrey, R. N. Kalaria, and R. O. Weller. 2013. 'Review: cerebral amyloid angiopathy, prion angiopathy, CADASIL and the spectrum of protein elimination failure angiopathies (PEFA) in neurodegenerative disease with a focus on therapy', *Neuropathol Appl Neurobiol*, 39: 593-611.

Chabriat, H. 2017. 'Cerebral Autosomal Dominant Arteriopathy with Subcortical Infarcts and Leukoencephalopathy CADASIL.' in P. Sharma and J.F. Meschia (eds.), *Stroke Genetics* (Springer International Publishing).

Chabriat, H., A. Joutel, M. Dichgans, E. Tournier-Lasserve, and M. G. Bousser. 2009. 'Cadasil', *Lancet Neurol*, 8: 643-53.

Chabriat, H., C. Levy, H. Taillia, M. T. Iba-Zizen, K. Vahedi, A. Joutel, E. Tournier-Lasserve, and M. G. Bousser. 1998. 'Patterns of MRI lesions in CADASIL', *Neurology*, 51: 452-7.

Chabriat, H., E. Tournier-Lasserve, K. Vahedi, D. Leys, A. Joutel, A. Nibbio, J. P. Escaillas, M. T. Iba-Zizen, S. Bracard, A. Tehindrazanarivelo, and et al. 1995. 'Autosomal dominant migraine with MRI white-matter abnormalities mapping to the CADASIL locus', *Neurology*, 45: 1086-91.

Charidimou, A., G. Boulouis, M. E. Gurol, C. Ayata, B. J. Bacskai, M. P. Frosch, A. Viswanathan, and S. M. Greenberg. 2017. 'Emerging concepts in sporadic cerebral amyloid angiopathy', *Brain*, 140: 1829-50.

Charidimou, A., Q. Gang, and D. J. Werring. 2012. 'Sporadic cerebral amyloid angiopathy revisited: recent insights into pathophysiology and clinical spectrum', *J Neurol Neurosurg Psychiatry*, 83: 124-37.

Chen, J., S. Van Gulden, T. L. McGuire, A. C. Fleming, C. Oka, J. A. Kessler, and C. Y. Peng. 2018. 'BMP-Responsive Protease HtrA1 Is Differentially Expressed in Astrocytes and Regulates Astrocytic Development and Injury Response', *J Neurosci*, 38: 3840-57.

Chen, L., K. Shi, T. L. Andersen, W. Qiu, and M. Kassem. 2019. 'KIAA1199 is a secreted molecule that enhances osteoblastic stem cell migration and recruitment', *Cell Death Dis*, 10: 126.

Chien, J., X. He, and V. Shridhar. 2009. 'Identification of tubulins as substrates of serine protease HtrA1 by mixture-based oriented peptide library screening', *J Cell Biochem*, 107: 253-63.

Chu, Q., J. K. Diedrich, J. M. Vaughan, C. J. Donaldson, M. F. Nunn, K. F. Lee, and A. Saghatelian. 2016. 'HtrA1 Proteolysis of ApoE In Vitro Is Allele Selective', *J Am Chem Soc*, 138: 9473-8.

Clausen, T., M. Kaiser, R. Huber, and M. Ehrmann. 2011. 'HTRA proteases: regulated proteolysis in protein quality control', *Nat Rev Mol Cell Biol*, 12: 152-62.

Cognat, E., C. Baron-Menguy, V. Domenga-Denier, S. Cleophax, C. Fouillade, M. Monet-Lepretre, M. Dewerchin, and A. Joutel. 2014. 'Archetypal Arg169Cys mutation in NOTCH3 does not drive the pathogenesis in cerebral autosomal dominant arteriopathy

with subcortical infarcts and leucoencephalopathy via a loss-of-function mechanism', *Stroke*, 45: 842-9.

Coleman, H. R., C. C. Chan, F. L. Ferris, 3rd, and E. Y. Chew. 2008. 'Age-related macular degeneration', *Lancet*, 372: 1835-45.

Coupland, K., U. Lendahl, and H. Karlstrom. 2018. 'Role of NOTCH3 Mutations in the Cerebral Small Vessel Disease Cerebral Autosomal Dominant Arteriopathy With Subcortical Infarcts and Leukoencephalopathy', *Stroke*, 49: 2793-800.

Cox, J., M. Y. Hein, C. A. Luber, I. Paron, N. Nagaraj, and M. Mann. 2014. 'Accurate proteome-wide label-free quantification by delayed normalization and maximal peptide ratio extraction, termed MaxLFQ', *Mol Cell Proteomics*, 13: 2513-26.

Crabb, J. W., M. Miyagi, X. Gu, K. Shadrach, K. A. West, H. Sakaguchi, M. Kamei, A. Hasan, L. Yan, M. E. Rayborn, R. G. Salomon, and J. G. Hollyfield. 2002. 'Drusen proteome analysis: an approach to the etiology of age-related macular degeneration', *Proc Natl Acad Sci U S A*, 99: 14682-7.

Craggs, L., J. Taylor, J. Y. Slade, A. Chen, C. Hagel, G. Kuhlenbaeumer, A. Borjesson-Hanson, M. Viitanen, H. Kalimo, V. Deramecourt, A. E. Oakley, and R. N. Kalaria. 2016. 'Clusterin/Apolipoprotein J immunoreactivity is associated with white matter damage in cerebral small vessel diseases', *Neuropathol Appl Neurobiol*, 42: 194-209.

Davous, P., P. Khoubesserian, P. Tric, and N. Telerman-Toppet. 1991. '[Mitochondrial encephalopathy affecting only the central nervous system]', *Rev Neurol (Paris)*, 147: 538-41.

de la Pena, P., B. Bornstein, P. del Hoyo, M. A. Fernandez-Moreno, M. A. Martin, Y. Campos, C. Gomez-Escalonilla, J. A. Molina, A. Cabello, J. Arenas, and R. Garesse. 2001. 'Mitochondrial dysfunction associated with a mutation in the Notch3 gene in a CADASIL family', *Neurology*, 57: 1235-8.

DeMattos, R. B., J. R. Cirrito, M. Parsadanian, P. C. May, M. A. O'Dell, J. W. Taylor, J. A. Harmony, B. J. Aronow, K. R. Bales, S. M. Paul, and D. M. Holtzman. 2004. 'ApoE and clusterin cooperatively suppress Abeta levels and deposition: evidence that ApoE regulates extracellular Abeta metabolism in vivo', *Neuron*, 41: 193-202.

Di Donato, I., S. Bianchi, N. De Stefano, M. Dichgans, M. T. Dotti, M. Duering, E. Jouvent, A. D. Korczyn, S. A. Lesnik-Oberstein, A. Malandrini, H. S. Markus, L. Pantoni, S. Penco, A. Rufa, O. Sinanovic, D. Stojanov, and A. Federico. 2017. 'Cerebral Autosomal Dominant Arteriopathy with Subcortical Infarcts and Leukoencephalopathy (CADASIL) as a model of small vessel disease: update on clinical, diagnostic, and management aspects', *BMC Med*, 15: 41.

Dichgans, M. 2002. 'Cerebral autosomal dominant arteriopathy with subcortical infarcts and leukoencephalopathy: phenotypic and mutational spectrum', *J Neurol Sci*, 203-204: 77-80.

Dichgans, M., J. Herzog, and T. Gasser. 2001. 'NOTCH3 mutation involving three cysteine residues in a family with typical CADASIL', *Neurology*, 57: 1714-7.

Dichgans, M., and D. Leys. 2017. 'Vascular Cognitive Impairment', *Circ Res*, 120: 573-91.

Dichgans, M., H. Ludwig, J. Muller-Hocker, A. Messerschmidt, and T. Gasser. 2000. 'Small in-frame deletions and missense mutations in CADASIL: 3D models predict misfolding of Notch3 EGF-like repeat domains', *Eur J Hum Genet*, 8: 280-5.

Dichgans, M., S. L. Pulit, and J. Rosand. 2019. 'Stroke genetics: discovery, biology, and clinical applications', *Lancet Neurol*, 18: 587-99.

Dotti, M. T., N. De Stefano, S. Bianchi, A. Malandrini, C. Battisti, E. Cardaioli, and A. Federico. 2004. 'A novel NOTCH3 frameshift deletion and mitochondrial abnormalities in a patient with CADASIL', *Arch Neurol*, 61: 942-5.

Drummond, E., S. Nayak, A. Faustin, G. Pires, R. A. Hickman, M. Askenazi, M. Cohen, T. Haldiman, C. Kim, X. Han, Y. Shao, J. G. Safar, B. Ueberheide, and T. Wisniewski. 2017. 'Proteomic differences in amyloid plaques in rapidly progressive and sporadic Alzheimer's disease', *Acta Neuropathol*, 133: 933-54.

Duering, M., A. Karpinska, S. Rosner, F. Hopfner, M. Zechmeister, N. Peters, E. Kremmer, C. Haffner, A. Giese, M. Dichgans, and C. Opherk. 2011. 'Co-aggregate formation of CADASIL-mutant NOTCH3: a single-particle analysis', *Hum Mol Genet*, 20: 3256-65.

Endo, Y., K. Hasegawa, R. Nomura, H. Arishima, K. I. Kikuta, T. Yamashita, Y. Inoue, M. Ueda, Y. Ando, M. R. Wilson, T. Hamano, Y. Nakamoto, and H. Naiki. 2019. 'Apolipoprotein E and clusterin inhibit the early phase of amyloid-beta aggregation in an in vitro model of cerebral amyloid angiopathy', *Acta Neuropathol Commun*, 7: 12.

Fouillade, C., C. Baron-Menguy, V. Domenga-Denier, C. Thibault, K. Takamiya, R. Huganir, and A. Joutel. 2013. 'Transcriptome analysis for Notch3 target genes identifies Grip2 as a novel regulator of myogenic response in the cerebrovasculature', *Arterioscler Thromb Vasc Biol*, 33: 76-86.

Fouillade, C., M. Monet-Lepretre, C. Baron-Menguy, and A. Joutel. 2012. 'Notch signalling in smooth muscle cells during development and disease', *Cardiovasc Res*, 95: 138-46.

Freixes, M., B. Puig, A. Rodriguez, B. Torrejon-Escribano, R. Blanco, and I. Ferrer. 2004. 'Clusterin solubility and aggregation in Creutzfeldt-Jakob disease', *Acta Neuropathol*, 108: 295-301.

French, C. R., S. Seshadri, A. L. Destefano, M. Fornage, C. R. Arnold, P. J. Gage, J. M. Skarie, W. B. Dobyns, K. J. Millen, T. Liu, W. Dietz, T. Kume, M. Hofker, D. J. Emery, S. J. Childs, A. J. Waskiewicz, and O. J. Lehmann. 2014. 'Mutation of FOXC1 and PITX2 induces cerebral small-vessel disease', *J Clin Invest*, 124: 4877-81.

Fukutake, T. 2011. 'Cerebral autosomal recessive arteriopathy with subcortical infarcts and leukoencephalopathy (CARASIL): from discovery to gene identification', *J Stroke Cerebrovasc Dis*, 20: 85-93.

Gesierich, B., C. Opherk, J. Rosand, M. Gonik, R. Malik, E. Jouvent, D. Herve, P. Adib-Samii, S. Bevan, L. Pianese, S. Silvestri, M. T. Dotti, N. De Stefano, J. van der Grond, E. M. Boon, F. Pescini, N. Rost, L. Pantoni, S. A. Oberstein, A. Federico, M. Ragno, H. S. Markus, E. Tournier-Lasserve, H. Chabriat, M. Dichgans, M. Duering, and M. Ewers. 2016. 'APOE varepsilon2 is associated with white matter hyperintensity volume in CADASIL', *J Cereb Blood Flow Metab*, 36: 199-203.

Ghosh, M., M. Balbi, F. Hellal, M. Dichgans, U. Lindauer, and N. Plesnila. 2015. 'Pericytes are involved in the pathogenesis of cerebral autosomal dominant arteriopathy with subcortical infarcts and leukoencephalopathy', *Ann Neurol*, 78: 887-900.

Graham, J. R., A. Chamberland, Q. Lin, X. J. Li, D. Dai, W. Zeng, M. S. Ryan, M. A. Rivera-Bermudez, C. R. Flannery, and Z. Yang. 2013. 'Serine protease HTRA1 antagonizes

transforming growth factor-beta signaling by cleaving its receptors and loss of HTRA1 in vivo enhances bone formation', *PLoS One*, 8: e74094.

Grau, S., A. Baldi, R. Bussani, X. Tian, R. Stefanescu, M. Przybylski, P. Richards, S. A. Jones, V. Shridhar, T. Clausen, and M. Ehrmann. 2005. 'Implications of the serine protease HtrA1 in amyloid precursor protein processing', *Proc Natl Acad Sci U S A*, 102: 6021-6.

Grau, S., P. J. Richards, B. Kerr, C. Hughes, B. Caterson, A. S. Williams, U. Junker, S. A. Jones, T. Clausen, and M. Ehrmann. 2006. 'The role of human HtrA1 in arthritic disease', *J Biol Chem*, 281: 6124-9.

Greenberg, S. M., J. P. Vonsattel, A. Z. Segal, R. I. Chiu, A. E. Clatworthy, A. Liao, B. T. Hyman, and G. W. Rebeck. 1998. 'Association of apolipoprotein E epsilon2 and vasculopathy in cerebral amyloid angiopathy', *Neurology*, 50: 961-5.

Haffner, C., R. Malik, and M. Dichgans. 2016. 'Genetic factors in cerebral small vessel disease and their impact on stroke and dementia', *J Cereb Blood Flow Metab*, 36: 158-71.

Hansen, G., and R. Hilgenfeld. 2013. 'Architecture and regulation of HtrA-family proteins involved in protein quality control and stress response', *Cell Mol Life Sci*, 70: 761-75.

Hara, K., A. Shiga, T. Fukutake, H. Nozaki, A. Miyashita, A. Yokoseki, H. Kawata, A. Koyama, K. Arima, T. Takahashi, M. Ikeda, H. Shiota, M. Tamura, Y. Shimoe, M. Hirayama, T. Arisato, S. Yanagawa, A. Tanaka, I. Nakano, S. Ikeda, Y. Yoshida, T. Yamamoto, T. Ikeuchi, R. Kuwano, M. Nishizawa, S. Tsuji, and O. Onodera. 2009. 'Association of HTRA1 mutations and familial ischemic cerebral small-vessel disease', *N Engl J Med*, 360: 1729-39.

Hartl, F. U. 2017. 'Protein Misfolding Diseases', *Annu Rev Biochem*, 86: 21-26.

He, L., M. Vanlandewijck, M. A. Mae, J. Andrae, K. Ando, F. Del Gaudio, K. Nahar, T. Lebouvier, B. Lavina, L. Gouveia, Y. Sun, E. Raschperger, A. Segerstolpe, J. Liu, S. Gustafsson, M. Rasanen, Y. Zarb, N. Mochizuki, A. Keller, U. Lendahl, and C. Betsholtz. 2018. 'Single-cell RNA sequencing of mouse brain and lung vascular and vessel-associated cell types', *Sci Data*, 5: 180160.

Henshall, T. L., A. Keller, L. He, B. R. Johansson, E. Wallgard, E. Raschperger, M. A. Mae, S. Jin, C. Betsholtz, and U. Lendahl. 2015. 'Notch3 is necessary for blood vessel integrity in the central nervous system', *Arterioscler Thromb Vasc Biol*, 35: 409-20.

Hipp, M. S., P. Kasturi, and F. U. Hartl. 2019. 'The proteostasis network and its decline in ageing', *Nat Rev Mol Cell Biol*, 20: 421-35.

Hondius, D. C., K. N. Eigenhuis, T. H. J. Morrema, R. C. van der Schors, P. van Nierop, M. Bugiani, K. W. Li, J. J. M. Hoozemans, A. B. Smit, and A. J. M. Rozemuller. 2018. 'Proteomics analysis identifies new markers associated with capillary cerebral amyloid angiopathy in Alzheimer's disease', *Acta Neuropathol Commun*, 6: 46.

Hughes, C. S., S. Moggridge, T. Muller, P. H. Sorensen, G. B. Morin, and J. Krijgsveld. 2019. 'Single-pot, solid-phase-enhanced sample preparation for proteomics experiments', *Nat Protoc*, 14: 68-85.

Humphreys, D. T., J. A. Carver, S. B. Easterbrook-Smith, and M. R. Wilson. 1999. 'Clusterin has chaperone-like activity similar to that of small heat shock proteins', *J Biol Chem*, 274: 6875-81.

Hynes, R. O. 2009. 'The extracellular matrix: not just pretty fibrils', *Science*, 326: 1216-9.

REFERENCES

Iadecola, C. 2017. 'The Neurovascular Unit Coming of Age: A Journey through Neurovascular Coupling in Health and Disease', *Neuron*, 96: 17-42.

Inoue, Y., M. Ueda, M. Tasaki, A. Takeshima, A. Nagatoshi, T. Masuda, Y. Misumi, T. Kosaka, T. Nomura, M. Mizukami, S. Matsumoto, T. Yamashita, H. Takahashi, A. Kakita, and Y. Ando. 2017. 'Sushi repeat-containing protein 1: a novel disease-associated molecule in cerebral amyloid angiopathy', *Acta Neuropathol*, 134: 605-17.

Ishiko, A., A. Shimizu, E. Nagata, K. Takahashi, T. Tabira, and N. Suzuki. 2006. 'Notch3 ectodomain is a major component of granular osmiophilic material (GOM) in CADASIL', *Acta Neuropathol*, 112: 333-9.

Jones, A., S. Kumar, N. Zhang, Z. Tong, J. H. Yang, C. Watt, J. Anderson, Amrita, H. Fillerup, M. McCloskey, L. Luo, Z. Yang, B. Ambati, R. Marc, C. Oka, K. Zhang, and Y. Fu. 2011. 'Increased expression of multifunctional serine protease, HTRA1, in retinal pigment epithelium induces polypoidal choroidal vasculopathy in mice', *Proc Natl Acad Sci U S A*, 108: 14578-83.

Joutel, A. 2011. 'Pathogenesis of CADASIL: transgenic and knock-out mice to probe function and dysfunction of the mutated gene, Notch3, in the cerebrovasculature', *Bioessays*, 33: 73-80.

Joutel, A., F. Andreux, S. Gaulis, V. Domenga, M. Cecillon, N. Battail, N. Piga, F. Chapon, C. Godfrain, and E. Tournier-Lasserve. 2000. 'The ectodomain of the Notch3 receptor accumulates within the cerebrovasculature of CADASIL patients', *J Clin Invest*, 105: 597-605.

Joutel, A., C. Corpechot, A. Ducros, K. Vahedi, H. Chabriat, P. Mouton, S. Alamowitch, V. Domenga, M. Cecillion, E. Marechal, J. Maciazek, C. Vayssiere, C. Cruaud, E. A. Cabanis, M. M. Ruchoux, J. Weissenbach, J. F. Bach, M. G. Bousser, and E. Tournier-Lasserve. 1996. 'Notch3 mutations in CADASIL, a hereditary adult-onset condition causing stroke and dementia', *Nature*, 383: 707-10.

Joutel, A., I. Haddad, J. Ratelade, and M. T. Nelson. 2016. 'Perturbations of the cerebrovascular matrisome: A convergent mechanism in small vessel disease of the brain?', *J Cereb Blood Flow Metab*, 36: 143-57.

Joutel, A., M. Monet-Lepretre, C. Gosele, C. Baron-Menguy, A. Hammes, S. Schmidt, B. Lemaire-Carrette, V. Domenga, A. Schedl, P. Lacombe, and N. Hubner. 2010. 'Cerebrovascular dysfunction and microcirculation rarefaction precede white matter lesions in a mouse genetic model of cerebral ischemic small vessel disease', *J Clin Invest*, 120: 433-45.

Joutel, A., M. Monet, V. Domenga, F. Riant, and E. Tournier-Lasserve. 2004. 'Pathogenic mutations associated with cerebral autosomal dominant arteriopathy with subcortical infarcts and leukoencephalopathy differently affect Jagged1 binding and Notch3 activity via the RBP/JK signaling Pathway', *Am J Hum Genet*, 74: 338-47.

Joutel, A., K. Vahedi, C. Corpechot, A. Troesch, H. Chabriat, C. Vayssiere, C. Cruaud, J. Maciazek, J. Weissenbach, M. G. Bousser, J. F. Bach, and E. Tournier-Lasserve. 1997. 'Strong clustering and stereotyped nature of Notch3 mutations in CADASIL patients', *Lancet*, 350: 1511-5.

Kalaria, R. N. 2018. 'The pathology and pathophysiology of vascular dementia', *Neuropharmacology*, 134: 226-39.

REFERENCES

Kalimo, H., M. M. Ruchoux, M. Viitanen, and R. N. Kalaria. 2002. 'CADASIL: a common form of hereditary arteriopathy causing brain infarcts and dementia', *Brain Pathol*, 12: 371-84.

Karbowski, M., and A. Neutzner. 2012. 'Neurodegeneration as a consequence of failed mitochondrial maintenance', *Acta Neuropathol*, 123: 157-71.

Kast, J., P. Hanecker, N. Beaufort, A. Giese, A. Joutel, M. Dichgans, C. Opherk, and C. Haffner. 2014. 'Sequestration of latent TGF-beta binding protein 1 into CADASIL-related Notch3-ECD deposits', *Acta Neuropathol Commun*, 2: 96.

Keage, H. A., R. O. Carare, R. P. Friedland, P. G. Ince, S. Love, J. A. Nicoll, S. B. Wharton, R. O. Weller, and C. Brayne. 2009. 'Population studies of sporadic cerebral amyloid angiopathy and dementia: a systematic review', *BMC Neurol*, 9: 3.

Kopan, R., and M. X. Ilagan. 2009. 'The canonical Notch signaling pathway: unfolding the activation mechanism', *Cell*, 137: 216-33.

Kuo, D. S., C. Labelle-Dumais, and D. B. Gould. 2012. 'COL4A1 and COL4A2 mutations and disease: insights into pathogenic mechanisms and potential therapeutic targets', *Hum Mol Genet*, 21: R97-110.

Launay, S., E. Maubert, N. Lebeurrier, A. Tennstaedt, M. Campioni, F. Docagne, C. Gabriel, L. Dauphinot, M. C. Potier, M. Ehrmann, A. Baldi, and D. Vivien. 2008. 'HtrA1-dependent proteolysis of TGF-beta controls both neuronal maturation and developmental survival', *Cell Death Differ*, 15: 1408-16.

Lee, S. J., X. Zhang, and M. M. Wang. 2014. 'Vascular accumulation of the small leucine-rich proteoglycan decorin in CADASIL', *Neuroreport*, 25: 1059-63.

Lennon, F. E., and P. A. Singleton. 2011. 'Hyaluronan regulation of vascular integrity', *Am J Cardiovasc Dis*, 1: 200-13.

Liu, H., W. Zhang, S. Kennard, R. B. Caldwell, and B. Lilly. 2010. 'Notch3 is critical for proper angiogenesis and mural cell investment', *Circ Res*, 107: 860-70.

Louvi, A., and S. Artavanis-Tsakonas. 2012. 'Notch and disease: a growing field', *Semin Cell Dev Biol*, 23: 473-80.

Maeda, S., H. Nakayama, K. Isaka, Y. Aihara, and S. Nemoto. 1976. 'Familial unusual encephalopathy of Binswanger's type without hypertension', *Folia Psychiatr Neurol Jpn*, 30: 165-77.

Malandrini, A., F. Albani, S. Palmeri, F. Fattapposta, S. Gambelli, G. Berti, A. Bracco, A. Tammaro, S. Calzavara, M. Villanova, M. Ferrari, A. Rossi, and P. Carrera. 2002. 'Asymptomatic cores and paracrystalline mitochondrial inclusions in CADASIL', *Neurology*, 59: 617-20.

Manousopoulou, A., M. Gatherer, C. Smith, J. A. R. Nicoll, C. H. Woelk, M. Johnson, R. Kalaria, J. Attems, S. D. Garbis, and R. O. Carare. 2017. 'Systems proteomic analysis reveals that clusterin and tissue inhibitor of metalloproteinases 3 increase in leptomeningeal arteries affected by cerebral amyloid angiopathy', *Neuropathol Appl Neurobiol*, 43: 492-504.

Mas, J. L., A. Dilouya, and J. de Recondo. 1992. 'A familial disorder with subcortical ischemic strokes, dementia, and leukoencephalopathy', *Neurology*, 42: 1015-9.

Milner, J. M., A. Patel, and A. D. Rowan. 2008. 'Emerging roles of serine proteinases in tissue turnover in arthritis', *Arthritis Rheum*, 58: 3644-56.

REFERENCES

Mizuta, I., A. Watanabe-Hosomi, T. Koizumi, M. Mukai, A. Hamano, Y. Tomii, M. Kondo, M. Nakagawa, H. Tomimoto, T. Hirano, M. Uchino, O. Onodera, and T. Mizuno. 2017. 'New diagnostic criteria for cerebral autosomal dominant arteriopathy with subcortical infarcts and leukocencephalopathy in Japan', *J Neurol Sci*, 381: 62-67.

Monet-Lepretre, M., I. Haddad, C. Baron-Menguy, M. Fouillot-Panchal, M. Riani, V. Domenga-Denier, C. Dussaule, E. Cognat, J. Vinh, and A. Joutel. 2013. 'Abnormal recruitment of extracellular matrix proteins by excess Notch3 ECD: a new pathomechanism in CADASIL', *Brain*, 136: 1830-45.

Monet, M., V. Domenga, B. Lemaire, C. Souilhol, F. Langa, C. Babinet, T. Gridley, E. Tournier-Lasserve, M. Cohen-Tannoudji, and A. Joutel. 2007. 'The archetypal R90C CADASIL-NOTCH3 mutation retains NOTCH3 function in vivo', *Hum Mol Genet*, 16: 982-92.

Nagatoshi, A., M. Ueda, A. Ueda, M. Tasaki, Y. Inoue, Y. Ma, T. Masuda, M. Mizukami, S. Matsumoto, T. Kosaka, T. Kawano, T. Ito, and Y. Ando. 2017. 'Serum amyloid P component: A novel potential player in vessel degeneration in CADASIL', *J Neurol Sci*, 379: 69-76.

Narayan, P., A. Orte, R. W. Clarke, B. Bolognesi, S. Hook, K. A. Ganzinger, S. Meehan, M. R. Wilson, C. M. Dobson, and D. Klenerman. 2011. 'The extracellular chaperone clusterin sequesters oligomeric forms of the amyloid-beta(1-40) peptide', *Nat Struct Mol Biol*, 19: 79-83.

Narayan, S. K., G. Gorman, R. N. Kalaria, G. A. Ford, and P. F. Chinnery. 2012. 'The minimum prevalence of CADASIL in northeast England', *Neurology*, 78: 1025-7.

Nelson, P. T., N. M. Pious, G. A. Jicha, D. M. Wilcock, D. W. Fardo, S. Estus, and G. W. Rebeck. 2013. 'APOE-epsilon2 and APOE-epsilon4 correlate with increased amyloid accumulation in cerebral vasculature', *J Neuropathol Exp Neurol*, 72: 708-15.

Nichols, Emma, Cassandra E. I. Szoeke, Stein Emil Vollset, Nooshin Abbasi, Foad Abd-Allah, Jemal Abdela, Miloud Taki Eddine Aichour, Rufus O. Akinyemi, Fares Alahdab, Solomon W. Asgedom, Ashish Awasthi, Suzanne L. Barker-Collo, Bernhard T. Baune, Yannick Béjot, Abate B. Belachew, Derrick A. Bennett, Belete Biadgo, Ali Bijani, Muhammad Shahdaat Bin Sayeed, Carol Brayne, David O. Carpenter, Félix Carvalho, Ferrán Catalá-López, Ester Cerin, Jee-Young J. Choi, Anh Kim Dang, Meaza G. Degefa, Shirin Djalalinia, Manisha Dubey, Eyasu Ejeta Duken, David Edvardsson, Matthias Endres, Sharareh Eskandarieh, Andre Faro, Farshad Farzadfar, Seyed-Mohammad Fereshtehnejad, Eduarda Fernandes, Irina Filip, Florian Fischer, Abadi K. Gebre, Demeke Geremew, Maryam Ghasemi-Kasman, Elena V. Gnedovskaya, Rajeev Gupta, Vladimir Hachinski, Tekleberhan B. Hagos, Samer Hamidi, Graeme J. Hankey, Josep M. Haro, Simon I. Hay, Seyed Sina N. Irvani, Ravi P. Jha, Jost B. Jonas, Rizwan Kalani, André Karch, Amir Kasaeian, Yousef Saleh Khader, Ibrahim A. Khalil, Ejaz Ahmad Khan, Tripti Khanna, Tawfik A. M. Khoja, Jagdish Khubchandani, Adnan Kisa, Katarzyna Kissimova-Skarbek, Mika Kivimäki, Ai Koyanagi, Kristopher J. Krohn, Giancarlo Logroscino, Stefan Lorkowski, Marek Majdan, Reza Malekzadeh, Winfried März, João Massano, Getnet Mengistu, Atte Meretoja, Moslem Mohammadi, Maryam Mohammadi-Khanaposhtani, Ali H. Mokdad, Stefania Mondello, Ghobad Moradi, Gabriele Nagel, Mohsen Naghavi, Gurudatta Naik, Long H. Nguyen, Trang H. Nguyen, Yirga L. Nirayo, Molly R. Nixon, Richard Ofori-Asenso, Felix A. Ogbo, Andrew T. Olagunju, Mayowa O. Owolabi, Songhomitra Panda-Jonas, Valéria M. de Azeredo Passos, David M. Pereira, Gabriel D. Pinilla-Monsalve, Michael A. Piradov, Constance D. Pond, Hossein Poustchi, Mostafa

Qorbani, Amir Radfar, Robert C. Reiner, Stephen R. Robinson, Gholamreza Roshandel, Ali Rostami, Tom C. Russ, Perminder S. Sachdev, Hosein Safari, Saeid Safiri, Ramesh Sahathevan, Yahya Salimi, Maheswar Satpathy, Monika Sawhney, Mete Saylan, Sadaf G. Sepanlou, Azadeh Shafieesabet, Masood A. Shaikh, Mohammad Ali Sahraian, Mika Shigematsu, Rahman Shiri, Ivy Shiue, João P. Silva, Mari Smith, Soheila Sobhani, Dan J. Stein, Rafael Tabarés-Seisdedos, Marcos R. Tovani-Palone, Bach X. Tran, Tung Thanh Tran, Amanuel T. Tsegay, Irfan Ullah, Narayanaswamy Venketasubramanian, Vasily Vlassov, Yuan-Pang Wang, Jordan Weiss, Ronny Westerman, Tissa Wijeratne, Grant M. A. Wyper, Yuichiro Yano, Ebrahim M. Yimer, Naohiro Yonemoto, Mahmoud Yousefifard, Zoubida Zaidi, Zohreh Zare, Theo Vos, Valery L. Feigin, and Christopher J. L. Murray. 2019. 'Global, regional, and national burden of Alzheimer's disease and other dementias, 1990–2016: a systematic analysis for the Global Burden of Disease Study 2016', *The Lancet Neurology*, 18: 88-106.

Nozaki, H., T. Kato, M. Nihonmatsu, Y. Saito, I. Mizuta, T. Noda, R. Koike, K. Miyazaki, M. Kaito, S. Ito, M. Makino, A. Koyama, A. Shiga, M. Uemura, Y. Sekine, A. Murakami, S. Moritani, K. Hara, A. Yokoseki, R. Kuwano, N. Endo, T. Momotsu, M. Yoshida, M. Nishizawa, T. Mizuno, and O. Onodera. 2016. 'Distinct molecular mechanisms of HTRA1 mutants in manifesting heterozygotes with CARASIL', *Neurology*, 86: 1964-74.

Nozaki, H., M. Nishizawa, and O. Onodera. 2014. 'Features of cerebral autosomal recessive arteriopathy with subcortical infarcts and leukoencephalopathy', *Stroke*, 45: 3447-53.

Oide, T., H. Nakayama, S. Yanagawa, N. Ito, S. Ikeda, and K. Arima. 2008. 'Extensive loss of arterial medial smooth muscle cells and mural extracellular matrix in cerebral autosomal recessive arteriopathy with subcortical infarcts and leukoencephalopathy (CARASIL)', *Neuropathology*, 28: 132-42.

Oka, C., R. Tsujimoto, M. Kajikawa, K. Koshiba-Takeuchi, J. Ina, M. Yano, A. Tsuchiya, Y. Ueta, A. Soma, H. Kanda, M. Matsumoto, and M. Kawaichi. 2004. 'HtrA1 serine protease inhibits signaling mediated by Tgfbeta family proteins', *Development*, 131: 1041-53.

Olzscha, H., S. M. Schermann, A. C. Woerner, S. Pinkert, M. H. Hecht, G. G. Tartaglia, M. Vendruscolo, M. Hayer-Hartl, F. U. Hartl, and R. M. Vabulas. 2011. 'Amyloid-like aggregates sequester numerous metastable proteins with essential cellular functions', *Cell*, 144: 67-78.

Pantoni, L. 2010. 'Cerebral small vessel disease: from pathogenesis and clinical characteristics to therapeutic challenges', *Lancet Neurol*, 9: 689-701.

Pepys, M. B. 2018. 'The Pentraxins 1975-2018: Serendipity, Diagnostics and Drugs', *Front Immunol*, 9: 2382.

Pepys, Mark. 2015. 'New therapeutic perspectives – amyloid removal', *Orphanet Journal of Rare Diseases*, 10: I17.

Peters, N., C. Opherk, S. Zacherle, A. Capell, P. Gempel, and M. Dichgans. 2004. 'CADASIL-associated Notch3 mutations have differential effects both on ligand binding and ligand-induced Notch3 receptor signaling through RBP-Jk', *Exp Cell Res*, 299: 454-64.

Pippucci, T., A. Maresca, P. Magini, G. Cenacchi, V. Donadio, F. Palombo, V. Papa, A. Incensi, G. Gasparre, M. L. Valentino, C. Preziuso, A. Pisano, M. Ragno, R. Liguori, C. Giordano, C. Tonon, R. Lodi, A. Parmeggiani, V. Carelli, and M. Seri. 2015. 'Homozygous NOTCH3 null mutation and impaired NOTCH3 signaling in recessive early-onset arteriopathy and cavitating leukoencephalopathy', *EMBO Mol Med*, 7: 848-58.

Poepsel, S., A. Sprengel, B. Sacca, F. Kaschani, M. Kaiser, C. Gatsogiannis, S. Raunser, T. Clausen, and M. Ehrmann. 2015. 'Determinants of amyloid fibril degradation by the PDZ protease HTRA1', *Nat Chem Biol*, 11: 862-9.

Poon, S., S. B. Easterbrook-Smith, M. S. Rybchyn, J. A. Carver, and M. R. Wilson. 2000. 'Clusterin is an ATP-independent chaperone with very broad substrate specificity that stabilizes stressed proteins in a folding-competent state', *Biochemistry*, 39: 15953-60.

Poulsen, E. T., N. S. Nielsen, C. Scavenius, E. H. Mogensen, M. W. Risor, K. Runager, M. V. Lukassen, C. B. Rasmussen, G. Christiansen, M. Richner, H. Vorum, and J. J. Enghild. 2019. 'The serine protease HtrA1 cleaves misfolded transforming growth factor beta-induced protein (TGFBIp) and induces amyloid formation', *J Biol Chem*, 294: 11817-28.

Prince, M., R. Bryce, E. Albanese, A. Wimo, W. Ribeiro, and C. P. Ferri. 2013. 'The global prevalence of dementia: a systematic review and metaanalysis', *Alzheimers Dement*, 9: 63-75 e2.

Rasmussen, M. K., H. Mestre, and M. Nedergaard. 2018. 'The glymphatic pathway in neurological disorders', *Lancet Neurol*, 17: 1016-24.

Razvi, S. S., R. Davidson, I. Bone, and K. W. Muir. 2005. 'The prevalence of cerebral autosomal dominant arteriopathy with subcortical infarcts and leucoencephalopathy (CADASIL) in the west of Scotland', *J Neurol Neurosurg Psychiatry*, 76: 739-41.

Richards, A., A. M. van den Maagdenberg, J. C. Jen, D. Kavanagh, P. Bertram, D. Spitzer, M. K. Liszewski, M. L. Barilla-Labarca, G. M. Terwindt, Y. Kasai, M. McLellan, M. G. Grand, K. R. Vanmolkot, B. de Vries, J. Wan, M. J. Kane, H. Mamsa, R. Schafer, A. H. Stam, J. Haan, P. T. de Jong, C. W. Storimans, M. J. van Schooneveld, J. A. Oosterhuis, A. Gschwendter, M. Dichgans, K. E. Kotschet, S. Hodgkinson, T. A. Hardy, M. B. Delatycki, R. A. Hajj-Ali, P. H. Kothari, S. F. Nelson, R. R. Frants, R. W. Baloh, M. D. Ferrari, and J. P. Atkinson. 2007. 'C-terminal truncations in human 3'-5' DNA exonuclease TREX1 cause autosomal dominant retinal vasculopathy with cerebral leukodystrophy', *Nat Genet*, 39: 1068-70.

Runyon, S. T., Y. Zhang, B. A. Appleton, S. L. Sazinsky, P. Wu, B. Pan, C. Wiesmann, N. J. Skelton, and S. S. Sidhu. 2007. 'Structural and functional analysis of the PDZ domains of human HtrA1 and HtrA3', *Protein Sci*, 16: 2454-71.

Rutten-Jacobs, L. C. A., and N. S. Rost. 2019. 'Emerging insights from the genetics of cerebral small-vessel disease', *Ann N Y Acad Sci*.

Rutten, J. W., E. M. Boon, M. K. Liem, J. G. Dauwerse, M. J. Pont, E. Vollebregt, A. J. Maat-Kievit, H. B. Ginjaar, P. Lakeman, S. G. van Duinen, G. M. Terwindt, and S. A. Lesnik Oberstein. 2013. 'Hypomorphic NOTCH3 alleles do not cause CADASIL in humans', *Hum Mutat*, 34: 1486-9.

Rutten, J. W., B. J. Van Eijsden, M. Duering, E. Jouvent, C. Opherk, L. Pantoni, A. Federico, M. Dichgans, H. S. Markus, H. Chabriat, and S. A. J. Lesnik Oberstein. 2019. 'The effect of NOTCH3 pathogenic variant position on CADASIL disease severity: NOTCH3 EGFr 1-6 pathogenic variant are associated with a more severe phenotype and lower survival compared with EGFr 7-34 pathogenic variant', *Genet Med*, 21: 676-82.

Salvi, F., R. Michelucci, R. Plasmati, L. Parmeggiani, P. Zonari, M. Mascalchi, and C. A. Tassinari. 1992. 'Slowly progressive familial dementia with recurrent strokes and white matter hypodensities on CT scan', *Ital J Neurol Sci*, 13: 135-40.

Sasaki, K., K. Doh-ura, Y. Wakisaka, and T. Iwaki. 2002. 'Clusterin/apolipoprotein J is associated with cortical Lewy bodies: immunohistochemical study in cases with alpha-synucleinopathies', *Acta Neuropathol*, 104: 225-30.

Schubert, V., B. Bender, M. Kinzel, N. Peters, and T. Freilinger. 2018. 'A novel frameshift variant in the CADASIL gene NOTCH3: pathogenic or not?', *J Neurol*, 265: 1338-42.

Searcy, J. L., T. Le Bihan, N. Salvadores, J. McCulloch, and K. Horsburgh. 2014. 'Impact of age on the cerebrovascular proteomes of wild-type and Tg-SwDI mice', *PLoS One*, 9: e89970.

Selkoe, D. J. 2001. 'Alzheimer's disease: genes, proteins, and therapy', *Physiol Rev*, 81: 741-66.

Shiga, A., H. Nozaki, A. Yokoseki, M. Nihonmatsu, H. Kawata, T. Kato, A. Koyama, K. Arima, M. Ikeda, S. Katada, Y. Toyoshima, H. Takahashi, A. Tanaka, I. Nakano, T. Ikeuchi, M. Nishizawa, and O. Onodera. 2011. 'Cerebral small-vessel disease protein HTRA1 controls the amount of TGF-beta1 via cleavage of proTGF-beta1', *Hum Mol Genet*, 20: 1800-10.

Shin, T. M., J. M. Isas, C. L. Hsieh, R. Kayed, C. G. Glabe, R. Langen, and J. Chen. 2008. 'Formation of soluble amyloid oligomers and amyloid fibrils by the multifunctional protein vitronectin', *Mol Neurodegener*, 3: 16.

Singhal, S., S. Bevan, T. Barrick, P. Rich, and H. S. Markus. 2004. 'The influence of genetic and cardiovascular risk factors on the CADASIL phenotype', *Brain*, 127: 2031-8.

Skorko-Glonek, J., D. Zurawa-Janicka, T. Koper, M. Jarzab, D. Figaj, P. Glaza, and B. Lipinska. 2013. 'HtrA protease family as therapeutic targets', *Curr Pharm Des*, 19: 977-1009.

Sondergaard, C. B., J. E. Nielsen, C. K. Hansen, and H. Christensen. 2017. 'Hereditary cerebral small vessel disease and stroke', *Clin Neurol Neurosurg*, 155: 45-57.

Sonninen, V., and M. L. Savontaus. 1987. 'Hereditary multi-infarct dementia', *Eur Neurol*, 27: 209-15.

Stevens, D. L., R. H. Hewlett, and B. Brownell. 1977. 'Chronic familial vascular encephalopathy', *Lancet*, 1: 1364-5.

Tennstaedt, A., S. Popsel, L. Truebestein, P. Hauske, A. Brockmann, N. Schmidt, I. Irle, B. Sacca, C. M. Niemeyer, R. Brandt, H. Ksiezak-Reding, A. L. Tirniceriu, R. Egensperger, A. Baldi, L. Dehmelt, M. Kaiser, R. Huber, T. Clausen, and M. Ehrmann. 2012. 'Human high temperature requirement serine protease A1 (HTRA1) degrades tau protein aggregates', *J Biol Chem*, 287: 20931-41.

Thal, D. R., E. Ghebremedhin, U. Rub, H. Yamaguchi, K. Del Tredici, and H. Braak. 2002. 'Two types of sporadic cerebral amyloid angiopathy', *J Neuropathol Exp Neurol*, 61: 282-93.

Tiaden, A. N., and P. J. Richards. 2013. 'The emerging roles of HTRA1 in musculoskeletal disease', *Am J Pathol*, 182: 1482-8.

Tikka, S., M. Baumann, M. Siitonen, P. Pasanen, M. Poyhonen, L. Myllykangas, M. Viitanen, T. Fukutake, E. Cognat, A. Joutel, and H. Kalimo. 2014. 'CADASIL and CARASIL', *Brain Pathol*, 24: 525-44.

Tiwari, A., M. Schneider, A. Fiorino, R. Haider, M. J. Okoniewski, B. Roschitzki, A. Uzozie, M. Menigatti, J. Jiricny, and G. Marra. 2013. 'Early insights into the function of KIAA1199, a markedly overexpressed protein in human colorectal tumors', *PLoS One*, 8: e69473.

Tournier-Lasserve, E., M. T. Iba-Zizen, N. Romero, and M. G. Bousser. 1991. 'Autosomal dominant syndrome with strokelike episodes and leukoencephalopathy', *Stroke*, 22: 1297-302.

Tsuchiya, A., M. Yano, J. Tocharus, H. Kojima, M. Fukumoto, M. Kawaichi, and C. Oka. 2005. 'Expression of mouse HtrA1 serine protease in normal bone and cartilage and its upregulation in joint cartilage damaged by experimental arthritis', *Bone*, 37: 323-36.

Vahedi, K., H. Chabriat, C. Levy, A. Joutel, E. Tournier-Lasserve, and M. G. Bousser. 2004. 'Migraine with aura and brain magnetic resonance imaging abnormalities in patients with CADASIL', *Arch Neurol*, 61: 1237-40.

Vanlandewijck, M., L. He, M. A. Mae, J. Andrae, K. Ando, F. Del Gaudio, K. Nahar, T. Lebouvier, B. Lavina, L. Gouveia, Y. Sun, E. Raschperger, M. Rasanen, Y. Zarb, N. Mochizuki, A. Keller, U. Lendahl, and C. Betsholtz. 2018. 'A molecular atlas of cell types and zonation in the brain vasculature', *Nature*, 554: 475-80.

Venkatraman, A., B. Dutta, E. Murugan, H. Piliang, R. Lakshminaryanan, A. C. Sook Yee, K. V. Pervushin, S. K. Sze, and J. S. Mehta. 2017. 'Proteomic Analysis of Amyloid Corneal Aggregates from TGFBI-H626R Lattice Corneal Dystrophy Patient Implicates Serine-Protease HTRA1 in Mutation-Specific Pathogenesis of TGFBIp', *J Proteome Res*, 16: 2899-913.

Verbeek, M. M., I. Otte-Holler, R. Veerhuis, D. J. Ruiter, and R. M. De Waal. 1998. 'Distribution of A beta-associated proteins in cerebrovascular amyloid of Alzheimer's disease', *Acta Neuropathol*, 96: 628-36.

Verdura, E., D. Herve, F. Bergametti, C. Jacquet, T. Morvan, C. Prieto-Morin, A. Mackowiak, E. Manchon, H. Hosseini, C. Cordonnier, I. Girard-Buttaz, S. Rosenstingl, C. Hagel, G. Kuhlenbaumer, E. Leca-Radu, D. Goux, L. Fleming, T. Van Agtmael, H. Chabriat, F. Chapon, and E. Tournier-Lasserve. 2016. 'Disruption of a miR-29 binding site leading to COL4A1 upregulation causes pontine autosomal dominant microangiopathy with leukoencephalopathy', *Ann Neurol*, 80: 741-53.

Verdura, E., D. Herve, E. Scharrer, M. Amador Mdel, L. Guyant-Marechal, A. Philippi, A. Corlobe, F. Bergametti, S. Gazal, C. Prieto-Morin, N. Beaufort, B. Le Bail, I. Viakhireva, M. Dichgans, H. Chabriat, C. Haffner, and E. Tournier-Lasserve. 2015. 'Heterozygous HTRA1 mutations are associated with autosomal dominant cerebral small vessel disease', *Brain*, 138: 2347-58.

Vierkotten, S., P. S. Muether, and S. Fauser. 2011. 'Overexpression of HTRA1 leads to ultrastructural changes in the elastic layer of Bruch's membrane via cleavage of extracellular matrix components', *PLoS One*, 6: e22959.

Viswanathan, A., and S. M. Greenberg. 2011. 'Cerebral amyloid angiopathy in the elderly', *Ann Neurol*, 70: 871-80.

Wang, L., M. E. Clark, D. K. Crossman, K. Kojima, J. D. Messinger, J. A. Mobley, and C. A. Curcio. 2010. 'Abundant lipid and protein components of drusen', *PLoS One*, 5: e10329.

Wardlaw, J. M., C. Smith, and M. Dichgans. 2013. 'Mechanisms of sporadic cerebral small vessel disease: insights from neuroimaging', *Lancet Neurol*, 12: 483-97.

Wardlaw, J. M., C. Smith, and M. Dichgans. 2019. 'Small vessel disease: mechanisms and clinical implications', *Lancet Neurol*, 18: 684-96.

Weller, R. O., C. A. Hawkes, R. N. Kalaria, D. J. Werring, and R. O. Carare. 2015. 'White matter changes in dementia: role of impaired drainage of interstitial fluid', *Brain Pathol*, 25: 63-78.

Wilken, C., K. Kitzing, R. Kurzbauer, M. Ehrmann, and T. Clausen. 2004. 'Crystal structure of the DegS stress sensor: How a PDZ domain recognizes misfolded protein and activates a protease', *Cell*, 117: 483-94.

Wilson, M. R., and A. Zoubeidi. 2017. 'Clusterin as a therapeutic target', *Expert Opin Ther Targets*, 21: 201-13.

Wisniewski, J. R., A. Zougman, N. Nagaraj, and M. Mann. 2009. 'Universal sample preparation method for proteome analysis', *Nat Methods*, 6: 359-62.

Wojtas, A. M., S. S. Kang, B. M. Olley, M. Gatherer, M. Shinohara, P. A. Lozano, C. C. Liu, A. Kurti, K. E. Baker, D. W. Dickson, M. Yue, L. Petrucelli, G. Bu, R. O. Carare, and J. D. Fryer. 2017. 'Loss of clusterin shifts amyloid deposition to the cerebrovasculature via disruption of perivascular drainage pathways', *Proc Natl Acad Sci U S A*, 114: E6962-E71.

Wyatt, A. R., J. J. Yerbury, R. A. Dabbs, and M. R. Wilson. 2012. 'Roles of extracellular chaperones in amyloidosis', *J Mol Biol*, 421: 499-516.

Xu, X., S. H. Choi, T. Hu, K. Tiyanont, R. Habets, A. J. Groot, M. Vooijs, J. C. Aster, R. Chopra, C. Fryer, and S. C. Blacklow. 2015. 'Insights into Autoregulation of Notch3 from Structural and Functional Studies of Its Negative Regulatory Region', *Structure*, 23: 1227-35.

Yamazaki, Y., N. Zhao, T. R. Caulfield, C. C. Liu, and G. Bu. 2019. 'Apolipoprotein E and Alzheimer disease: pathobiology and targeting strategies', *Nat Rev Neurol*, 15: 501-18.

Yang, H., and H. Y. Hu. 2016. 'Sequestration of cellular interacting partners by protein aggregates: implication in a loss-of-function pathology', *Febs j*, 283: 3705-17.

Yerbury, J. J., S. Poon, S. Meehan, B. Thompson, J. R. Kumita, C. M. Dobson, and M. R. Wilson. 2007. 'The extracellular chaperone clusterin influences amyloid formation and toxicity by interacting with prefibrillar structures', *Faseb j*, 21: 2312-22.

Yoshida, H., A. Nagaoka, A. Komiya, M. Aoki, S. Nakamura, T. Morikawa, R. Ohtsuki, T. Sayo, Y. Okada, and Y. Takahashi. 2018. 'Reduction of hyaluronan and increased expression of HYBID (alias CEMIP and KIAA1199) correlate with clinical symptoms in photoaged skin', *Br J Dermatol*, 179: 136-44.

Yoshida, H., A. Nagaoka, A. Kusaka-Kikushima, M. Tobiishi, K. Kawabata, T. Sayo, S. Sakai, Y. Sugiyama, H. Enomoto, Y. Okada, and S. Inoue. 2013. 'KIAA1199, a deafness gene of unknown function, is a new hyaluronan binding protein involved in hyaluronan depolymerization', *Proc Natl Acad Sci U S A*, 110: 5612-7.

Yousif, S., C. Marie-Claire, F. Roux, J. M. Scherrmann, and X. Decleves. 2007. 'Expression of drug transporters at the blood-brain barrier using an optimized isolated rat brain microvessel strategy', *Brain Res*, 1134: 1-11.

Yu, J. T., L. Tan, and J. Hardy. 2014. 'Apolipoprotein E in Alzheimer's disease: an update', *Annu Rev Neurosci*, 37: 79-100.

Zhang, X., S. J. Lee, M. F. Young, and M. M. Wang. 2015. 'The small leucine-rich proteoglycan BGN accumulates in CADASIL and binds to NOTCH3', *Transl Stroke Res*, 6: 148-55.

Zhang, Y., B. A. Appleton, P. Wu, C. Wiesmann, and S. S. Sidhu. 2007. 'Structural and functional analysis of the ligand specificity of the HtrA2/Omi PDZ domain', *Protein Sci*, 16: 1738-50.

Ziaei, A., X. Xu, L. Dehghani, C. Bonnard, A. Zellner, A. Y. Jin Ng, S. Tohari, B. Venkatesh, C. Haffner, B. Reversade, V. Shaygannejad, and M. A. Pouladi. 2019. 'Novel mutation in HTRA1 in a family with diffuse white matter lesions and inflammatory features', *Neurol Genet*, 5: e345.

COPYRIGHT INFORMATION

Figure number	1.1
License number	4693620850585
License date	Oct 21, 2019
Licensed content publisher	Elsevier
Licensed content publication	The Lancet Neurology
Licensed content title	Small vessel disease: mechanisms and clinical implications
Licensed content author	Joanna M Wardlaw, Colin Smith, Martin Dichgans

Figure number	1.4
License number	4693620557537
License date	Oct 21, 2019
Licensed content publisher	Wolters Kluwer Health, Inc.
Licensed content publication	Stroke
Licensed content title	Role of NOTCH3 Mutations in the Cerebral Small Vessel Disease Cerebral Autosomal Dominant Arteriopathy With Subcortical Infarcts and Leukoencephalopathy
Licensed content author	Kirsten Coupland, Urban Lendahl, Helena Karlström

Figure number	1.6
License number	4693611503168
License date	Oct 21, 2019
Licensed content publisher	Springer Nature
Licensed content publication	Acta Neuropathologica
Licensed content title	Notch3 ectodomain is a major component of granular osmiophilic material (GOM) in CADASIL
Licensed content author	Akira Ishiko, Atsushi Shimizu, Eiichiro Nagata et al

Figure numbers	3.1, 3.3, 3.4, 3.5, 3.6, 3.7, 3.8, 3.9, 3.10, 3.11, 3.12, 3.14, 3.15, 3.16, 3.17, 3.19 and 3.20
License number	4693610213818
License date	Oct 21, 2019
Licensed content publisher	Springer Nature
Licensed content publication	Acta Neuropathologica
Licensed content title	CADASIL brain vessels show a HTRA1 loss-of-function profile
Licensed content author	Andreas Zellner, Eva Scharrer, Thomas Arzberger et al

ACKNOWLEDGEMENT